# ABSTRACT

Title of Dissertation: INTERNAL WAVE-TOPOGRAPHY
AND FLOW INTERACTIONS
IN THE BOTTOM BOUNDARY LAYER

Victoria Whitley Clark
Doctor of Philosophy, 2026

Dissertation Directed by: Assistant Professor Jacob Wenegrat
Department of Atmospheric & Oceanic Science

Turbulent bottom boundary layers (BBLs) over sloping topography play a central role in modifying water properties along dense overflow pathways and sustaining the upwelling limb of the global overturning circulation. This work examines the mechanisms controlling the transport and mixing of buoyancy, momentum, and tracers in these layers using high-resolution, idealized large-eddy simulations with a grid-fitted immersed boundary method (IBM). The IBM is validated against canonical downslope Ekman flows, reproducing BBL structure and associated transports across grid-fitted topographic resolutions.

Internal waves breaking on slopes generate near-bottom bores and overturns in the "internal swash" zone, driving fluid ejections into the stratified interior. The extent of these overturns, turbulent mixing, and along-isopycnal intrusions depends strongly on the effective wave height, a length scale defined by the ratio of wave velocity to background buoyancy frequency. A volume budget and patterns in buoyancy flux divergence reveal spatial and temporal variability critical

for assessing water-mass transformation and restratification.

In dense overflows, symmetric instability (SI) and near-inertial waves, modified by a generated baroclinic background field, extract energy from the mean flow, enhance cross-slope transport, and increase dissipation within the BBL. Long after surface cooling is shut off, SI cells continue to propagate towards the shelf break, driving persistent off-shelf export of dense water. In the interior, positive potential vorticity features generated by the propagation of the gravity current cause the reflection and trapping of near- and sub-inertial waves, promoting wave breaking and possibly enhanced diapycnal mixing.

These results demonstrate that interactions among topography, mean flow, internal waves, and submesoscale instabilities play a fundamental role in BBL dynamics, tracer transport, and energy redistribution in dense overflow regions and the deep ocean. By characterizing the restratification and mixing by internal wave breaking, persistent SI-driven off-shelf export, and dense overflow-modified near-inertial wave trapping and reflection, this work provides a framework for interpreting boundary-driven exchange and mixing, thereby guiding their future representation and evaluation in global ocean models.

# INTERNAL WAVE-TOPOGRAPHY AND FLOW INTERACTIONS IN THE BOTTOM BOUNDARY LAYER

by

Victoria Whitley Clark

Dissertation submitted to the Faculty of the Graduate School of the
University of Maryland, College Park in partial fulfillment
of the requirements for the degree of
Doctor of Philosophy
2026

Advisory Committee:
Assistant Professor Jacob Wenegrat, Chair/Advisor
Professor James Carton
Associate Professor Kayo Ide
Professor Johan Larsson
Assistant Professor Madeleine Youngs

© Copyright by
Victoria Whitley Clark
2026

# Dedication

To every girl who talks math in spaces where she is outnumbered.

# Acknowledgments

First and foremost, I want to extend my deepest gratitude to my advisor, Dr. Jacob Wenegrat, whose intellectual rigor, patience, and guidance have been invaluable. Your willingness to take on an applied math student who knew nothing about the ocean as your first student, all during the chaos of the pandemic, has shaped me into the scholar I am today. You have helped me become a better thinker, writer, and oceanographer, and have provided me with a template for how to be a good mentor, leader, and academic.

I am also grateful to my committee members, Drs. Jim Carton, Kayo Ide, Johan Larsson, and Madeleine Youngs, whose broad expertise and thoughtful questions pushed me to consider perspectives I might not have otherwise explored and strengthened this work. I am equally thankful to Drs. Tomás Chor and Greg Wagner for helping me understand modeling in Oceananigans and coding in Julia. This work was partially supported by the National Science Foundation (NSF). I also acknowledge computing support from the Casper system, provided by the NSF's National Center for Atmospheric Research (NCAR).

I want to thank all of my friends, both in graduate school and beyond, for providing both intellectual community and emotional support. Michael, JJ, Marco, and the rest of my amazing cohort in AMSC helped me grow into a graduate student, supporting me through those early classes and staying connected, even during a pandemic. I will be forever grateful to my Wenegrads, my research group and officemates, who were willing to adopt a math student and welcome

me into their family. Thank you, Igor, Zihan, Shaun, Reint, Rachel, Logan, Zhihua, and Katharina, for always helping to tamp down the impostor syndrome and for every walk, coffee, and lunch that helped me get through my day. Thank you, Margaux, Erica, and Lucy, as well, for following me from college to the DMV and reminding me that there is life on the outside!

I am deeply grateful to my family — the Whitleys, Shearins, and Clarks — for always believing in me and offering their love. I want to thank my aunt, Jane Caviness, who showed me what a woman mathematician looks like. I also want to thank my siblings, Nicole and Zac, who might claim to have taught me everything I know, and will definitely make sure the "doctor" doesn't go to my head. I especially want to thank my parents, John and Daun Whitley, and grandparents, Ron and Roma Shearin, for instilling in all of us the importance of education and lifelong learning, while valuing family and the connections that make life worth living.

Finally, to my husband, Brandon, who has lived with me and this dissertation these last six years: your patience, love, and respect have always been something I can count on. Thank you for encouraging me through all of my moments of doubt and celebrating every milestone along the way. I love you, and I look forward to continuing our journey together.

# Table of Contents


Dedication ii

Acknowledgements iii

Table of Contents v

List of Tables vii

List of Figures viii

List of Abbreviations x

Chapter 1: Introduction 1
- 1.1 Background and Motivation . . . 1
  - 1.1.1 A global motivation for studying bottom boundary layer processes . . . 1
  - 1.1.2 Internal waves as a mechanism for near boundary mixing and interior-boundary exchange . . . 3
  - 1.1.3 Submesoscale processes as a mechanism for near boundary mixing and interior-boundary exchange . . . 5
- 1.2 Dissertation structure . . . 7

Chapter 2: Validation of a Grid-Fitted Immersed Boundary Method for Simulating Ocean Bottom Boundary Layers 10
- 2.1 Introduction and Motivation . . . 10
- 2.2 Immersed Boundary Formulation . . . 14
- 2.3 Grid-Fitted IBM Implementation . . . 17
  - 2.3.1 Model Formulation . . . 17
  - 2.3.2 Immersed node classification . . . 21
  - 2.3.3 Boundary conditon enforcement . . . 22
- 2.4 Validation Ekman Theory . . . 25
- 2.5 Validation Set Up . . . 28
- 2.6 Validation Results . . . 31
  - 2.6.1 Validation Case 1: Unstratified, Laminar Ekman . . . 31
  - 2.6.2 Validation Case 2: Unstratified, Turbulent Ekman . . . 35
  - 2.6.3 Validation Case 3: Stratified, Turbulent Ekman . . . 39
- 2.7 Assessment and Outlook . . . 45

Chapter 3: Breaking internal waves on sloping topography: connecting parcel displacements to overturn size, interior-boundary exchanges, and mixing 49
3.1 Introduction . . . 49
3.2 Numerical Model Set Up . . . 52
3.3 Results . . . 58
3.3.1 Physical mechanism and scaling of breaking internal waves . . . 58
3.3.2 Overturns and dissipation in breaking waves scaled by $h_w$ . . . 64
3.3.3 Boundary layer and interior exchange through adiabatic pumping . . . 67
3.3.4 Turbulent buoyancy fluxes . . . 74
3.4 Conclusion . . . 79

Chapter 4: Symmetric instability and modification of near-inertial waves in dense-water overflows 82
4.1 Introduction . . . 82
4.2 Numerical Set Up . . . 85
4.3 Behavior of dense-water overflows from simulations . . . 87
4.3.1 Dense water formation and overflow . . . 88
4.3.2 Adjustment after the shutdown of the dense overflow . . . 90
4.4 Potential vorticity in dense-water overflow . . . 94
4.4.1 Description of the PV budget . . . 94
4.4.2 PV evolution during dense water formation and overflow . . . 97
4.4.3 PV evolution after the shutdown of the dense overflow . . . 103
4.5 Symmetric Instability and downslope pulsing on shelf . . . 106
4.6 Modification of NIWs by background dense overflow . . . 115
4.7 Discussion . . . 122
4.8 Conclusion . . . 126

Chapter 5: Conclusion 131

Appendix A: Calculations of Intrusion Thickness 137
A.1 Numerical calculation of tracer intrusion thickness . . . 137
A.2 Numerical calculation of interior stratification anomaly thickness . . . 140

Appendix B: Grid Resolution Analysis 141

Bibliography 143

# List of Tables

2.1 Validation Simulation Parameters . . . . . 30

3.1 Simulation Parameters for Main Reference Set . . . . . 55
3.2 Constant Simulation Parameters for Main Reference Set . . . . . 56
3.3 Simulation Parameters for Assessing Sensitivity to Wave Frequency, $\sigma$, and Criticality, $\gamma$ . . . . . 57

# List of Figures


2.1 Schematic of Immersed Boundaries . . . 14
2.2 IBM node classification in Oceananigans . . . 21
2.3 Topographic coarsening used to validate grid fitted IBM . . . 29
2.4 Laminar Ekman flow validation snapshots . . . 32
2.5 Laminar Ekman flow comparison metrics . . . 34
2.6 Turbulent Ekman flow comparison metrics . . . 35
2.7 Turbulence and vorticity in unstratified Ekman flow . . . 37
2.8 Stratified Ekman snapshots on refined topography . . . 39
2.9 Stratified Ekman snapshots on coarse topography . . . 40
2.10 Across-slope averaged profiles in stratified Ekman flows . . . 42
2.11 Length scale comparisons for stratified Ekman . . . 43
2.12 Ekman transport comparisons in time for stratified Ekman . . . 44

3.1 3D LES domain set up . . . 53
3.2 Early wave velocity snapshots . . . 58
3.3 Later wave velocity snapshots . . . 59
3.4 3D contours of spanwise vorticity . . . 60
3.5 Thorpe scale vs. Effective Wave Height . . . 62
3.6 Ozmidov scale vs Effective Wave Height . . . 64
3.7 Ejected tracer and dissipation snapshots . . . 67
3.8 3D dye contours . . . 68
3.9 Volume budget schematic . . . 70
3.10 Near-boundary buoyancy-binned, phase averaged quantities . . . 71
3.11 Tracer intrusion thickness vs. Effective Wave Height . . . 72
3.12 Triple decomposition of buoyancy fluxes . . . 75
3.13 Wave-averaged Eulerian buoyancy flux budget . . . 77
3.14 Buoyancy and volume changes in time . . . 78

4.1 3D LES dense overflow domain set up . . . 86
4.2 Snapshots of overflow during the cooling phase . . . 88
4.3 Snapshots of adjusted flow after cooling shuts off . . . 91
4.4 Snapshots of the shelf after cooling shuts off . . . 92
4.5 Volume integrated PV . . . 94
4.6 PV boundary flux components . . . 98
4.7 Location of vertical PV fluxes along the boundary . . . 99
4.8 Long term inertially averaged fields after cooling is shut down . . . 100
4.9 Snapshots of PV features at three points in time . . . 102

4.10 Stream functions of SI cells on the shelf . . . 106
4.11 Hovmöller plots of pulsing events on the shelf . . . 109
4.12 PDFs of bottom PV fluxes binned by velocity and buoyancy anomaly . . . 110
4.13 Net shelf export by SI cells . . . 112
4.14 Regionally averaged spectral analyses of vorticity and dissipation . . . 115
4.15 Ray tracing of NIWs . . . 118
4.16 Schematic of dense overflow processes during cooling and after cooling is shut down . . . 126

A.1 Tracer intrusion thickness calculation example . . . 138

B.1 Resolution Testing . . . 141

# List of Abbreviations and Symbols

| | |
|---|---|
| $A^{\alpha\pm}$ | Area of the top $(+)$ and bottom $(-)$ $\alpha$ face |
| BBL | Bottom Boundary Layer |
| $b$ | Buoyancy |
| $c, C$ | Arbitrary tracer |
| $C_D$ | Drag coefficient |
| CV | Coefficient of Variation |
| CFL | Courant–Friedrichs–Lewy stability condition |
| DNS | Direct Numerical Simulation |
| $\delta_e$ | Ekman depth |
| $\delta_e^*$ | Frictional velocity approximation to Ekman depth |
| $\delta_{\text{fit}}$ | Least squares fit to Ekman depth |
| $\Delta z_{\text{topo}}$ | Vertical topographic resolution of immersed step-size |
| $\mathscr{D}$ | Buoyancy diffusion term |
| $\text{Diab}^{\text{bot,top}}$ | Vertical diabatic flux contribution to potential vorticity |
| $\epsilon, \varepsilon$ | Dissipation of kinetic energy rate |
| $Fr$ | Froude Number |
| $f$ | Coriolis frequency |
| FVM | Finite Volume Method |
| $\boldsymbol{F}_b$ | Continuous forcing function |
| $\{\boldsymbol{F}_b'\}$ | Modified, discretized forcing function |
| $\boldsymbol{F_u}$ | Arbitrary velocity forcing function |
| $\boldsymbol{F}_c$ | Arbitrary tracer forcing function |
| $\boldsymbol{F}$ | Frictional velocity stress vector |
| $\text{Fric}^{\text{bot,top}}$ | Vertical frictional flux contribution to potential vorticity |
| $\boldsymbol{G_u}$ | Discretized velocity tendency |
| $G_c$ | Discretized tracer tendency |
| $\gamma$ | Slope criticality |
| $\Gamma_b$ | Boundary of fluid domain |
| $\Gamma_b'$ | Grid-fitted approximation of boundary |
| $h_{eff}$ | Effective height |
| $h_w$ | Effective wave height |
| IB | Immersed Boundary |
| IBM | Immersed Boundary Method |
| $\boldsymbol{J}$ | Potential vorticity fluxes in flux formulation |

| | |
|---|---|
| $\kappa$ | diffusivity |
| $\kappa_{vk}$ | von Kármán constant |
| $\vec{\boldsymbol{k}}$ | Cartesian vertical basis vector |
| KE | Kinetic energy |
| $l$ | Horizontal wave number |
| $\lambda$ | Slope of wave characteristics |
| $L_T$ | Thorpe Scale |
| $L_{tr}$ | Average tracer weighted thickness |
| $L_{N^2}$ | Average Stratification anomaly thickness |
| $L_O$ | Ozmidov length scale |
| LES | Large Eddy Simulations |
| $L_{xy,z}$ | Domain lengths |
| $m$ | Vertical wave number |
| $\vec{\boldsymbol{n}}$ | Boundary-normal vector |
| $\mathscr{N}$ | Nonlinear operator |
| $[N]$ | Discretized nonlinear operator |
| $[N']$ | Modified, discretized nonlinear operator |
| $N$ | Buoyancy frequency |
| $N_0$ | Background or initial buoyancy frequency |
| NIW | Near Inertial Wave |
| $\nu$ | Viscosity |
| $\nu_e$ | Turbulent eddy viscosity |
| $\Omega_b$ | Solid body domain |
| $\Omega_f$ | Fluid domain |
| $\boldsymbol{\omega}$ | Vorticity |
| $\partial\Omega_{i,j,k}$ | Boundary faces of a finite volume |
| $\omega$ | Internal wave frequency |
| $\omega_{\min}$ | Minimum internal wave frequency |
| ODE | Ordinary differential equations |
| $p$ | Pressure |
| $p_{non}$ | Non-hydrostatic pressure |
| $p_{hyd}$ | Hydrostatic pressure |
| $Pr_t$ | Turbulent Prandtl number |
| $\boldsymbol{\Phi}$ | Arbitrary state vector field |
| $\boldsymbol{\Phi}_\Gamma$ | Arbitrary state vector field boundary conditions |
| $\Psi$ | Streamfunction for velocity |
| PV | Potential vorticity |
| $\boldsymbol{q}_c$ | Diffusive tracer flux |
| $q$ | Potential vorticity |
| $\{\boldsymbol{r_b}\}$ | Discretized boundary conditions |

| | |
|---|---|
| $Re$ | Reynolds Number |
| $\rho_0$ | Reference density |
| RMS | Root mean square |
| $\sigma$ | Internal wave frequency |
| $\vec{\boldsymbol{s}}$ | Across-slope unit vector |
| $S_0$ | Slope Burger number |
| $s_b$ | Isopycnal slope |
| SI | Symmetric instability |
| $\tan\alpha$ | Topographic slope |
| $\tan\theta$ | Internal wave propagation slope |
| $T_\sigma$ | Internal wave period with frequency, $\sigma$ |
| $T_f$ | Inertial period with frequency, $f$ |
| $\boldsymbol{\tau}$ | Kinematic stress tensor |
| $t$ | Time |
| $\boldsymbol{u}$ | Full 3D velocity field |
| $\hat{\boldsymbol{u}}$ | Rotated across-slope velocity |
| $\boldsymbol{U}$ | Discretized velocity field |
| $U_E$ | Across-slope Ekman transport |
| $U$ | Rotated across-slope velocity |
| $\partial_s U$ | Rotated across-slope velocity divergence |
| $V_0$ | Maximum internal wave velocity |
| $V_0^B$ | Simulations with an increased vertical domain |
| $V_{i,j,k}$ | Finite volume |
| $\boldsymbol{V}$ | Constant background velocity vector |
| WENO | Weighted essentially non-oscillatory advection scheme |

# Chapter 1: Introduction

## 1.1 Background and Motivation

### 1.1.1 A global motivation for studying bottom boundary layer processes

Small-scale diapycnal processes drive the mixing and upwelling of dense waters that sink from high-latitude formation regions, essential for closing the global overturning circulation (Munk, 1966; Lumpkin and Speer, 2007; Talley, 2013; Ferrari, 2014). As dense waters, formed in regions such as the Nordic Seas or along Antarctic continental shelves, spill through narrow sills and descend along continental slopes, their properties are substantially modified by localized mixing processes near topography (Lumpkin and Speer, 2007; Killworth, 1983; Girton and Sanford, 2003). The entrainment and diapycnal exchange that occur as these dense overflows move downslope shape the water masses that ventilate the deep and intermediate ocean, setting the buoyancy structure that governs circulation and mixing downstream (Lumpkin and Speer, 2007; Killworth, 1983; Dickson and Brown, 1994; Almansi et al., 2017; Magaldi and Haine, 2015; Girton and Sanford, 2003). Once these dense waters sink, they become part of the North Atlantic Deep Water or the Antarctic Bottom Water, depending on their dense water formation origin (Lumpkin and Speer, 2007; Talley, 2013). These dense water masses must be transformed through diapycnal mixing into waters light enough to upwell and close this global circulation.

Observations and theory indicate that the intensity of this mixing increases toward the seafloor, reaching maxima over rough topography (Polzin et al., 1997; Kunze et al., 2006; Ferrari, 2014; MacKinnon et al., 2017). However, bottom-intensified mixing primarily drives diapycnal sinking within the ocean interior rather than the upwelling required for overturning closure (Laurent et al., 2001; Klocker and McDougall, 2010; Ferrari et al., 2016). Recent studies propose that the necessary upwelling occurs along sloping bottom topography within turbulent bottom boundary layers (BBLs) (Ferrari et al., 2016; Mashayek et al., 2017; Holmes and McDougall, 2020). The insulating bottom boundary condition allows convergent turbulent buoyancy fluxes to develop within a thin near-bottom layer, in contrast to the bottom-enhanced mixing profile aloft (Ferrari et al., 2016; Mashayek et al., 2017).

These advances have renewed focus on turbulent BBLs, including the mechanisms that drive "upside-down" mixing near sloping topography, the pathways through which mixed water escapes into the ocean interior, and the role of boundary-layer restratification in maintaining an efficient mixing process (Ferrari et al., 2016; van Haren, 2023; McPhee-Shaw et al., 2021a; Armi, 1978). The mixing and exchange in turbulent BBLs, essential to the upwelling limb of the circulation, can also transform water along dense overflow pathways before reaching the abyssal or intermediate-depth regions (Yankovsky and Legg, 2019; Qu et al., 2021b). Understanding these systems will be key to creating a comprehensive analytical theory of global circulation (Drake et al., 2020), as well as constraining how the ocean stores heat and carbon or transports nutrients or sediments (Friedrich et al., 2011; Toggweiler et al., 1989; Walin, 1982). Recent efforts have begun to characterize these abyssal mixing layers through observations (Wynne-Cattanach et al., 2024; Qu et al., 2021a; Garabato et al., 2019) and to investigate their dynamics using theoretical analyses and idealized simulations (Wenegrat et al., 2018; Wenegrat and Thomas, 2020; Holmes

et al., 2019; Qu et al., 2021b). Building on these studies, the present work employs Large Eddy Simulations (LES) in idealized models to examine how breaking internal tides along sloping boundaries, as well as interactions between submesoscale instabilities, near-inertial waves, and the mean flow, influence mixing and exchange near topography, forming a critical link in the upwelling limb of the global overturning circulation.

### 1.1.2 Internal waves as a mechanism for near boundary mixing and interior-boundary exchange

Internal tides that break directly on sloping topography can not only generate the turbulence required to sustain BBLs but could also provide a pathway for interior–boundary exchange (Armi, 1978; Slinn and Riley, 1998; Chalamalla et al., 2013; van Haren, 2023). Tidal motions over topography generate $\sim 1$ TW of energy into the ocean internal wave continuum (Whalen et al., 2020). These waves may break locally (Nash et al., 2007; Winters and Armi, 2013; Sarkar and Scotti, 2017), or, for lower modes, propagate hundreds of kilometers from their generation sites before encountering and breaking upon sloping boundaries (Aucan et al., 2006; van Haren et al., 2015; Jones et al., 2020; Whalen et al., 2020). Together with observed enhanced mixing in regions of elevated internal wave generation, the high energy content and widespread presence of internal waves throughout the world's oceans have long made them a leading candidate for driving the "missing mixing" in global circulation (Munk and Wunsch, 1998; Polzin et al., 1997; Waterhouse et al., 2014; Kunze, 2017). Extensive work has focused on internal waves breaking on critical slopes, where the topographic angle is close to that of the incoming wave (Nokes and Ivey, 1989; Slinn and Riley, 1998; Gemmrich and Klymak, 2015). However, oscillatory

"swashing" motions by internal waves along sloping boundaries can also induce overturning and breaking (Cyr and van Haren, 2016a; Winters, 2015; Gayen and Sarkar, 2011; van Haren, 2006). This "internal swash" ejects boundary fluid into the overlying water column (Winters, 2015; Nokes and Ivey, 1989), possibly facilitating biogeochemical exchange and contributing to water-mass transformation at the seafloor (Cacchione and Drake, 1986; Bonnin et al., 2006; Gardner et al., 2017; Armi, 1978). Internal tides breaking on sloping topography, therefore, represent a potential pathway for delivering energy to the bottom boundary and driving mixing and exchange along sloping topography. Nevertheless, the relationship between wave breaking and boundary ejections, the relevant length scales, and whether these processes actually drive the water-mass transformation required for upside-down mixing remain poorly understood (Winters, 2015); part of this work focuses on addressing these gaps (Whitley and Wenegrat, 2025).

On a global scale, near-inertial waves (NIWs), internal waves with frequencies close to the local Coriolis frequency, supply a comparable amount of power to the ocean as internal tides (Whalen et al., 2020; Alford et al., 2016). Therefore, they have a similar potential to drive turbulent mixing. This energy can radiate downward into the stratified ocean as NIWs, which often propagate nearly horizontally in regions of uniform stratification (Whalen et al., 2020). Their propagation is strongly influenced by background vorticity and lateral buoyancy gradients, which modify their intrinsic frequency and propagation pathways through baroclinic fronts and large-scale flows (Mooers, 1975; Kunze, 1985; Whitt and Thomas, 2013; Thomas et al., 2024; Young and Jelloul, 1997; D'Asaro, 1995a,b). Sloping bottom boundaries are often associated with baroclinic flows, such as found on continental shelves in western boundary currents or in dense overflow regions where isopycnals naturally align with sloping topography (Bryden et al., 2009; Meinen et al., 2009; Girton et al., 2001; Magaldi and Haine, 2015). With increasing baro-

clinicity, the minimum frequency of these waves can decrease, allowing NIWs to propagate in regions where their frequency is subinertial (Whitt and Thomas, 2013). Because NIWs propagate near the minimum allowable internal wave frequency (along isopycnals), strong horizontal buoyancy gradients found along these sloping boundaries can also change their angle of propagation; in some instances, with anomalously low wave frequency, both wave characteristics can propagate in the same vertical direction (Whitt and Thomas, 2013). These mean flow-induced modifications near topography can cause wave reflection, breaking, and trapping of NIWs (Qu et al., 2021b,a, 2022; Whitt and Thomas, 2013). For instance, with sufficiently steep isopycnals, NIWs propagating along slope-aligned isopycnals can get trapped and amplify in slantwise critical layers, where their group velocity approaches zero (Qu et al., 2021b). Wave breaking, trapping, and amplification can lead to enhanced turbulence and mixing in the BBL, as well as tracer transport (Qu et al., 2021b, 2022). NIWs generated in dense overflow regions may similarly intensify near-bottom mixing and cross-slope exchange, transforming water masses that eventually ventilate the intermediate and deep ocean as part of the global overturning circulation (Lumpkin and Speer, 2007; Killworth, 1983). The presence of breaking and trapped NIWs generated by dense overflows will be examined here.

### 1.1.3 Submesoscale processes as a mechanism for near boundary mixing and interior-boundary exchange

Just as submesoscale instabilities, fronts, and eddies are key drivers of vertical exchange and restratification in the surface mixed layer (McWilliams, 2016), similar dynamical settings in BBLs suggest that submesoscale turbulence may also play a key role in near-boundary mixing.

The submesoscale is defined by a dynamical regime in which inertial accelerations are comparable to Coriolis forces ($\sim O(1)$ Rossby number) and stratification and shear are of similar importance ($\sim O(1)$ Richardson number). These flows in the surface boundary layer promote restratification, regulate vertical fluxes, and mediate air–sea interactions. (Taylor and Ferrari, 2010; Boccaletti et al., 2007; Callies et al., 2015; Taylor and Thompson, 2023; Balwada et al., 2021; Uchoa et al., 2025). Characterized by strong lateral buoyancy gradients, horizontal and vertical shear, and strong vertical velocities, submesoscale processes modulate the exchange of water, heat, and nutrients between the mixed layer and the ocean interior (Mahadevan, 2016; Lévy et al., 2010; McWilliams, 2016) while providing a key pathway for the downscale transfer of energy (Fox-Kemper et al., 2008; Garabato et al., 2022; Boccaletti et al., 2007; Zheng et al., 2025; Dong et al., 2024). Despite the presence of comparable horizontal buoyancy gradients and frictional effects in BBLs over sloping topography, the influence of submesoscale turbulence on BBL dynamics and mixing remains more poorly understood. With kilometer-scale horizontal variability and timescales of hours to days, observing and modeling submesoscale dynamics remains particularly challenging (Uchida et al., 2022; McWilliams, 2016), and only recently have field campaigns begun to directly resolve these motions near the surface (Farrar et al., 2025), let alone the deep BBLs. Recent studies show that submesoscale motions in the BBL can enhance cross-shelf exchange, promote water-mass transformation, and cascade energy to smaller, dissipative scales (Gula et al., 2016b, 2015; Wenegrat et al., 2018; Ruan et al., 2017). Therefore, submesoscale turbulence could provide a complementary, mostly wave-independent pathway for BBL mixing and restratification that contributes to the global overturning circulation (Wenegrat et al., 2018; Callies, 2018).

Among submesoscale processes, symmetric instability (SI) can play a key role in regulat-

ing momentum and buoyancy exchange near sloping boundaries (Wenegrat and Thomas, 2020; Garabato et al., 2019; Wienkers et al., 2021; Thomas et al., 2013). SI can develop when potential vorticity becomes negative due to the combined effects of strong shear and lateral buoyancy gradients (Haine and Marshall, 1998). The resulting SI cells often drive efficient overturning and turbulent mixing that rapidly restores marginal stability (Thomas et al., 2013; Benthuysen and Thomas, 2012). In dense overflow regions, where strong horizontal density gradients and bottom-intensified shear are prevalent (Gawarkiewicz and Chapman, 1995; Beaird et al., 2013; Lin et al., 2020; Girton et al., 2001; Magaldi and Haine, 2015), SI may arise naturally (Lin et al., 2020; Brearley et al., 2012; Le Bras et al., 2022; Garabato et al., 2017) and enhance near-bottom mixing, accelerating water-mass transformation as dense waters descend and equilibrate along the slope. Here, we explore the development of SI in dense overflows and how these motions contribute to cross-shelf transport and the stabilization of the mean flow.

## 1.2 Dissertation structure

Taken together, these studies highlight that mixing, momentum and buoyancy exchange, and water-mass transformation in the BBL could arise from the interplay of multiple mechanisms, including internal tides breaking on sloping topography (Winters, 2015; Cyr and van Haren, 2016a; Cacchione and Drake, 1986), NIWs interacting with benthic fronts (Qu et al., 2021b; Whitt and Thomas, 2013; Qu et al., 2022), and submesoscale instabilities such as SI (Wenegrat and Thomas, 2020; Thomas et al., 2013; Garabato et al., 2017). The impact of these dynamics can depend strongly on slope, stratification, and background currents (Slinn and Riley, 1998; Cyr and van Haren, 2016a; Winters, 2015; Whitt and Thomas, 2013; Wenegrat and

Thomas, 2020; Umlauf and Burchard, 2011). Despite substantial observational and modeling efforts, the complex interactions between internal waves, submesoscale motions, and the mean flow near topography still require further study. These knowledge gaps motivate the use of high-resolution, idealized simulations to systematically examine how topography, internal waves, and submesoscale processes control BBL mixing and exchange.

Accurately representing bottom topography is essential for simulating geophysical flows, as BBL processes are often sensitive to frictional fluxes, slope angle, and curvature (Pedlosky, 2014; Slinn and Riley, 1998; MacCready and Rhines, 1991; Wenegrat and Thomas, 2020; Brink and Lentz, 2010). Chapter 2 describes the implementation and geophysical validation of a grid-fitted IBM for representing topography in Oceananigans, the incompressible, non-hydrostatic ocean model used throughout this thesis (Wagner et al., 2025a). The grid-fitted IBM is shown to be well suited for LES of geophysical flows, complementing the finite-volume formulation employed in Oceananigans (Wagner et al., 2025a; Mittal and Iaccarino, 2005). To assess its performance in a geophysical context, Chapter 2 validates the implementation using a suite of simulations of downslope Ekman flows, a submesoscale process strongly influenced by frictional bottom stresses (Garrett et al., 1993; Brink and Lentz, 2010; Umlauf et al., 2015; Wenegrat and Thomas, 2020). These tests demonstrate that the grid-fitted boundary accurately reproduces the formation and evolution of the BBL structure and associated Ekman transport, even when the relevant dynamical scales are only marginally resolved relative to the topographic step size.

The following chapter (Chapter 3) was published as Whitley, V. and Wenegrat, J.O., 2025: Breaking internal waves on sloping topography: connecting parcel displacements to overturn size, interior-boundary exchanges, and mixing. *J. Phys. Ocean.* (cited as Whitley and Wenegrat, 2025). This study employs a set of three-dimensional LES of a mode-one internal tide impinging

on a sloping immersed boundary to investigate the mechanisms of internal wave breaking. A detailed analysis of the breaking process reveals how swash-like motions (Cyr and van Haren, 2016a) lead to wave breaking along the slope and the subsequent ejection of fluid into the stratified interior. By systematically varying wave velocity, stratification, and slope criticality, the study identifies a key length scale, the "effective wave height", that governs dissipation and interior–boundary exchange throughout the breaking process (Whitley and Wenegrat, 2025). The results suggest that water-mass transformation and diapycnal mixing associated with these events depend on a more nuanced view of mixing, one that accounts for the spatial and temporal variability inherent to internal wave dynamics along sloping topography.

Chapter 4 examines the generation and persistence of SI and the modification of propagating NIWs within the near-boundary flow and stratification produced by dense overflows. A three-dimensional LES of a dense overflow system over a representative immersed topographic shelf and slope, with surface cooling, enables a detailed investigation of both the dynamics during dense water formation and the subsequent overflow, as well as the evolution of the mean flow once cooling ceases and the overflow stops. A detailed breakdown of the potential vorticity (PV) budget for the simulation highlights frictional boundary fluxes from the current injecting high PV along the shelf break, which is advected into the interior. Therefore, unlike previous work (Yankovsky and Legg, 2019), while SI is present on the shelf where surface cooling destroys PV, the interior is stable to SI. This simulation reveals that persistent SI and breaking NIWs extract energy from the geostrophic flow, drive cross-shelf transport and increased dissipation, with possible implications of enhanced BBL mixing.

Finally, Chapter 5 summarizes the findings presented in this dissertation and discusses remaining open questions, highlighting directions for future research needed to address them.

# Chapter 2: Validation of a Grid-Fitted Immersed Boundary Method for Simulating Ocean Bottom Boundary Layers

## 2.1 Introduction and Motivation

[1] Including topography in ocean models enables researchers to study geophysical processes, such as bottom boundary layer (BBL) dynamics and internal wave reflection, without relying on complex laboratory experiments or costly observations. Fluid-terrain interactions could be one of the major pathways of extracting energy from larger-scale flows in a forward energy flux by creating unbalanced submesoscale (0.1- 10 km) turbulence (Gula et al., 2016b; Chor and Wenegrat, 2025; Jagannathan et al., 2023). Over flat topography, the BBL does not typically generate benthic fronts, since buoyancy is relatively uniform along the bottom. In contrast, sloping topography allows for across-isopycnal flow, modifying potential vorticity and generating submesoscale instabilities (Wenegrat and Thomas, 2020; McWilliams, 2016; Garrett et al., 1993; Jagannathan et al., 2023), as well as interacting more directly with the internal wave field (Whitley and Wenegrat, 2025; Winters, 2015; Sarkar and Scotti, 2017; Lamb, 2014). The influx of energy into smaller flows can lead to elevated local dissipation and mixing outside of the

[1]Parts of this section have been adapted from previous project course work, which was not peer-reviewed, but is publicly available: Whitley, V., and Wenegrat, J.O., 2020: Introducing Topography to Large-Eddy Simulations. *AMSC 663 Project Report*. University of Maryland. Retrieved from https://www.math.umd.edu/ rvbalan/TEACHING/AMSC663Fall2020/PROJECTS/P7/index.html

oceanic boundary layers, of significance to the energy budget for general circulation (Gula et al., 2016b; Whitley and Wenegrat, 2025; Polzin et al., 1997). Such exchanges near complex topography can also increase interior-boundary exchange, transporting biogeochemical tracers such as carbon and oxygen crucial for the ecosystem (McPhee-Shaw et al., 2021b; Cyr and van Haren, 2016a; Bonnin et al., 2006; Whitley and Wenegrat, 2025).

There are many numerical methods for including topography in turbulence-resolving fluid models, including body-conforming structured and unstructured meshes, as well as terrain-following coordinates. Since the boundary itself in these methods becomes a part of the grid, boundary conditions are simple to implement, but depending on the complexity of the boundary, grid distortion can quickly lead to numerical errors (Zängl et al., 2004; Klemp, 2011). Transforming from Cartesian to terrain-following coordinates introduces metric terms, where small truncation errors in calculating pressure gradients over topography can overwhelm physical gradients, leading to errors and numerical instabilities (Klemp et al., 2003; Berntsen et al., 2015). Large Eddy Simulation turbulence models and subgrid-scale schemes often assume relatively isotropic grid cells, but grid cells near topography in conforming meshes can become highly anisotropic, degrading the performance of the closures (Schumann et al., 2020). Grids with varying cell shapes can also produce variations in numerical dispersion and dissipation, problematic in maintaining a physical turbulent spectra in LES models (Soufflet et al., 2016). Additionally, high-quality mesh generation is often time-consuming and computationally expensive, with a new mesh required for any desired changes to the terrain in a simulation. The sophisticated grid generation, careful treatment of near-boundary fields, and computational cost necessary for these methods make the immersed boundary method (IBM) a promising alternative for the integration of realistic bathymetry into high-resolution simulations (Nasr-Azadani and Meiburg, 2011; Arthur et al., 2020).

In IBM, instead of using meshes to conform to the terrain or solid body, topography is represented by an "immersed boundary" (IB) that can arbitrarily intersect a standard Cartesian grid. Then, boundary conditions are applied along the IB by modifying the governing equations through forcing terms on nearby grid points (Nasr-Azadani and Meiburg, 2011; DeLeon et al., 2018). In this way, many types of boundary conditions can be employed on whatever shape the surface has, while still maintaining a simple Cartesian grid, easily refined and implemented (Mittal and Iaccarino, 2005). The open-source ocean modeling package, Oceananigans, has implemented a simplified grid-fitted version of IBM to use on both direct numerical simulations (DNS) and Large Eddy Simulations (LES) (Wagner et al., 2025a). Due to the finite volume method (FVM) used in Oceananigans, the implementation of boundaries that are approximated by the nearest Cartesian cell boundary allows for the simple inclusion of topography, while keeping the finite volume properties intact (Wagner et al., 2025a).

Previous validation on IBM, including that of Oceananigans, has focused on aspects that are important for engineering applications, such as classical properties of a simulated flow around a cylinder, or on numerical accuracy: ensuring conservation properties and correct boundary conditions (Nasr-Azadani and Meiburg, 2011; Fornberg, 1980; Mittal and Iaccarino, 2005; Wagner et al., 2025a; Fadlun et al., 2000). While these are important in all fluid simulations, the use of IBM for geophysical applications, with rotating flow and density-stratified water, requires some additional considerations. The method must not only be numerically accurate, but also match the geophysical phenomenon being modelled. This is especially critical for the grid-fitted approximation to the topography made in Oceananigans, as the "stair steps" along the boundary will introduce vertical velocities, along with increased turbulence and possible changes to near boundary mixing.

To understand the impact of the grid-fitted IBM on geophysical applications, the dynamics of downslope Ekman transport in stratified and unstratified setups will be examined. Ekman flows are highly dependent on the frictional effects on the boundary. Bottom stress has impacts on the boundary layer height, bulk transport, and classic spiral behavior (Garrett et al., 1993; Brink and Lentz, 2010; Umlauf et al., 2015; Wenegrat and Thomas, 2020). Recent work also shows a growing community interest in how bottom Ekman dynamics contribute to upwelling in the abyssal circulation (Wenegrat and Thomas, 2020; Chor and Wenegrat, 2025; Jagannathan et al., 2023; Schubert et al., 2025; Srinivasan et al., 2019; Jagannathan et al., 2021). The clear theoretical solutions and parameters, along with the large boundary impact and active scientific interest in bottom Ekman flows, make it an ideal validation study for grid-fitted IBM. Validating the IBM implementation in Oceananigans using Ekman transport along grid-fitted slopes will highlight any impacts of the grid structure on geophysical problems.

In this chapter, we will discuss the theoretical framework of IBM in section 2.2 and the implementation in Oceananigans in section 2.3. This will be followed by the validation. Section 2.4 will describe the theory behind bottom Ekman flows, followed by a description of the numerical setup used for the validation in section 2.5. Section 2.6 discusses the results and validation in a rotated Ekman setup for laminar and turbulent simulations, with and without stratification. A summary of this assessment, as well as possible future enhancements to this study, are reviewed in section 2.7.

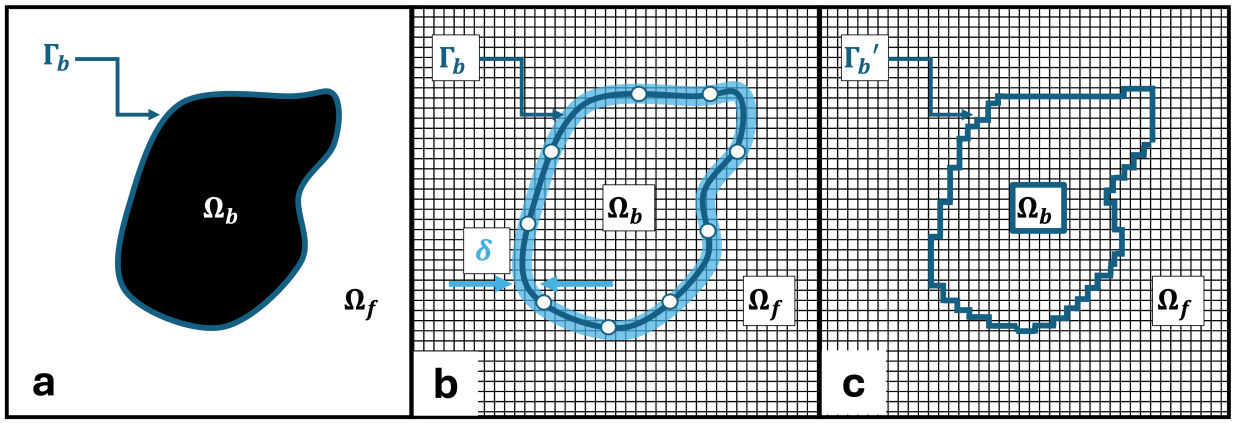



Figure 2.1: (a) Schematic of flow in $\Omega_f$ passing a generic body, $\Omega_b$, with boundary, $\Gamma_b$. (b) $\Omega_b$ immersed in a Cartesian grid with discretized governing equations. $\delta$ marks the smearing of the boundary in continuous IBM. (c) A grid-fitted IBM approximating $\Gamma_b$ by $\Gamma_b'$. (Adapted from Mittal and Iaccarino, 2005)

## 2.2 Immersed Boundary Formulation

There are two main techniques within IBM, discrete and continuous forcing methods (Mittal and Iaccarino, 2005), but, for geophysical applications, the discrete forcing method is more often used (Lundquist et al., 2012; Adcroft et al., 1997; Maronga et al., 2015). Consider a system of linear or nonlinear governing equations acting on a state vector $\mathbf{\Phi}$ in a fluid, representing any number of fields, such as velocity, pressure, or buoyancy. Following the formulation of Mittal and Iaccarino (2005), let $\mathscr{N}$ be the nonlinear operator such that,

$$\mathscr{N}(\mathbf{\Phi}) = 0 \qquad \in \Omega_f \tag{2.1}$$

$$\text{with } \mathbf{\Phi} = \mathbf{\Phi}_\Gamma \qquad \text{on } \Gamma_b, \tag{2.2}$$

where the fluid domain, $\Omega_f$, is enclosed by boundary, $\Gamma_b$, with boundary conditions, $\mathbf{\Phi}_\Gamma$ (Fig. 2.1a).

In continuous IBM, a forcing function, $\boldsymbol{F_b}$, is included in the continuous governing equations (2.1), as

$$\mathscr{N}(\boldsymbol{\Phi}) = \boldsymbol{F_b} \qquad \in (\Omega_f \cup \Omega_b), \tag{2.3}$$

such that now $\mathscr{N}$ operates on $\boldsymbol{\Phi}$ in both the fluid and solid body domain (Mittal and Iaccarino, 2005). Equation (2.3) can then be discretized on a Cartesian grid ($[N]\{\Phi\} = \{\boldsymbol{F_b}\}$), without having to conform around $\Omega_b$, and can be solved numerically as usual (Fig. 2.1b). The IB is often represented as a Dirac-delta forcing function, which has to be smoothed when discretized, causing stability constraints and a smearing of the boundary over several grid cells (Mittal and Iaccarino, 2005). The smeared boundary is represented in Fig. 2.1b by the $\delta$ thickness around $\Gamma_b$. Such a boundary representation makes the continuous IBM method undesirable for high Reynolds number flows and ocean applications (Mittal and Iaccarino, 2005), where the boundary processes are particularly important.

The alternative (direct-method) is to discretize the governing equations ($[N]\{\Phi\} = 0$), then add forcing directly to the cells within the IB to reflect its presence, resulting in a modified system of equations

$$[N']\{\boldsymbol{\Phi}\} = \{\boldsymbol{r_b}\} \qquad \in (\Omega_f \cup \Omega_b), \tag{2.4}$$

where $\{\boldsymbol{r}\}$ represents a discretized representation of known boundary conditions (Mittal and Iaccarino, 2005). Rewriting in terms of the original discretized operator,

$$[N]\{\boldsymbol{\Phi}\} = \{\boldsymbol{r_b}\} + [N]\{\Phi\} - [N']\{\Phi\} = \{\boldsymbol{F_b'}\} \qquad \in (\Omega_f \cup \Omega_b) \tag{2.5}$$

(Mittal and Iaccarino, 2005). The modified forcing term can be solved for at each time step using

the approximate numerical solution, then included in the system to find the true solution. The boundary forcing can be implemented using interpolation over the boundary with "ghost cells" inside the solid body (DeLeon et al., 2018; Fedkiw, 2002). The ghost cell method allows for the topography to arbitrarily intersect the boundary, but relies on geometric interpolation to employ accurate boundary conditions (DeLeon et al., 2018). This technique also requires a thick enough boundary to account for the number of layers of "ghost cells" for the desired order of accuracy of the interpolation (Seo and Mittal, 2011).

The grid-fitted IBM offers an alternative to the ghost-cell approach that satisfies the conservation laws for fluid, especially appealing for an FVM simulation. By assuming the boundary always intersects the nodes of the grid, the resulting surfaces take on a stair-step or jagged appearance instead of being smooth (Fig. 2.1c). While the boundary itself is now an approximation ($\Gamma_b'$), the boundary conditions are applied at cell faces, mimicking the usual application of boundary fluxes in a finite volume. The grid-fitted or cut-cell approach maintains strict conservation of mass, momentum, and energy within the model, without adding truncation errors or computational cost from the interpolation scheme. Many LES models use a grid-fitted representation to solve geophysical problems (Ye et al., 1999; Briscolini and Santangelo, 1989; Chung, 2006), and topography data, such as the elevation of the sea floor, is often defined on grids, making coincidental boundaries common in ocean applications.

For continuous forcing, the governing equations are modified to enforce the boundary conditions before discretization, whereas with discrete forcing, they are modified within the simulation. While the continuous method might seem computationally cheaper, it requires the use of problem-specific parameters that the user would have to tune themselves (Mittal and Iaccarino, 2005; Nasr-Azadani and Meiburg, 2011). Such tuning would require every user to have an in-

depth knowledge of IBM, not realistic for a public model such as Oceananigans (Wagner et al., 2025a; Nasr-Azadani and Meiburg, 2011; Mittal and Iaccarino, 2005). In contrast, the discrete method has no added parameters or stability limitations. The grid-fitted, discrete IBM will conserve fluid properties and model sharp boundaries, making it an ideal candidate for implementing topography in turbulent fluid simulations such as Oceananigans (Wagner et al., 2025a; Mittal and Iaccarino, 2005).

## 2.3 Grid-Fitted IBM Implementation

### 2.3.1 Model Formulation

With recent pushes for updating the commonly used modeling practices and parameters to include the advances in science, data collecting, and numerics, the Climate Modeling Alliance (CliMA) aims to build a climate model from scratch that will simulate small-scale ocean physics at high resolutions (Schneider et al., 2017). As part of this project, they are developing the "fast and friendly" software package, Oceananigans, to solve the incompressible fluid problems of the ocean (Ramadhan et al., 2020). Written in Julia, the package supports LES and DNS on both CPUs and GPUs (Wagner et al., 2025a). Oceananigans aims to create a user-friendly interface, allowing researchers to "focus on the science," while relying on algorithms that will run as fast as possible (Ramadhan et al., 2020). While Oceananigans has a functioning LES package, the group continues to improve the algorithms and add more capabilities for scientists to utilize.

Oceananigans implements both a hydrostatic free-surface model and a non-hydrostatic model, both incompressible with the Boussinesq approximation (Wagner et al., 2025a). For Chapters 2 through 4, the non-hydrostatic formulation is used to more accurately represent the

strong vertical accelerations, wave breaking, and localized mixing events that violate the hydrostatic assumption (Gill, 1982). As many of the ocean questions addressed in this work rely on accurately representing turbulence, most of the following analysis will use an explicit LES with the Smagorinsky-Lilly closure. In this case, no background viscosity or diffusivity is set in the model, but the turbulent Prandtl number is set to $Pr_t = 1$, with a parametrized turbulent diffusivity and viscosity (Wagner et al., 2025a). Some of the following validation will also include DNS with a set background viscosity. The highest order advection scheme currently available in Oceananigans is the ninth-order weighted essentially non-oscillatory (WENO) (Wagner et al., 2025a). This method adds an implicit component to the model, which could generate some numerical dissipation in the simulations. It has been shown that using an explicit closure, such as Smagorinsky-Lilly, with a WENO scheme is the best available combination for calculating turbulence statistics in LES (Pressel et al., 2017). The following description of the grid-fitted IBM in Oceananigans is from the current implementation (version 0.100.7, (Wagner et al., 2025b)), and more details can be found in the publicly available Julia package (Wagner et al., 2025b).

Building on the general description of IBM implementation provided in section 2.2, this section details the grid-fitted implementation used in Oceananigans. Consider the incompressible Navier–Stokes equations under the Boussinesq approximation, as used in the non-hydrostatic Oceananigans model (ignoring background fields and Stokes drift; Wagner et al., 2025a), together

with a general tracer conservation equation.

$$\frac{\partial \boldsymbol{u}}{\partial t} = -(\boldsymbol{u} \cdot \nabla)\boldsymbol{u} - (f \times \boldsymbol{u}) - \nabla p + b\vec{\boldsymbol{k}} - \nabla \cdot \boldsymbol{\tau} + \boldsymbol{F_u} \tag{2.6}$$

$$\frac{\partial c}{\partial t} = -(\boldsymbol{u} \cdot \nabla)c - \nabla \cdot \boldsymbol{q_c} + F_c \tag{2.7}$$

$$\nabla \cdot \boldsymbol{u} = 0, \tag{2.8}$$

where $\boldsymbol{u}$,c are the velocity vector and tracer, $f$ is the Coriolis parameter, $p$ is the kinematic pressure, $b$ is the buoyant acceleration in the vertical direction, $\boldsymbol{\tau}$ is the kinematic stress tensor, $\boldsymbol{q_c}$ is the diffusive flux, and $\boldsymbol{F_u}, F_c$ are arbitrary forcing functions on the velocity field and tracer respectively. The reference density $\rho_0$ is implicitly included in the kinematic terms. $\boldsymbol{\tau}, \boldsymbol{q_c}$ could represent molecular or turbulent viscous stress and diffusive fluxes, depending on which closure the model uses (Ramadhan et al., 2020; Wagner et al., 2025a).

After discretization, the time integral of the momentum equation is given by the following,

$$\begin{aligned}
\boldsymbol{U}^{n+1} - \boldsymbol{U}^n &= \int_{t_n}^{t_{n+1}} \Big[ -\boldsymbol{\nabla} p_{non} - \boldsymbol{\nabla} p_{hyd} - (\boldsymbol{U} \cdot \boldsymbol{\nabla})\boldsymbol{u} - f \times \boldsymbol{U} - \boldsymbol{\nabla} \cdot \boldsymbol{\tau} + \boldsymbol{F_u} \Big] dt \\
&= \int_{t_n}^{t_{n+1}} \Big[ -\boldsymbol{\nabla} p_{non} + \boldsymbol{G_u} \Big] dt \\
&\approx -\Delta t \boldsymbol{\nabla} p_{non}^{n+1} + \int_{t_n}^{t_{n+1}} \boldsymbol{G_u} dt,
\end{aligned}$$

(Ramadhan et al., 2020). Oceananigans implements a fractional step method where non-hydrostatic pressure, $\boldsymbol{\nabla} p_{non}$, is treated implicitly, while the rest of the terms on the right-hand side, defined as the tendency, $\boldsymbol{G_u}$, are treated explicitly (Ramadhan et al., 2020). The non-hydrostatic pressure

is calculated to ensure that the velocity field at $n+1$ is divergence-free. For the tracer equations,

$$\boldsymbol{C}^{n+1} - \boldsymbol{C}^{n} = \int_{t_n}^{t_{n+1}} G_c dt \tag{2.9}$$

(Wagner et al., 2025a). Oceananigans uses a third-order Runge-Kutta scheme with pressure correction (Le and Moin, 1991). At the $k$th stage of the time stepper, the velocity is updated by

$$\boldsymbol{U^k} = \boldsymbol{U^k} + \gamma^k \Delta t \boldsymbol{G}^k + \zeta^k \Delta t \boldsymbol{G}^{k-1}, \tag{2.10}$$

where $\boldsymbol{G}^k$ is the tendency calculated prior to the $k$th stage of the time stepper and $\gamma^k, \zeta^k$ are Runge-Kutta coefficients. Then the velocity is corrected for the non-hydrostatic pressure by

$$\boldsymbol{U^k} = \boldsymbol{U^k} - \boldsymbol{\nabla} p^k_{non} \Delta t (\gamma^k + \zeta^k). \tag{2.11}$$

It is within this part of the model that the IBM forcing is added directly to the calculation of $\boldsymbol{G_u}, G_c$, between the Runge-Kutta sub-step and the pressure correction of the velocity. Similar to (2.5), calculated boundary flux divergences are removed while forcing is added for the prescribed boundary condition. The pressure correction step enforces incompressibility in the model, but applying it after the IB enforcement can introduce boundary errors or leakage. To reduce unphysical divergences at the boundary, cells inside the IB are masked within the pressure solver (Wagner et al., 2025a). Nonetheless, there remains a tradeoff (mitigated by the iterative pressure solver) between strictly enforcing the boundary conditions and maintaining exact incompressibility (Wagner et al., 2025a).

### 2.3.2 Immersed node classification

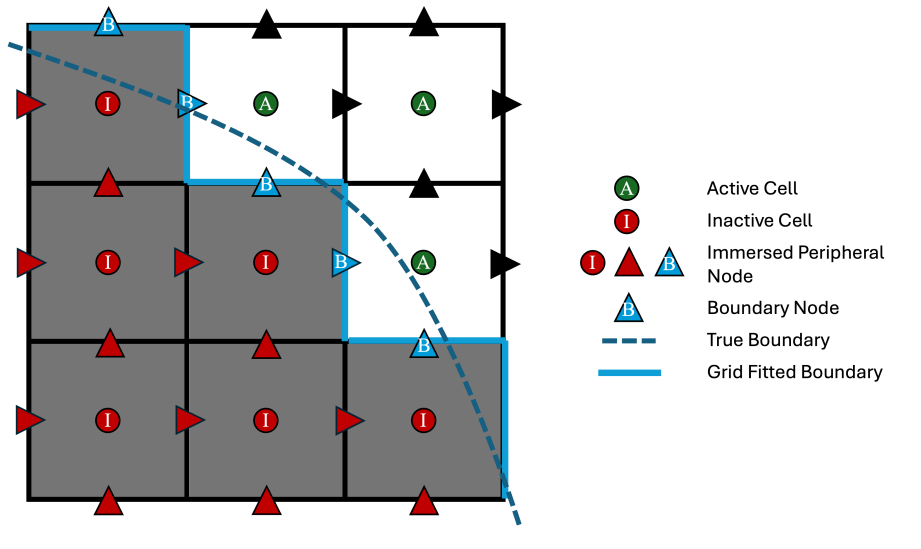



Figure 2.2: Classification of immersed nodes in Oceananigans using an example boundary (dashed line) and the resulting grid-fitted topography (gray cells). Arrows indicate the location of staggered velocity nodes, while circle markers are the centered tracer nodes. Tracer nodes are marked ”A” for active and ”I” for inactive cell classification.

To know where to modify the tendencies, the nodes must be classified based on their location with respect to a given boundary. Oceananigans uses a staggered Arakawa C-grid, which shifts the evaluation of the vector quantities, like velocities, to the faces of the finite volume surrounding a tracer node (Ramadhan et al., 2020). Therefore, classification must be done for both the cell centers and the faces. A user can specify an IB using a Boolean function or an array that returns `true` for locations within the topography. Based on this given boundary definition, the grid first classifies if tracer cells are “active” or “inactive,” where active means in the fluid. Fig. 2.2 shows an example classification, where the active and inactive cells are marked at the cell centers by “A” and “I” respectively. All immersed inactive cells also fall into the larger category of “immersed peripheral nodes.” The faces of the cells are also classified as immersed peripheral

nodes if at least one of the cell centers on either side of that face is an inactive cell (red and blue triangles, Fig. 2.2). Boundary nodes are immersed peripheral nodes on faces with an active cell on one side (blue triangles, Fig. 2.2).

The IBM only holds at boundary nodes where boundary conditions exist, so thought must be given to the immersed peripheral nodes not located on the boundary. For direct forcing methods, little difference was found between applying forcing within the body and leaving the fields free to develop an unphysical flow (Fadlun et al., 2000). For the implementation in Oceananigans, IBM enforcement is done on all peripheral nodes. Then, once the fields are updated (along with the non-hydrostatic pressure correction (Ramadhan et al., 2020)), $\boldsymbol{U}^{k+1}, C^{k+1}$ are masked to zero at all immersed peripheral nodes, removing any unphysical flows or tracers before the next calculation step.

### 2.3.3 Boundary conditon enforcement

The FVM makes adding flux boundary conditions to a certain cell relatively simple and numerically stable. For simplicity, consider the tracer equation, though all methods follow in the same manner for momentum as the tracer implementations. The average of the tracer equation (2.7) over a finite volume, $V_{i,j,k}$, gives the tendency $G_c|_{i,j,k}$ in that volume,

$$G_c|_{i,j,k} = -\frac{1}{V_{i,j,k}} \oint_{\partial\Omega_{i,j,k}} (\boldsymbol{u}c + \boldsymbol{q_c}) \cdot \vec{\boldsymbol{n}} dS + \int_{V_{i,j,k}} F_c dV, \tag{2.12}$$

where $\partial\Omega_{i,j,k}$ is the surface integral over the six faces of the cell. All external boundaries are required to have a no-penetration condition on velocities normal to the cell face ($\boldsymbol{u}\cdot\vec{\boldsymbol{n}} = 0$), so the only fluxes along immersed boundary faces should come from a prescribed boundary condition

($q_c|_{BC} = \boldsymbol{q}_c \cdot \vec{\boldsymbol{n}}|_{\partial\Omega_b}$). The normally calculated viscous stress or diffusive flux terms in the model are set to zero on immersed peripheral nodes. Then these terms are replaced by the addition of the immersed boundary condition flux on that face. For example, assume the bottom face of a volume, $V_{i,jk}$, has a prescribed flux $q_c|_b$. The convention is that fluxes are directed inward-facing normal, such that a positive flux boundary condition on the "right" face of a cell (top, north, and east) will result in a decrease in boundary-adjacent cell values. Then the addition to the tendency for that boundary face is given by

$$-\frac{1}{V_{i,j,k}} \int_{A_{i,j}} q_c|_b \,\text{sign}(\vec{\boldsymbol{n}}) dA = -\frac{q_c|_b A_{i,j}}{V_{i,j,k}}, \tag{2.13}$$

where $A_{i,j}$ is the area of the bottom face the flux comes from. Assuming that all faces fall on an immersed periphery node, the full tendency correction for all faces is

$$G_c|_{i,j,k} - \frac{1}{V_{i,j,k}} \oint_{\partial\Omega_{i,j,k}} q_c|_{BC} \,\text{sign}(\vec{\boldsymbol{n}}) dS = G_c|_{i,j,k} + \frac{1}{V_{i,j,k}} \sum_{\alpha \in \{i,j,k\}} (q_c|_\alpha^+ A^{\alpha+} - q_c|_\alpha^- A^{\alpha-}) \tag{2.14}$$

where ($\pm$) notation indicates the left and right faces of the cell in the $\alpha$ direction, and $A^{\alpha\pm}$ is the area of the $\alpha$ face (eg. $A^{i-} = A_{j,k}$). Each of these fluxes, $q_c|_\alpha^\pm$, are only included if that face is classified as an immersed periphery node. Therefore, enforcing a flux boundary condition on a field is as simple as adding a new immersed flux divergence to the tendency term, which is only non-zero on immersed peripheral nodes.

While flux boundary conditions, such as bottom drag or a heat loss from an ice shelf, are one of the most commonly used boundary conditions in oceanography simulations, there are also times when a prescribed boundary value (Dirichlet) or gradient across the boundary (Neumann)

would be useful. Due to the simplicity of implementing the immersed flux boundary conditions in the FVM, gradient and value boundary conditions are interpolated into related boundary fluxes for a consistent enforcement method across all available boundary conditions. This is possible because all turbulent closures implemented in Oceananigans currently have the property that the fluxes $(\boldsymbol{\tau}, q_c)$ are proportional to the gradient of the field. For a gradient boundary condition, the diffusivity, $\kappa$, or viscosity, $\nu$, along with the given boundary-normal gradient, $\frac{\partial c}{\partial n}$, are used to derive a prescribed boundary flux,

$$q_c|_b = -\kappa \frac{\partial c}{\partial n}, \tag{2.15}$$

where $\kappa$ (or $\nu$ equivalently) is either a set molecular value, in the case of a DNS simulation, or the turbulent eddy value from a turbulence closure in LES. For a value boundary condition, the value is extrapolated into a near-boundary gradient, which is then used to get the desired boundary flux. With a known boundary value, $c_b$, and the cell value at which the fluxes are being calculated, $c_{i,jk}$, linear interpolation over the half grid cell distance $\Delta x, \Delta y$, or $\Delta z$ between the two values gives the gradient. For example, if the boundary is on the bottom face of a grid cell, then the flux is given by

$$q_c|_b = -\kappa \frac{c_{i,j,k} - c_b}{\Delta z/2}. \tag{2.16}$$

From the derivation of this boundary flux, the gradient and value formulation follow the same steps as the case of a directly given flux boundary condition (2.14).

The grid-fitted immersed boundary implementation in Oceananigans is facilitated by the finite-volume framework, which allows immersed boundary fluxes to be incorporated directly by replacing the calculated diffusive fluxes on immersed peripheral nodes with the prescribed boundary condition. Because all turbulent closures in Oceananigans relate fluxes to field gra-

dients, value and gradient boundary conditions can be consistently reformulated as equivalent fluxes, maintaining a unified enforcement method across all boundary types. Given boundary values are translated into gradients by local linear interpolation (2.16; then gradient boundary conditions are related to fluxes by the viscosity or diffusivity of the field 2.15. The ability of this grid-fitted formulation to reproduce theoretical results for bottom boundary Ekman flows is demonstrated through a series of validation studies presented below.

## 2.4 Validation Ekman Theory

To describe bottom Ekman dynamics along sloping topography, it is convenient to use a rotated coordinate system aligned with the slope at angle $\alpha$, with across-slope and slope-normal unit vectors $(\vec{\boldsymbol{s}}, \vec{\boldsymbol{n}})$ related to the Cartesian basis $(\vec{\boldsymbol{i}}, \vec{\boldsymbol{j}})$ by

$$\begin{bmatrix} \vec{\boldsymbol{s}} \\ \vec{\boldsymbol{n}} \end{bmatrix} = \begin{bmatrix} \cos\alpha & \sin\alpha \\ -\sin\alpha & \cos\alpha \end{bmatrix} \begin{bmatrix} \vec{\boldsymbol{i}} \\ \vec{\boldsymbol{k}} \end{bmatrix}. \tag{2.17}$$

Rotated variables are denoted by $\hat{(\cdot)}$. In this coordinate system, the Coriolis vector becomes $\hat{\boldsymbol{f}} = f\sin\alpha\vec{\boldsymbol{s}} + f\cos\alpha\vec{\boldsymbol{n}}$, and the buoyancy vector, $b\boldsymbol{k} = b\sin\alpha\boldsymbol{s} + b\cos\alpha\boldsymbol{n}$.

Assuming a steady barotropic interior flow $\boldsymbol{V} = (0, V_0, 0)$ and uniform background stratification $N_0^2$, perturbations in velocity, buoyancy, and pressure $(\hat{\boldsymbol{u}}, b, p)$ satisfy the incompressible Boussinesq equations given in (2.6-2.8). The governing equation for buoyancy is given by,

$$\frac{\partial b}{\partial t} + (\hat{\boldsymbol{u}} + \boldsymbol{V}) \cdot \nabla b + \hat{u}N_0^2\sin\alpha + \hat{w}N_0^2\cos\alpha = \nabla \cdot q_b, \tag{2.18}$$

where $q_b$ is the diabatic flux, incorporating parameterized contributions. Boundary conditions include prescribed bottom stress $\boldsymbol{\tau}_b^{\hat{x},y}$ and no-flow conditions on $\hat{w}$, as well as no-flux on $b$. Stresses vanish far above the boundary layer. Averaging across a theoretically infinite slope isolates the Ekman balance.

$$\frac{\partial \langle \hat{u} \rangle}{\partial t} - f \langle v \rangle \cos\alpha = \langle b \rangle \sin\alpha + \frac{\partial \langle \tau^{\hat{x}} \rangle}{\partial \hat{z}} \tag{2.19}$$

$$\frac{\partial \langle v \rangle}{\partial t} + f \langle \hat{u} \rangle \cos\alpha = \frac{\partial \langle \tau^{y} \rangle}{\partial \hat{z}} \tag{2.20}$$

$$f \langle v \rangle \sin\alpha = -\frac{\partial \langle p \rangle}{\partial \hat{z}} + b\cos\alpha + \frac{\partial \langle \tau^{\hat{z}} \rangle}{\partial \hat{z}} \tag{2.21}$$

$$\frac{\partial \langle b \rangle}{\partial t} + \langle u \rangle N_0^2 \sin\alpha = -\frac{\partial}{\partial \hat{z}} \langle w' b' \rangle + \nabla \cdot \langle q_b \rangle, \tag{2.22}$$

where primes indicate departures from the across-slope averaging, denoted by $\langle \cdot \rangle$. The reference density will continue to be implicitly included in kinematic terms for consistency with (2.6-2.8). The boundary conditions on the slope normal velocity, along with the averaged continuity equation, necessitate that $\langle w \rangle = 0$. These terms have been removed from the balances above.

Friction near the wall shears the mean flow, producing a Coriolis-induced across-slope transport within the developing BBL. The balance between Coriolis and viscous stress yields an exponentially decaying velocity profile, the Ekman spiral, with characteristic Ekman depth $\delta_e$. For an unstratified, laminar flow with constant viscosity $\nu$, buoyancy vanishes, and the reduced Ekman balance in steady-state becomes,

$$-f \langle v \rangle \cos\alpha = \frac{\partial \langle \tau^{\hat{x}} \rangle}{\partial \hat{z}} \tag{2.23}$$

$$f \langle \hat{u} \rangle \cos\alpha = \frac{\partial \langle \tau^{y} \rangle}{\partial \hat{z}}. \tag{2.24}$$

The analytical solution of (2.23-2.24) gives the laminar Ekman depth,

$$\delta_e = \sqrt{\frac{2\nu}{f\cos\alpha}}. \tag{2.25}$$

In unstratified turbulent conditions, molecular viscosity is replaced by a parametrized eddy viscosity, and the Ekman depth can be expressed in terms of the friction velocity, $u^* = \sqrt{|\boldsymbol{\tau_b}|}$, again with an implicit reference density. The corresponding turbulent Ekman depth is then

$$\delta_e^* = \frac{\kappa_{vk} u^*}{f\cos\alpha} \tag{2.26}$$

(Coleman et al., 1990), where $\kappa_{vk} = 0.4$ is the von Kármán constant. In the stratified ocean, buoyancy forces oppose the turbulent mixing that deepens the layer, yielding a reduced effective Ekman depth

$$\delta_e^* = \frac{\kappa_{vk} u^*}{\sqrt{N_0 f\cos\alpha}} \tag{2.27}$$

(McWilliams et al., 2009). Stratification thus limits cross-isopycnal transport and can ultimately arrest the Ekman circulation (Garrett et al., 1993; Brink and Lentz, 2010).

When downslope Ekman transport advects light water beneath dense, buoyancy fluxes erode stratification and potential vorticity (PV), potentially driving symmetric instability (SI) (Wenegrat and Thomas, 2020). For large slope Burger numbers ($S_0 = \tan\alpha N_0/f > 1$), this low PV environment promotes SI that restores the boundary layer toward marginal stability (PV $\approx 0$) (Allen and Newberger, 1998; Wenegrat and Thomas, 2020). The resulting low-PV layer thickness depends strongly on the along-slope stress $\langle \tau^y \rangle$, making it a topographically-sensitive diagnostic of boundary-layer adjustment over topography (Wenegrat and Thomas, 2020).

The bottom Ekman transport is also dependent on the boundary stress and sloping topography (Brink and Lentz, 2010). Vertically integrating (2.19–2.22) and assuming vanishing stress above the boundary layer gives the across-slope Ekman transport before buoyancy arrest,

$$U_E = \int_0^\infty \hat{u} d\hat{z} = -\frac{\langle \tau_b^y \rangle}{f(1+S_0^2)} \tag{2.28}$$

(Brink and Lentz, 2010). This expression for the transport holds regardless of the structure of the velocity, depending only on the local bottom stress and slope.

Validation will include simulations of unstratified laminar and turbulent flows and several stratified Ekman flows along sloping topography. Together, the relationships discussed above provide a theoretical framework for interpreting the modeled boundary-layer structure, transport, and stability. Examining these theoretical scalings and balances in numerical simulations will assess how well the grid-fitted topography reproduces the canonical rotation–friction balance of the bottom Ekman layer.

## 2.5 Validation Set Up

To explore Ekman BBL flows, we used LES and DNS, with the non-hydrostatic model in Oceananigans (Wagner et al., 2025b). A ninth-order WENO scheme advects velocities and tracers, with a third-order Runge–Kutta time-stepping method (Wagner et al., 2025b). Poisson's equation for the non-hydrostatic pressure is solved using a rapidly-converging conjugate gradient method, with a fast Fourier transform-based solver as a preconditioner (Wagner et al., 2025b). The laminar simulations were run with a constant viscosity of $\nu = 10^{-3}$ m$^2$s$^{-1}$, while the turbulent simulations employed the explicit Smagorinsky–Lilly subgrid-scale model for the LES

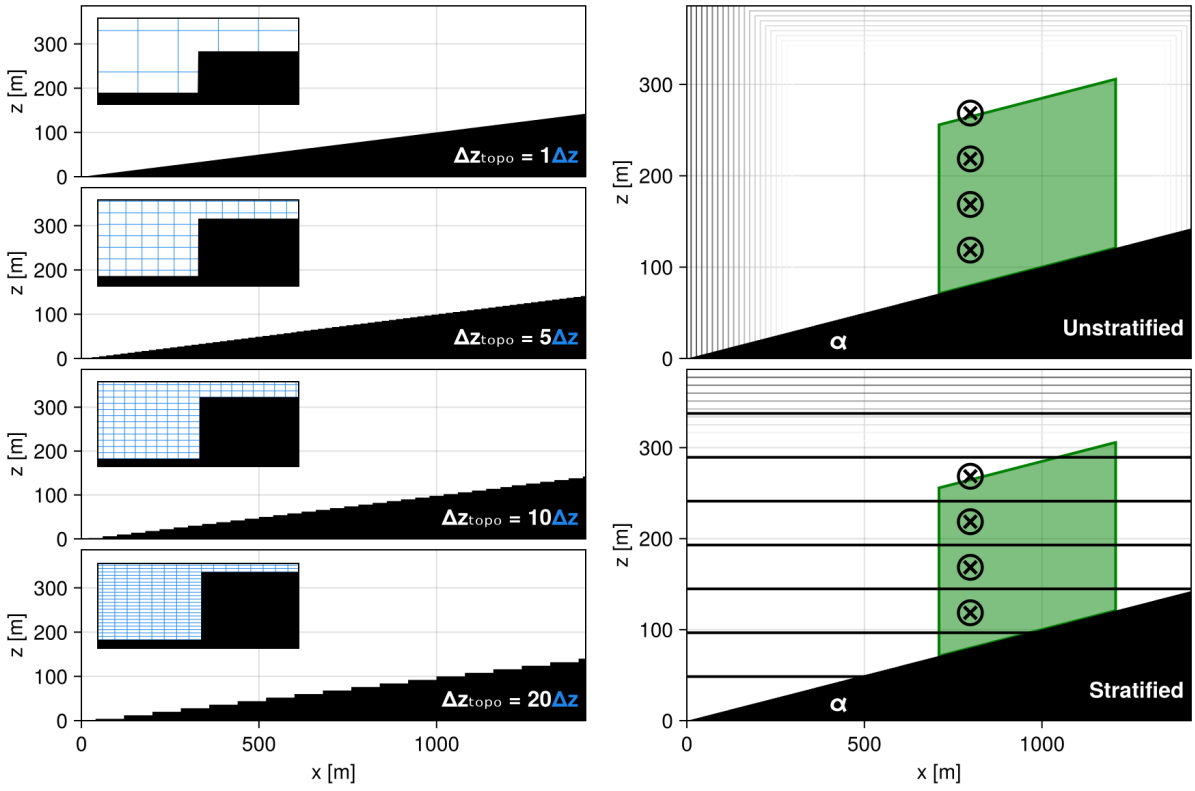



Figure 2.3: The topographic grid resolution ($\Delta z_{topo}$) is shown for all topography tested (left). Subplots show a representative step with the comparative size of the interior fluid grid cells (in blue). The numerical model domain setup for all simulations is depicted (right), with initial conditions consisting of a uniform barotropic flow ($v > 0$) and uniform stratification, when applicable (buoyancy contours indicated by black lines). Sponge regions are shown by thin gray lines. The green regions represent the part of the domain used for analysis, to exclude domain effects.

turbulence closure, with a turbulent Prandtl number of $1.0$. Note that the simulations are two-dimensional, capturing the bulk flow organization relevant to this study, but not the full three-dimensional turbulence cascade or dissipation processes. Simulations were run for at least $10$ inertial periods ($T_f$) with a variable time step given by a CFL of $0.5$ and outputs every $\frac{1}{30}\,T_f$.

The domain, shown in Fig. 2.3, is two-dimensional, with size $(L_x, L_z) = (1420, 386)$ m, with uniform grid spacing of $\Delta x = 0.8$ m and $\Delta z = 0.4$ m. In all simulations, an $80$ m sponge was applied to the top of the domain, damping velocities back to zero (Fig. 2.3, bottom right)

Table 2.1: Validation Simulation Parameters

| Parameter | Unstratified | Stratified | | |
|---|---|---|---|---|
| $N_0^2$ [s$^{-2}$] | 0 | $1.2 \times 10^{-6}$ | $2 \times 10^{-6}$ | $3 \times 10^{-6}$ |
| $V_0$ [ms$^{-1}$] | 0.1 | 0.1 | 0.1 | 0.1 |
| $f$ [s$^{-1}$] | $3.8 \times 10^{-5}$ | $10^{-4}$ | $10^{-4}$ | $10^{-4}$ |
| $\nu$ [m$^2$s$^{-1}$] | $10^{-3}$ | NA | NA | NA |
| $\alpha$ [°] | 5.7 | 5.7 | 5.7 | 5.7 |
| $C_D$ | $5.7 \times 10^{-3}$ | $5.7 \times 10^{-3}$ | $5.7 \times 10^{-3}$ | $5.7 \times 10^{-3}$ |
| $S_0^2$ | - | 1.2 | 2.0 | 3.0 |
| $\delta_e$ [m]$^+$ | 7.31, 34.41 | 1.85 | 1.49 | 1.28 |

$^+$Values determined by frictional estimates using equations (2.26, 2.27) for LES simulations

to avoid wave reflection. In the unstratified simulations, horizontal sponges were also required over 300 m on the offshore edge ($x = 0$ m) and 90 m onshore ($x = 1420$ m). The thin gray contours in Fig. 2.3 indicate the sponge regions in the stratified and unstratified simulations, with the magnitude given by the relative damping rates. To avoid domain effects and get as close as possible to an "infinite" slope, the region used for analysis only includes values between $x = 710$ and 1206.8 m (green region, Fig. 2.3). Topography was included in the simulation using a grid-fitted IBM with a steady slope given by $\alpha = 5.7\,^\circ$.

To understand the effects of the grid-fitted topography on Ekman flows, the slope topography was coarsened, maintaining the original grid resolution. This ensures that any degradation in the results is due to the topographic discretization itself, rather than differences in the resolved fluid scales. The ratio between the horizontal and vertical grid resolution was also kept constant. The four topographic resolutions ($\Delta z_{\text{topo}}$) tested were $1, 5, 10,$ and $20$ times the grid resolution. Fig. 2.3 shows the relative step size for each $\Delta z_{\text{topo}}$ compared to the grid resolution, with the most refined topography, $\Delta z_{topo} = 1\Delta z$, having a step size the same height as the grid cell. Length

scales in plots, along with the coarsening of the topography, will be normalized by the relevant Ekman depth for each simulation. In the laminar simulations, the $\delta_e$ for constant viscosity (2.25) will be used, while for the LES, the relevant $u^*$ approximation, $\delta_e^*$ in (2.26, 2.27), will be used.

The simulations are all started from rest, with a steady background flow of $V_0 = 0.1$ ms$^{-1}$. Assuming the model does not resolve the viscous sublayer, a quadratic drag boundary condition, with drag coefficient $C_d$ and a model-implicit viscosity $\nu$, is set as

$$\nu \frac{\partial}{\partial z}(u, v)|_b = -C_d(u_b, v_b + V_0)|\boldsymbol{u}_b|, \tag{2.29}$$

where $u, v_b$ is the bottom velocity along the topography. All other boundary conditions are no flux. The drag coefficient, $C_D$, along with other relevant simulation parameters are found in Table 2.1. Three values of uniform initial stratification, $N_0^2$, were tested, ranging from $1.2 \times 10^{-6}$ s$^{-2}$ to $3 \times 10^{-6}$ s$^{-2}$. Holding the slope angle and Coriolis constant, the three stratified simulation groups cover a slope Burger number ($S_0^2$) between 1.2 and 3, well within the range where SI can dominate the boundary-layer evolution (Wenegrat and Thomas, 2020). See Table 2.1 for more parameter details.

## 2.6 Validation Results

### 2.6.1 Validation Case 1: Unstratified, Laminar Ekman

The laminar case quickly reaches a steady state with downslope flow in $\hat{u}$, along with a decrease in the along-slope flow, $v + V_0$, near the boundary. Fig. 2.4 shows a representative time step ($t = 10\, T_f$) after the simulations reach steady-state for the most well-resolved topography

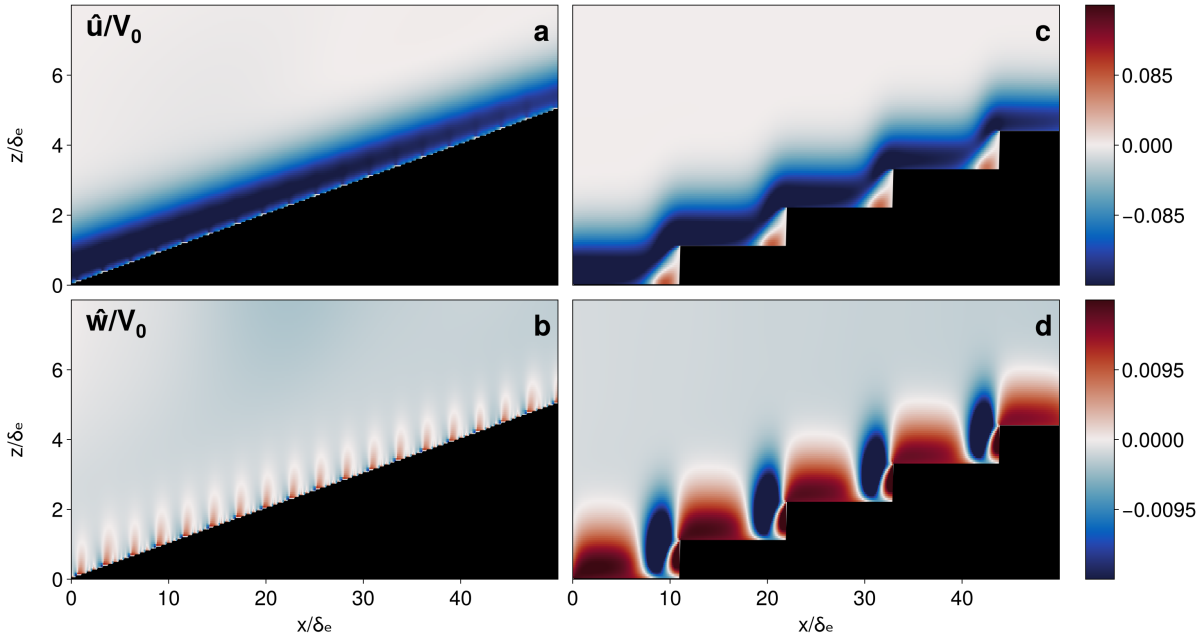



Figure 2.4: Steady-state flow structure of the unstratified, laminar Ekman layer for the finest (a-b) and coarsest (c-d) topography of (a,c) the across-slope velocity, $\hat{u}$, and (b,d) the slope-normal velocity, $\hat{w}$.

simulation ($\Delta z_{\text{topo}}/\delta_e = 0.05$) and the coarsest topography ($\Delta z_{\text{topo}}/\delta_e = 1.09$). Near the boundary, alternating positive and negative vertical velocities develop with magnitudes and length scales correlated with the topographic resolution (Fig. 2.4b,d). Along with the small upslope velocities visible in the coarsest topography simulation (Fig. 2.4c), these are consistent with small overturning circulations along the steps, due to the vertical walls. In the case of an equivalently coarse interior grid and topography, these circulations would be smaller than the grid-scale and could resemble the weaker velocities in the refined case where the topographic and true grid resolution are the same (Fig. 2.4a,b).

Averaging across slope and in time after steady-state is reached, representative 1D profiles can be used to compare to theory. The profiles of $\hat{u}, v$ in Fig. 2.5a,b indicate some differences in the profile below the depth of the topography "step" size, most likely due to the recirculating flow

along the steps (Fig. 2.4). For the coarsest topography, this corresponds to 1.09 $\delta_e$, marked as the horizontal red line in Fig. 2.5(a,b), where there is a sharp bend in the $\hat{u}$ profile. Hodographs of $\hat{u}, v$ in the finest topography resolution of $0.05\delta_e$ show a qualitatively correct Ekman spiral, while, with decreasing topographic resolution, there is a similar discontinuity at the depth of the topographic step (Fig. 2.5c). Variations below the step size are not expected to be significant on coarsely resolved grids matching the coarse topography, since any inaccuracies at those scales would only extend over a single grid cell. The flow structure above the step size shows good agreement, with the most prominent changes in Fig. 2.5 (a-c) occurring in the coarsest simulation, where $\Delta z_{\text{topo}}$ does not resolve the Ekman depth. Since the slope-normal velocities are an order of magnitude smaller than the downslope Ekman transport, the associated errors have minimal influence on the across-slope mean structure. Their role may, however, become more significant in cases with weaker Ekman transport or in different problems where cross-slope variability is important.

Theory indicates that the magnitude of the profiles, $|u|$, should behave exponentially, with an Ekman depth dependence, such that

$$|u| \propto e^{-\hat{z}/\delta_e}. \tag{2.30}$$

Using a nonlinear, least-squares regression on the profiles in Fig. 2.5(a,b), the fitted Ekman depth, $\delta_e^{\text{fit}}$, is found for each simulation and normalized by the true theoretical $\delta_e$, calculated by (2.25). The most refined topography is the furthest from the true theoretical value (Fig. 2.5d), but this is most likely caused by damping near the sponge layers and the presence of vertical and horizontal walls, which are absent in the idealized infinite-slope assumed by the theory. There is a small

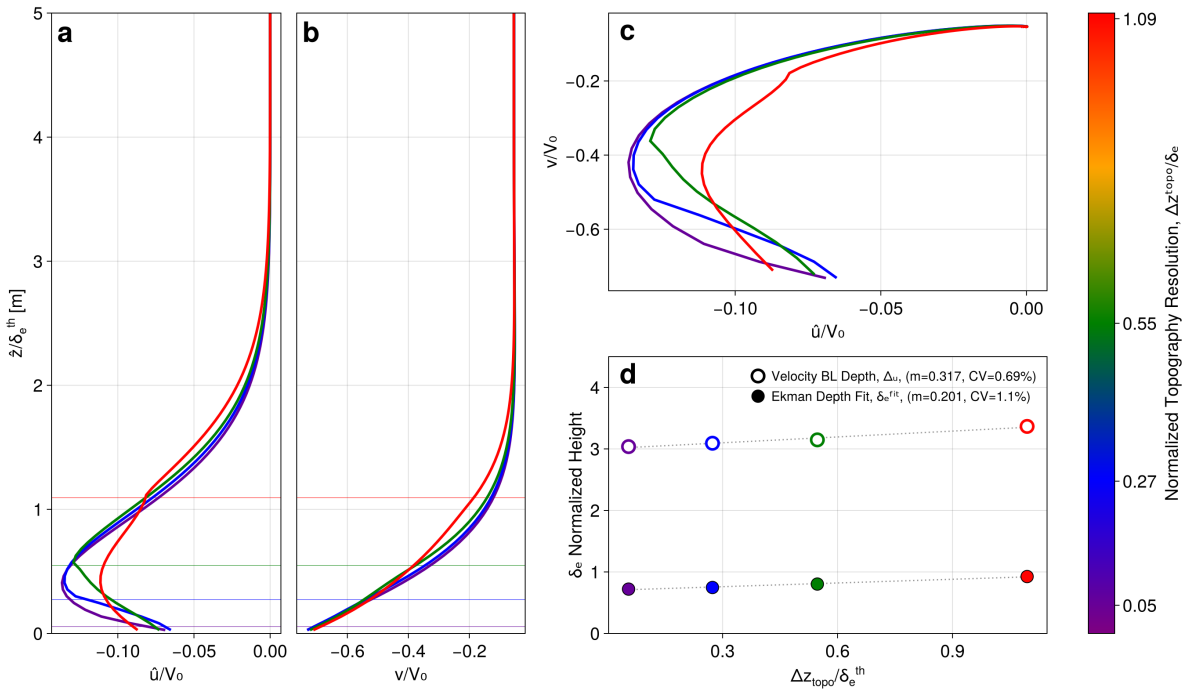



Figure 2.5: Comparison of 1D laminar simulation characteristics over all topography coarsenings, after averaging across-slope and in time. (a,b) are the steady state flow profiles of $\hat{u}, v$. Colors correspond to the topography coarseness, with the depth of the "stairs step" marked by horizontal lines as well. (c) is the hodograph of the characteristic spiral between $\hat{u}, v$. (d) is the fit of the Ekman depth based on the expected exponential profile, along with the calculated $u$ boundary layer. Statistics in the legend include the slope of the best-fit line, m, and the characteristic of variation, CV, for each parameter.

upward trend of $0.201\,\delta_e^{\text{fit}}/\Delta z_{\text{topo}}$ in the normalized results. The coefficient of variation (CV) is defined as the standard deviation of the results normalized by the mean. It can be thought of as a normalized measure of "flatness," where a CV of less than three percent indicated good agreement over increased topographic step size. The CV of the $\delta^{\text{fit}}$ results for the laminar case is $1.1\%$, showing that even with the changes in the profile below the topographic resolution, the resulting Ekman depth remains essentially steady. As another measure of the impact of the topography on the profile, the boundary-layer height from the across-slope transport in $\hat{u}$ was measured as the height where it is damped to less than $10^{-3}\,V_0$, which should be at $3\delta_e$. The calculated values

from each topographic size (open markers, Fig. 2.5d) show a moderate increase in the boundary-layer height ($m = 0.317\,\Delta_u/\Delta z$) with increased topographic coarseness. The CV for the laminar boundary layer is only $0.69\%$. While the profiles in Fig. 2.5a,b indicate some irregularities near the topographic resolution, made worse when the Ekman depth is no longer resolved, the bulk characteristics are consistent for laminar Ekman flow over topographic resolutions ranging from $0.05$ to $1.09\,\delta_e$.

### 2.6.2 Validation Case 2: Unstratified, Turbulent Ekman

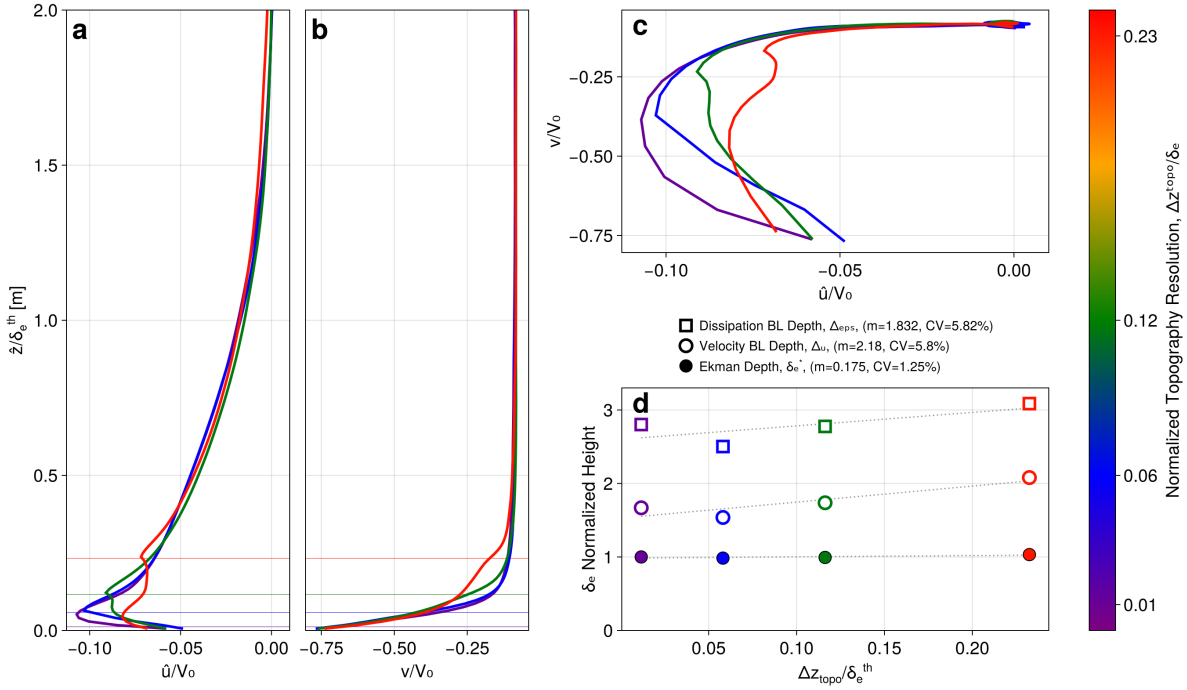



Figure 2.6: Comparison of 1D turbulent simulation characteristics over all topography coarsenings, after averaging across-slope and in time. (a,b) are the steady-state flow profiles of $\hat{u}, v$. Colors correspond to the topography coarseness, with the depth of the "stairs step" marked by horizontal lines as well. (c) is the hodograph of the characteristic spiral between $\hat{u}, v$. (d) is the fit of the Ekman depth based on the expected exponential profile, along with a calculation of the BBL using the $u$ velocity ($\Delta_u$) and the dissipation of KE rate, $\epsilon$, ($\Delta_{eps}$). Statistics in the legend include the slope of the best-fit line, m, and the characteristic of variation, CV, for each parameter.

In the turbulent simulations, the bottom Ekman layer is much larger than the laminar case as resolved eddies transport momentum away from the boundary. Due to the larger Ekman depths found in the turbulent simulation, all $\Delta z_{\text{topo}}$ resolve the calculated Ekman depth. While the parameter space is limited in $\delta_e$ space, the following results will show differences in the BBL height and in the size of vortices generated during the onset of turbulence from the impact of the grid-fitted boundary.

Similar to the laminar simulations, there are some irregularities in the velocity profiles near the coarser topography (Fig. 2.6a,b), but unlike in the laminar simulation, these fall well below the Ekman depth, calculated from (2.26) in the finest topographic resolution simulation ($\Delta z_{\text{topo}} = 0.01\delta_e$). These sub-$\Delta z$ differences extend to the hodograph (Fig. 2.6c), where the change in the spiral is much more pronounced compared to the laminar simulations. Instead of the exponential fit, the approximated $\delta_e^*$ is calculated from (2.26) for each simulation and normalized by the finest resolution $\delta_e^*$ (Fig. 2.6d). The best-fit line for the calculated Ekman depths has a slope of only $0.175$ and a CV of $1.25\%$, again indicating good agreement between the varying topography resolutions. The boundary layer can be calculated from the velocity as in the laminar simulations, but it can also be calculated using a cut-off based on the rate of dissipation of kinetic energy, $\epsilon$. Here $\epsilon$ is calculated directly by

$$\epsilon = \nu_e \frac{\partial u_i}{\partial x_j} \frac{\partial u_i}{\partial x_j}. \tag{2.31}$$

Using a threshold of $\epsilon = 5 \times 10^{-11}$ m$^2$s$^{-3}$, the dissipation, $\Delta_{\text{eps}}$, closely mirrors that of the velocity, $\Delta_u$, in Fig. 2.6d. The velocity boundary layer is around $2\delta_e$, while the dissipation rate boundary layer is measured at $3\delta_e$. The size of both these boundary layers increases with increas-

ing topographic coarseness, with best-fit slopes for $\Delta_{\text{eps}}$, $\Delta_{\text{u}}$ of $1.832$ and $2.18$ respectively. These are much larger trends than found in the laminar case, and could speak to the role topography plays in increasing the boundary-layer height.

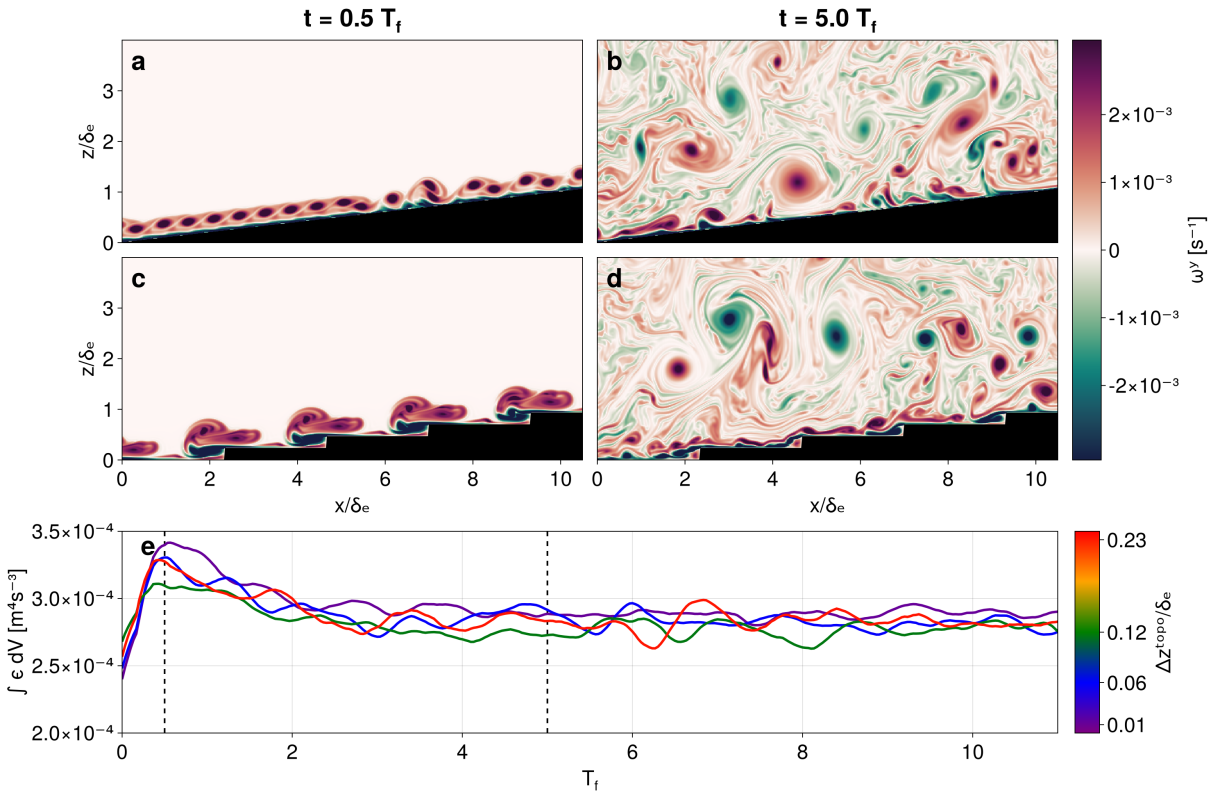



Figure 2.7: Along-slope vorticity, $\omega_y$ showing the onset of turbulence (a,c, $t = 0.5\,T_f$) compared to the fully-formed turbulent structures (b,d, $t = 5.0\,T_f$) in the non-stratified LES for the finest (a,b) and coarsest (c,d) topography. The volume integrated dissipation of kinetic energy rate, $\epsilon$, over all four non-stratified LES simulations is shown in (e). Colorbar is the calculated Ekman depth-normalized topographic coarseness.

While the across-slope averaged Ekman behavior in the turbulent simulations behaves similarly to that of the laminar, with little dependence on the topographic resolution, the onset of turbulence itself is very dependent on the topography. In 2D turbulence, energy can cascade upscale and vorticity is conserved in the inviscid case without stretching (Pope, 2008). As a result, 2D estimates of dissipation or turbulence intensity are not directly comparable to those in real

3D flows. However, in comparison to other 2D studies, they can still reveal the relative scales, instabilities, and evolving flow patterns that shape the onset of turbulence. During the first inertial period, eddy size from the along-slope vorticity, $\omega_y$, is correlated with the horizontal length of each step, while the number of eddies is dependent on the number of steps along the slope (Fig. 2.7, $0.5\,T_f$). Therefore, the finest resolution vorticity shows four times the number of eddies, but the size of each of those is smaller than the larger rollups seen in the coarsest resolution. This difference does not persist, though. Once 2D turbulence is fully developed (Fig. 2.7b,d, $t = 5.0\,T_f$), there is little difference in the distribution of vortices in the varying topographic coarseness. In 3D, vortex stretching and a forward energy cascade could enhance small-scale variability and dissipation, potentially altering the structure and longevity of these vortices (Pope, 2008). The volume integrated dissipation of kinetic energy (KE) rate (Fig. 2.7e) can be thought of as a global measure of turbulence activity. Each simulation line is smoothed by $0.3\,T_f$ for clarity. The temporal locations of the snapshots in (a-d) are marked by the horizontal dashed lines. While there is some initial variability between the simulations, the fully-developed turbulence has a similar integrated effect in all simulations, with the highest dissipation rate in the most resolved simulation. The integrated dissipation rate in Ekman flows is dependent on the along-slope stress (Umlauf et al., 2015). Therefore, the lack of variability in the dissipation rates could be due to the steady-state along-slope velocity profiles collapsing on top of each other at the boundary, despite disagreement aloft.

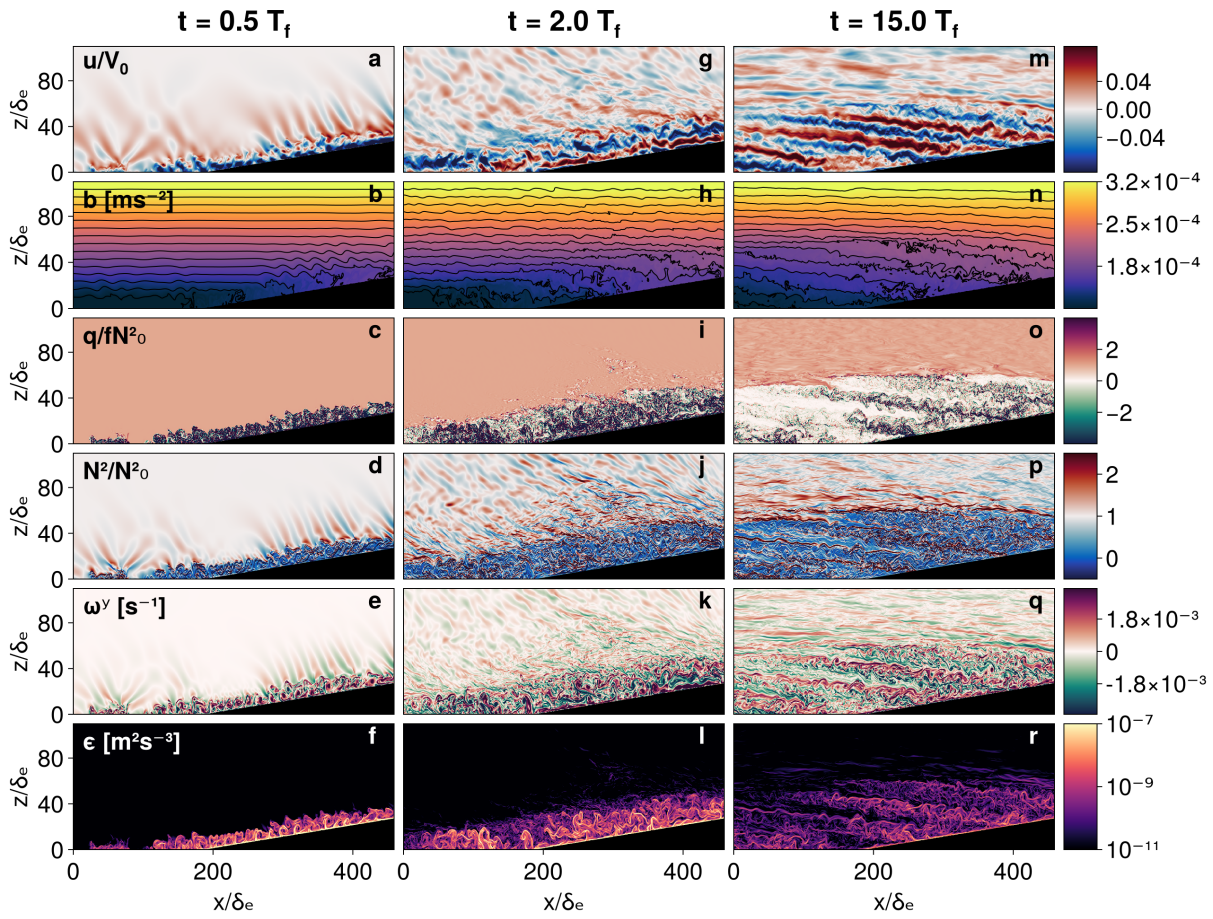



Figure 2.8: Snapshots from the $N_0^2 = 1.2 \times 10^{-6}$ s$^{-2}$ validation simulation with the finest topography resolution ($\Delta z_{\text{topo}}/\delta_e = 0.13$). Columns indicate 3 different times within the simulation, (a-f) $t = 0.5\,T_f$, (g-l) $2.0\,T_f$, and (m-r) $15.0\,T_f$. The fields shown are (a,g,m) the across-slope velocity normalized by the mean geostrophic background flow, (b,h,n) the total buoyancy, (c,i,o) the PV normalized by the initial planetary PV, (d,j,p) the stratification normalized by the initial stratification, (e,k,q) the along-slope vorticity, and (f,l,r) the dissipation of kinetic energy rate (in log scale).

### 2.6.3 Validation Case 3: Stratified, Turbulent Ekman

The three stratified simulation setups behave similarly, except for the height of the boundary layer and size of the subsequent SI cells, dependent on the changing stratification (Wenegrat and Thomas, 2020). Initially, the forced along-slope flow, $V_0$, generates a downslope Ekman flow in less than an inertial period (see Fig. 2.8a for the $N_0^2 = 1.2 \times 10^{-6}$ s$^{-2}$ case). Convection is already

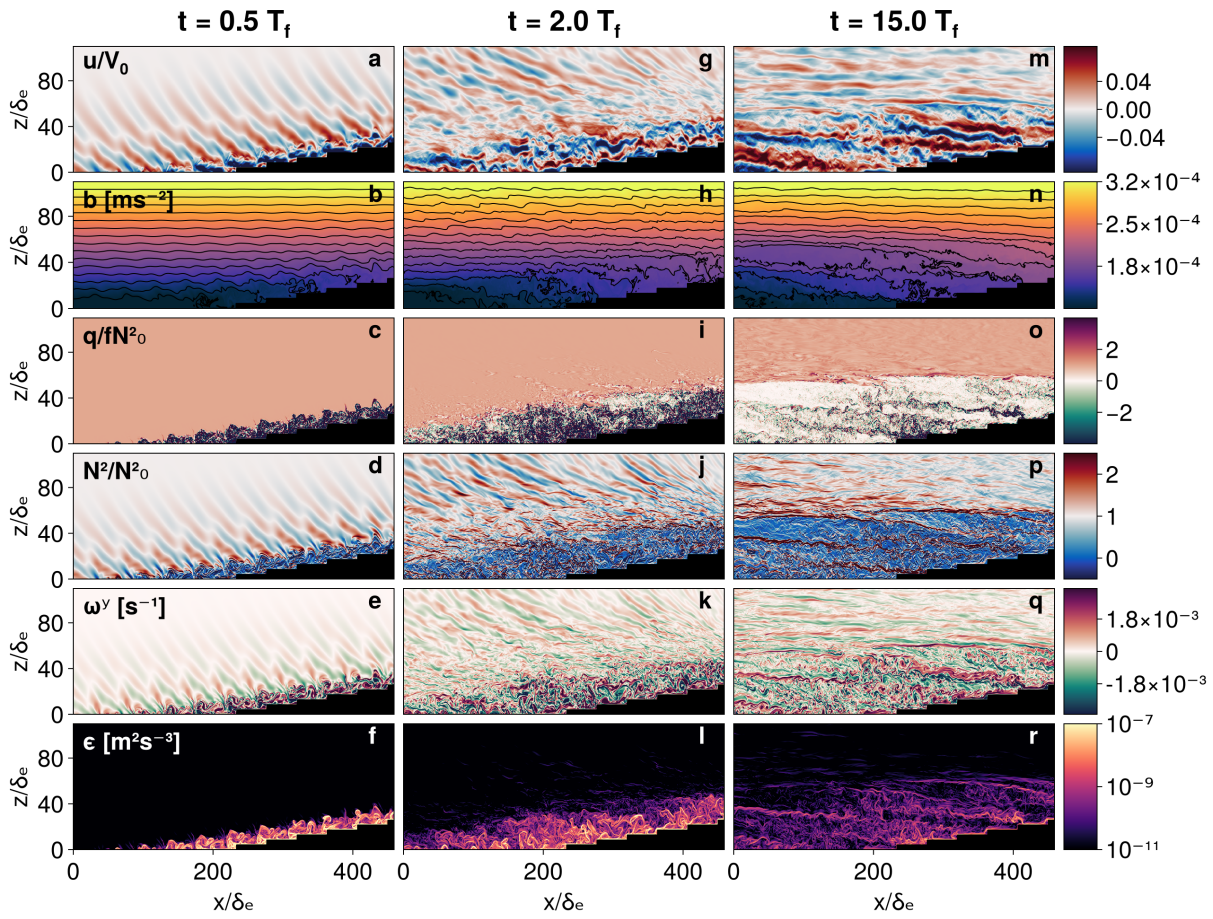



Figure 2.9: As in Fig. 2.8, except for the coarsest topography ($\Delta z_{\text{topo}}/\delta_e = 6.25$).

reducing the near-boundary stratification (Fig. 2.8d). Vertically propagating internal waves are also generated by the flow, seen in the banded structures above the BBL (Fig. 2.8a,d). The reduction of the stratification in the growing boundary layer also destroys PV (Fig. 2.8c), with a layer of the negative PV along the boundary (Benthuysen and Thomas, 2012). The mostly stable stratification, accompanied by $fq < 0$, means the BBL is unstable to SI (Haine and Marshall, 1998). Later in time, this gives rise to SI cells, seen in the banded structures in $u$ or the along-slope vorticity (Fig. 2.8m,q). The cells bring the boundary layer back to a state of marginal stability, noticeable in the $q \approx 0$ within the cell structures (Fig. 2.8o). This results in high

dissipation of KE rate and high stratification in convergent regions between neighboring cells (Fig. 2.8p,r). With increasing slope burger number (increasing stratification), the boundary layer becomes deeper, but the behavior and stages are similar (as in Wenegrat and Thomas, 2020).

The same snapshots can be seen for the coarsest topography in Fig. 2.9. The initially generated internal waves are much stronger and seem to be more dependent on the topographic length scales (Fig. 2.9a,d). This stronger organization persists in the next snapshot above the newly formed boundary layer (Fig. 2.9g,j), but has been taken over by the lateral flow by the last snapshot (Fig. 2.9m,p). Conversely, the cell structure in the coarsest topography seems to be more disorganized than the refined case, broken up by smaller-scale overturning features, mixing near the edge of the boundary layer, and possibly resulting in the larger intermediate buoyancy class, seen in Fig. 2.9n. While not explored here, this result suggests caution is warranted when considering topographic effects on watermass transformation at resolutions where submesoscale boundary-layer dynamics are coarsely resolved.

To understand the evolution of Ekman flow better, Fig. 2.10 shows the averages across-slope profile in time for the $N_0^2 = 3\times10^{-6}s^{-2}$ stratification. Comparing the finest ($\Delta_{\text{topo}} = 0.3\delta_e$) topography to the coarsest ($\Delta_{\text{topo}} = 6.3\delta_e$) shows similar growth of weak stratification, low PV, and high dissipation, indicating consistent boundary layer growth. The PV boundary-layer height is determined based on a threshold of $q = 0.99\, f N_0^2$, marked by the black contours in Fig. 2.10. This calculated value is similar to the boundary-layer height defined using a threshold in $\epsilon$ (gray line, Fig. 2.10). These boundary layer thresholds show only minimal increases in the coarser step size boundary layer height later in the given simulation ($t > 15T_f$, Fig. 2.10). Considering all variations in stratification and topographic coarseness, the boundary-layer height defined by the PV threshold shows good agreement (Fig. 2.11b). The smallest stratification (and smallest $S_0^2$)

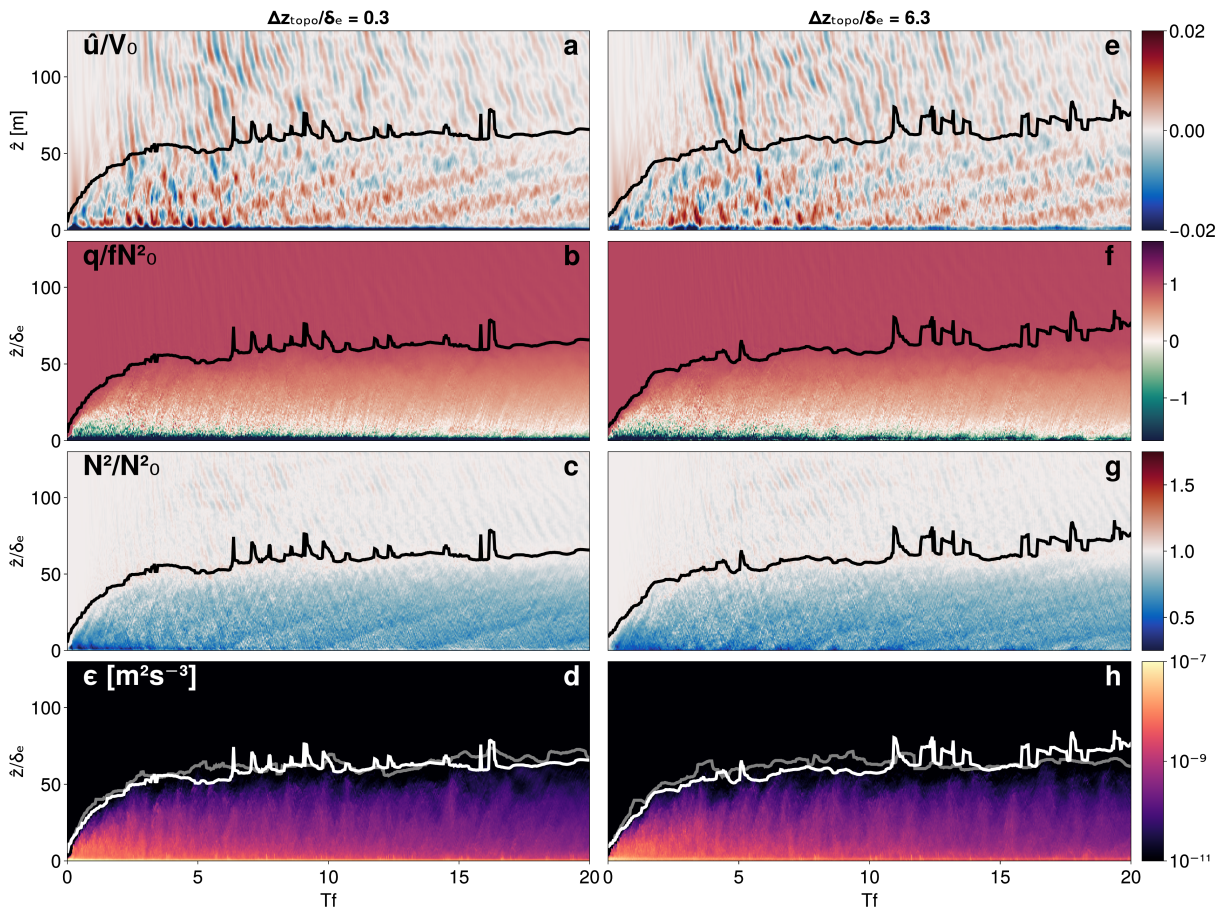



Figure 2.10: Across slope averaged profiles in time, for the $N_0^2 = 3 \times 10^{-6}$ s$^{-2}$ simulation, of rotated across-slope velocity $\hat{u}$, the normalized PV, $q/fN_0^2$, the normalized stratification, $N^2/N_0^2$, and the dissipation of kinetic energy rate, $\epsilon$ (in log scale). Plots are shown for the finest (col 1, $\Delta z_{\text{topo}}/\delta_e = 0.3$)and coarsest (col 2, $\Delta z_{\text{topo}}/\delta_e = 0.6.3$) topographic resolution. The thick black (white in $\epsilon$) line represents the height of the PV layer, while the gray line in $\epsilon$ is the boundary-layer height defined using the $\epsilon$. Both are smoothed over $0.3\,T_f$.

shows the best agreement with a slope of only $m = 0.052$ and a CV of $1.04\%$. The other two also have small, if slightly increasing trends with slopes of $0.338$. The trends in the boundary-layer height calculated using the dissipation of KE rate (Fig. 2.11a) show stronger variations across all simulations, and no clear trends, with some positive and some negative correlations. The smallest $S_0^2$ value also does the best at maintaining a constant boundary-layer height, with a slope of only $0.63$ and a CV of $0.97\%$, indicating good agreement over all topographic resolutions.

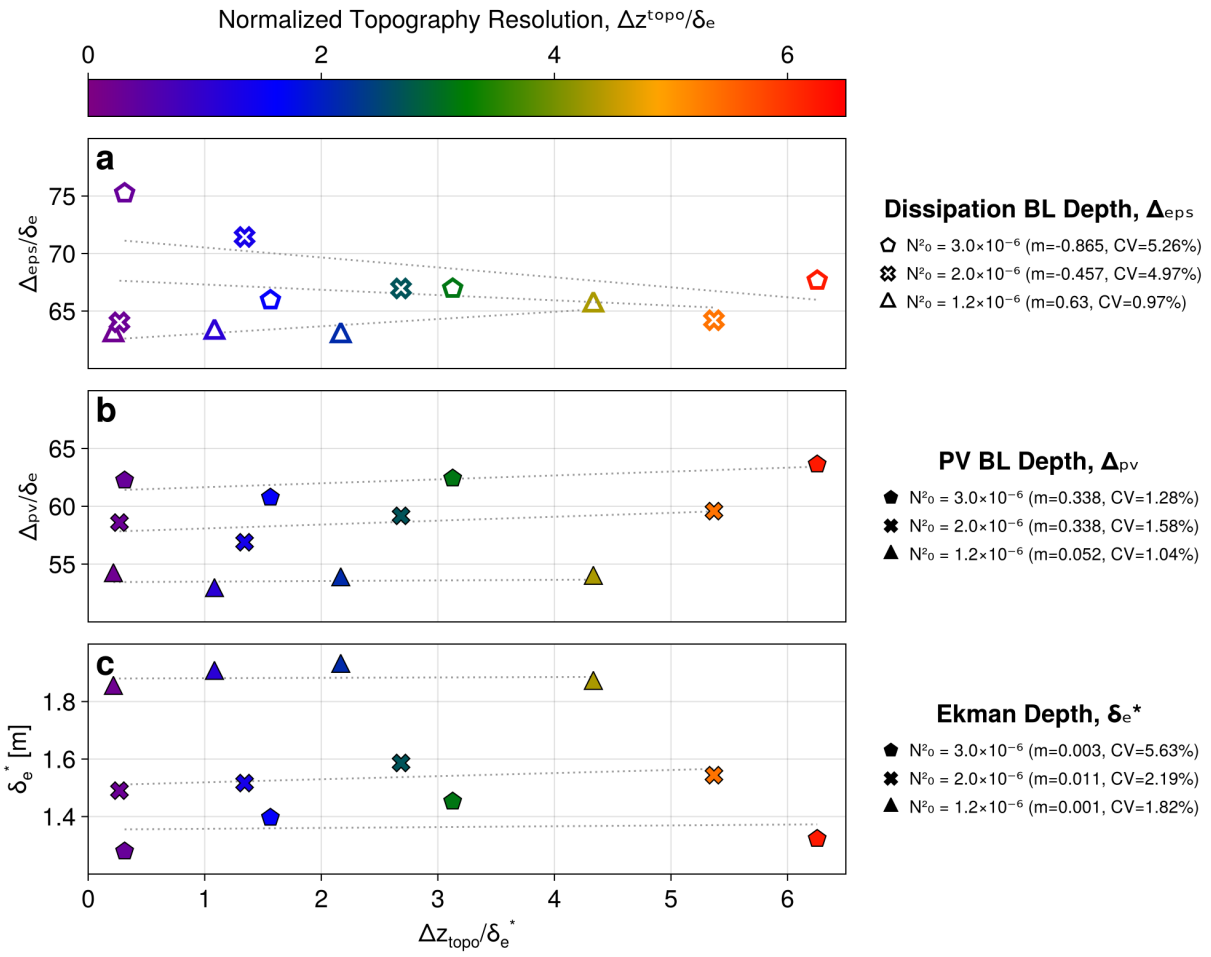



Figure 2.11: Length scale comparisons from the stratified validation simulations. (a) is the comparison of boundary-layer heights calculated using PV or the dissipation of KE rate, each normalized by each relevant Ekman depth, calculated using (2.26) on the finest topographic resolution. (b) shows the calculated Ekman depth for each simulation (not normalized).

The variations in $\Delta_{\text{eps}}$ with increasing stratification could be related to differences in the amount of turbulence for different step sizes, a numerical problem with the chosen threshold, or the limitations of turbulence in a 2D domain.

The agreement in boundary-layer depth suggests that the frictional definition of Ekman depth (2.27) and the Ekman transport will also be consistent across topographic coarseness, with implications for the consistency of the Ekman buoyancy flux (EBF) (Wenegrat and Thomas,

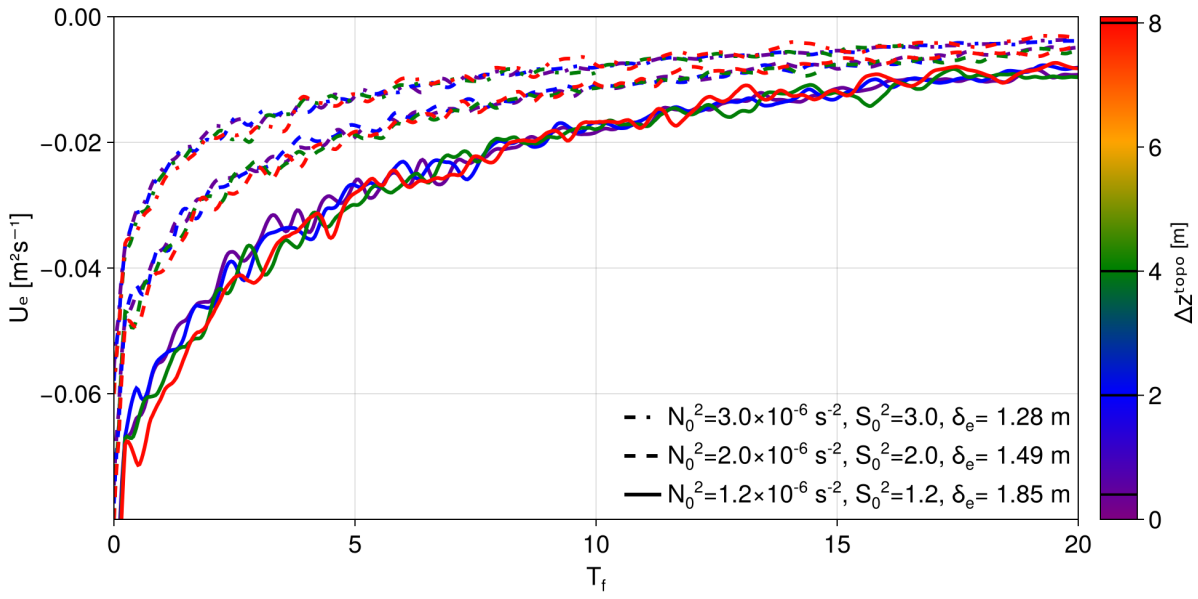



Figure 2.12: Ekman transport in time calculated from the bottom stress formulation in (2.28) for all three stratification values (line style). Note that here the line colors indicate the topographic resolution and are not normalized by the relevant Ekman depth to differentiate more easily between line colors in each set. Results are smoothed using a rolling average of $0.2\,T_f$.

2020). The Ekman depths are very small, which correlates with the change in $f$ in these simulations and the addition of stratification. Despite not resolving the Ekman depth in almost all of the topographic coarseness levels tested, the calculation of $\delta_e^*$ remains steady. Fig. 2.11c shows all values (not normalized, for easier visualization), with slopes all less than $0.011$. The variation is greatest for the largest tested $S_0^2$ with a CV of 5.63%, but the total trend remains flat. The calculation of the Ekman transport using the along-slope stress (2.28) is shown for all simulations in Fig. 2.12. There was less of a dependence on the ratio of the grid spacing with the calculated Ekman depth and more of one related to the true step size, so unlike the previous plots, lines have been colored according to the true topographic coarseness ($0.2 - 8.0$ m). Once again, results show good agreement as the topography is increasingly coarsened. The largest differences in transport occur in the first $5\,T_f$, where the coarsest topography underestimates the transport compared to

the finer cases. This is most prominent in the simulations run with the smallest slope Burger number, $S_0^2 = 1.2$. The coarsest case also shows the most variation later in time, though these differences are minimal.

The height of the boundary layer and the general characteristics of stratified Ekman flow remain essentially unchanged, even when the Ekman depth is heavily under-resolved. Because the bottom stress remains consistent across the coarsened topographic resolutions, the associated Ekman transports are likewise insensitive to grid refinement (Fig. 2.12). This robustness indicates that the grid-fitted boundary does not distort the magnitude or spatial structure of bottom drag dissipation, which can be highly sensitive to stress variability (Umlauf et al., 2015), nor does it introduce spurious modifications to the Ekman buoyancy flux, which depends directly on the Ekman transport and its interaction with horizontal buoyancy gradients (Wenegrat and Thomas, 2020). Preserving bottom-stress integrity despite large changes in topographic step size, therefore, suggests that the IBM implementation is unlikely to compromise either the dissipative pathways or the buoyancy-modifying pathways that shape energy and tracer budgets near the boundary.

## 2.7 Assessment and Outlook

While other geophysical models have implemented various forms of IBM, grid-fitted IBM remains relatively understudied and under-validated for small-scale oceanic flows (Nasr-Azadani and Meiburg, 2011; Arthur et al., 2020; Lundquist et al., 2012; Maronga et al., 2015). Oceananigans has previously validated the grid-fitted IBM implementation for numerical accuracy, conservation, and classical benchmark problems, such as flow past a cylinder (Wagner et al., 2025b).

The goal of this work was to assess the performance of the grid-fitted IB method in a geophysical context, using the well-studied Ekman flows along sloping topography for validation. Bottom Ekman dynamics are highly sensitive to frictional effects along the boundary and have received significant attention as a mechanism for water-mass transformation contributing to the closure of the global overturning circulation (Wenegrat and Thomas, 2020; Chor and Wenegrat, 2025; Jagannathan et al., 2021, 2023; Srinivasan et al., 2019; Schubert et al., 2025). By demonstrating accurate representation of these flows, this study provides confidence in applying the grid-fitted IBM to more complex geophysical scenarios where topography and boundary effects play a critical role.

Laminar, turbulent, stratified, and unstratified simulations were used to test the sensitivity of boundary-layer characteristics to topographic coarseness. The convergence of key Ekman-layer features across topographic resolutions demonstrates that the grid-fitted IBM is robust, even when the grid approaches the limits of LES resolution. Some small-scale circulation develops along the step transitions, where vertical faces modify cross-slope and slope-normal flow patterns (Fig. 2.4), and profiles deviate below the step-scale resolution (Fig. 2.5). However, these discrepancies at sub-step scales are not as dynamically significant as changes that impact the flow above the topographic steps, as typical simulations align vertical resolution with the step height, rendering such effects negligible. The dependence of small slope-normal velocities on the topographic step size influenced the early onset of turbulence (Fig. 2.7, $t = 0.5, T_f$), but once turbulence was fully developed, this dependence diminished (Fig. 2.7, $t = 5.0, T_f$). Even for the coarsest topography, the simulations accurately captured the bulk characteristics of Ekman flow, including the e-folding length scale and boundary-layer depths (Figs. 2.5, 2.6, 2.11).

In the stratified cases, the downslope Ekman transport induced cross-isopycnal convection,

eroding PV and generating SI cells. The PV boundary-layer depth, which scales with the bottom stress (Wenegrat and Thomas, 2020), remained consistent across topographic resolutions, with coefficients of variation below $2\%$ for all three stratifications tested (Fig. 2.11b). The close agreement in boundary-layer thickness is reflected in the Ekman transport, where the grid-fitted boundary captures consistent values in time even when the Ekman depth is poorly resolved. Therefore, despite large topographic step sizes, the stratified boundary layer adjusts to the along-slope flow in a nearly identical way at all resolutions. This consistency in bottom stress indicates that the grid-fitted boundary can correctly capture energetics and mixing efficiency as calculated by the Ekman buoyancy flux or bottom drag dissipation (Wenegrat and Thomas, 2020; Umlauf et al., 2015).

The grid-fitted IBM in Oceananigans modifies the governing equations by directly replacing fluxes along the boundary with the boundary condition-prescribed immersed fluxes. This approach allows accurate representation of sloping boundaries while maintaining numerical conservation. The present validation suggests that increased roughness from the stepwise representation or small vertical velocities introduced at step junctions does not substantially alter simulated BBL dynamics for downslope Ekman flows. These results should still be interpreted with caution, as the downslope Ekman configuration primarily steers the flow over the stepped geometry rather than directly into the vertical faces, and therefore does not capture cases where boundary-normal currents interact more strongly with the grid-fitted topography. In addition, the limited domain size constrains the development of fully three-dimensional turbulence, which may suppress some mixing pathways or alter the details of the boundary-layer adjustment.

Extending this validation by varying slope angle could help to distinguish whether errors arise primarily from step transitions or from the flat regions between them. Upslope Ekman

flows (Brink and Lentz, 2010) also represent a natural extension, where the vertical faces may more directly impede cross-slope motion when the boundary-layer depth remains small relative to topographic roughness (Brink and Lentz, 2010). Finally, three-dimensional simulations and validation problems where cross-slope variability is important will be essential for assessing how these findings generalize to more complex turbulent and mixing processes that cannot be reduced to one-dimensional dynamics. Together, these results demonstrated that the grid-fitted IBM provides a numerically efficient and physically consistent framework for representing sloping boundaries in geophysical LES, laying the foundation for future studies of oceanic boundary layers over realistic topography.

# Chapter 3: Breaking internal waves on sloping topography: connecting parcel displacements to overturn size, interior-boundary exchanges, and mixing[1]

## 3.1 Introduction

Internal waves breaking on topography are significant to many ocean processes. Internal tides impinging on both critical and off-critical topography can result in bottom-enhanced turbulent mixing, and diapycnal upwelling necessary for the closure of the abyssal circulation (Eriksen, 1985; Polzin et al., 1997; Slinn and Riley, 1998; Kunze et al., 2012; Cyr and van Haren, 2016b; Chalamalla et al., 2013; van Haren and Gostiaux, 2012b). Recent theoretical work and observations suggest upwelling near sloping bottom boundaries may be limited to turbulent Bottom Boundary Layers (BBLs) where the mixing profile allows for convergent turbulent buoyancy fluxes, (Ferrari et al., 2016; Mashayek et al., 2017; Wynne-Cattanach et al., 2024). Exchanges

[1]An edited version of this chapter was published as: Whitley, V and Wenegrat, J.O., 2025: Breaking internal waves on sloping topography: connecting parcel displacements to overturn size, interior-boundary exchanges, and mixing. *J. Phys. Ocean.*

©Copyright 2025 American Meteorological Society (AMS). For permission to reuse any portion of this Work, please contact permissions@ametsoc.org. Any use of material in this Work that is determined to be "fair use" under Section 107 of the U.S. Copyright Act (17 U.S. Code § 107) or that satisfies the conditions specified in Section 108 of the U.S. Copyright Act (17 USC § 108) does not require the AMS's permission. Republication, systematic reproduction, posting in electronic form, such as on a website or in a searchable database, or other uses of this material, except as exempted by the above statement, requires written permission or a license from the AMS. All AMS journals and monograph publications are registered with the Copyright Clearance Center (https://www.copyright.com). Additional details are provided in the AMS Copyright Policy statement, available on the AMS website (https://www.ametsoc.org/PUBSCopyrightPolicy).

between the stratified interior and the well-mixed BBL associated with breaking internal waves could be a pathway for the restratification of these boundary waters, necessary to maintain an efficient diapycnal process (Armi, 1978; van Haren, 2023). These breaking events and interior exchanges also allow for the transport and recycling of carbon, oxygen, and nutrients crucial for the ecosystem (Cheriton et al., 2014; Churchill et al., 1988; Bonnin et al., 2006; Cyr and van Haren, 2016b; McPhee-Shaw et al., 2021a). The reflection and possible breaking of internal waves could result in bottom velocities strong enough to resuspend particles on the sea floor in nepheloid layers (Cacchione and Drake, 1986), often observed in lakes and off continental shelves (e.g., McPhee-Shaw et al., 2004; McPhee-Shaw, 2006; Bonnin et al., 2006; Edge et al., 2021). These nepheloid layers are also observed as lateral intrusions into the interior (Gardner et al., 2017; Thorpe and White, 1988), similar to internal wave laboratory experiments and numerical models showing layers of dye ejected from the slope (Nokes and Ivey, 1989; Winters, 2015).

Several parameters have been used to characterize internal wave formation and nearby breaking in the presence of both oscillating and steady barotropic forcing, including the nonlinearity of the resulting wave behavior and the flow's ability to overcome obstacles (Winters and Armi, 2013; Chalamalla et al., 2013; Sarkar and Scotti, 2017; Legg and Klymak, 2008; Drazin, 1961). When a steady flow is blocked by topography, the length scale given by the steady velocity, $U$, over the buoyancy frequency, $N$, represents the thickness of the layer that can continue past the obstacle (Winters and Armi, 2013). This results in a new "effective height," $h_{eff} = U/N$, of the topography and sets the vertical scale for the resulting waves (Winters and Armi, 2013; Legg and Klymak, 2008). This ratio is included in the Scorer number, as well, an atmospheric parameter characterizing lee waves (Scorer, 1949). The effective height leads to the characterization

of the topographic Froude number, $Fr = U/Nh$, where $h$ is the obstacle's height. Nonlinear hydraulic effects can be found in simulations of small $Fr$, (Sarkar and Scotti, 2017; Chalamalla et al., 2013; van Haren, 2023), where the height of the obstacle is much larger than the effective height. Here we show that a similar effective height parameter is useful for characterizing aspects of wave breaking along topography.

While the generation and nearby-breaking of internal waves over topography have been extensively modeled (Winters and Armi, 2013; Sarkar and Scotti, 2017), there is also clear evidence of turbulence resulting from remotely forced internal waves reaching sloping boundaries (Aucan et al., 2006; van Haren et al., 2015; Jones et al., 2020). This turbulence can result from the formation of critical layers when the slope of the incident wave is close to that of the topography (Nokes and Ivey, 1989; Slinn and Riley, 1998; Lamb, 2014; Gemmrich and Klymak, 2015), but can also be found when the slope is not critical. In particular, the oscillating flow of internal waves up and down the slope can result in intermittent overturns and breaking within the phases of the wave period, sometimes described as "swashing" motions (Cyr and van Haren, 2016b). The overturns tend to occur at the rapid transition between down and upslope flow, as well as during the downslope phase where intensified near-slope velocities result in shear along the slope (Cyr and van Haren, 2016b; Aucan et al., 2006; Winters, 2015; van Haren and Gostiaux, 2012b; Gayen and Sarkar, 2011). These types of overturning events have been observed along the continental slope (van Haren, 2006) and in the deep ocean (Cyr and van Haren, 2016b; Wynne-Cattanach et al., 2024).

In a simulation with a low-mode internal tide impinging on a supercritical slope in rotating, stratified fluid, Winters (2015) notes a visual similarity between the length scales of the expulsion events from the boundary layer to the interior and a vertical length scale defined similarly to $h_{eff}$

except with the velocity scale set by the wave velocities (rather than a steady background flow)—a quantity we term here as the *effective wave height*. A similar dependence on the effective wave height was also noted to scale the size of turbulent patches in Large Eddy Simulations (LES) of internal tides interacting with the steep western ridge of the Luzon Strait (Jalali et al., 2017). Motivated by these observations and results, this paper focuses on a set of highly-resolved, three-dimensional simulations of internal waves impinging on sloping boundaries, where wave velocity, stratification, frequency, and criticality are varied, spanning a range of values relevant to the ocean. There is a strong dependence on the vertical effective wave height throughout the breaking process, resulting in subsequent dissipation and boundary-interior exchange scaled by the effective wave height near the slope.

The manuscript is organized as follows. In section 3.2 we introduce the high-resolution model used to explore the breaking events as well as a description of the parameter space surveyed in this study. In section 3.3 we describe a characteristic breaking event and introduce the governing scaling found throughout the mixing process. This is followed by an explanation of the mechanism behind the resulting interior and boundary exchange with connections to the previously discussed vertical scaling. Water-mass transformation and diapycnal mixing involved are then analyzed for a representative simulation. Conclusions, and several avenues for future study, are reviewed in section 3.4.

## 3.2 Numerical Model Set Up

To explore the interaction between the BBL and the interior in the presence of breaking internal waves, we used high-resolution Large Eddy Simulations (LES) of internal waves im-

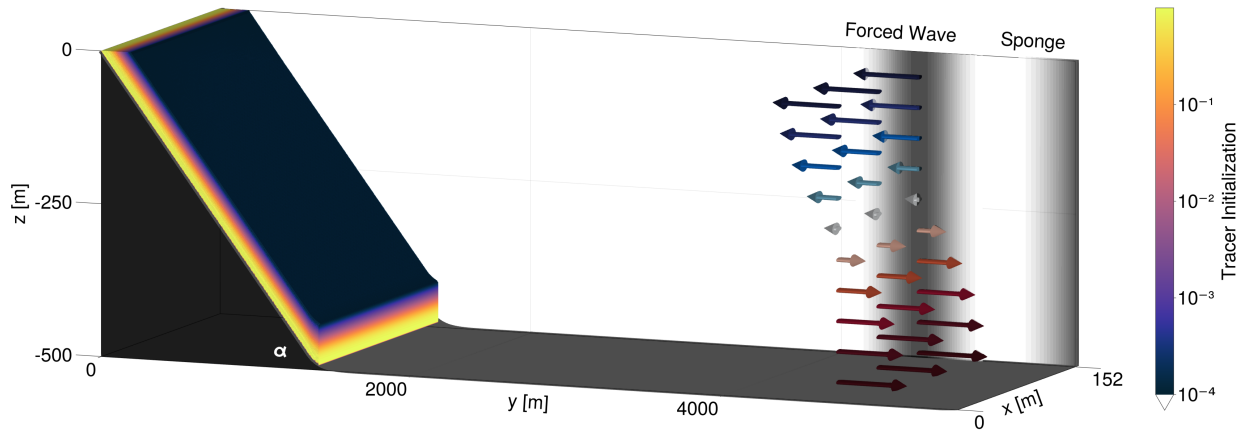



Figure 3.1: 3D LES domain set up. Planar topography with slope $\tan\alpha$ shown in black. The location of the forced internal wave is indicated with arrows centered at $y = 4500$, and the gray Gaussian shading behind the arrows. The sponge regions near the right boundary are also marked out with gray shading, representing the amplitude of damping. Contours of the initial hyperbolic tangent condition of the concentration of the tracer are also shown. The tracer is uniformly initialized in the across-slope direction, similar to the topography.

pinging on a planar slope. The incompressible Navier-Stokes equations under the Boussinesq approximation were solved using a non-hydrostatic model in the julia package, Oceananigans (Ramadhan et al., 2020). Oceananigans uses a finite volume method on a staggered, structured grid based on that of MITgcm (Ramadhan et al., 2020; Marshall et al., 1997). A fifth-order weighted essentially non-oscillatory (WENO) scheme advects velocities and tracers, with a third-order Runge–Kutta time-stepping method (Ramadhan et al., 2020; Silvestri et al., 2024). A Fast Fourier Transform solves Poisson's equation for the non-hydrostatic pressure (Ramadhan et al., 2020). We employed the Smagorinsky-Lilly subgrid-scale model for the LES turbulence closure, with a turbulent Prandtl number, $Pr_t = 1$. With an average eddy viscosity of O($10^{-3}$ m$^2$s$^{-1}$) and Reynolds number of O($10^5$), background molecular diffusivity and viscosity were omitted from the model. While the implemented LES closure is explicit, the use of the WENO advection scheme could add some numerical dissipation to the model (Silvestri et al., 2024).

The domain, shown in Fig. 3.1, is three-dimensional, with size $(L_x, L_y, L_z) = (152, 6500, 500)$ m, with periodicity in the along-isobath (x) direction and uniform grid spacing of $\Delta y = \Delta x = 4$ m and $\Delta z = 2$ m. To test the grid resolution dependency, vertical grid spacing was varied from $\Delta z = 1.5$ m to 6 m, and the horizontal spacing from $\Delta x = \Delta y = 3$ m to 8 m, for two representative simulations (see Appendix B for details). The chosen grid spacing, $\Delta y = \Delta x = 4$ m and $\Delta z = 2$ m, was found to resolve the Ozmidov length, defined as,

$$L_O = \left(\frac{\bar{\epsilon}}{N_0^3}\right)^{1/2}, \tag{3.1}$$

where $\bar{\epsilon}$ is the average dissipation rate of kinetic energy over turbulent regions, ($\epsilon > 10^{-10}$ m$^2$s$^{-3}$) (Khani, 2018; Dillon, 1982). Other results discussed in this paper, such as average intrusion thicknesses and the buoyancy flux analysis were also found to be quantitatively insensitive to the changes in resolution, as long as the prevailing length scales were resolved with several grid points. The behavior of the simulations with the largest expected characteristic length scales could be impacted by the limitations of the vertical domain. To check this, three simulations were run with an increased vertical height of $L_z = 650$ m. These simulations are marked by $(\cdot)^+$ in Table 3.1 and denoted by $(\cdot)^B$ in the corresponding results.

Boundary conditions in the bottom normal direction were no flux on buoyancy and tracers and quadratic drag on momentum. Topography was included in the simulation using a grid-fitted immersed boundary method with the quadratic drag boundary conditions set on each boundary-adjacent cell face. The idealized domain was initialized with a uniform stratification, $N_0^2$, and constant Coriolis frequency, $f$, with the ratio, $N_0/f = 10.7$, kept constant over all simulations. The topographic slope was given by $\tan\alpha$. A full list of parameters for the main set of simulations

Table 3.1: Simulation Parameters for Main Reference Set

| | Vary $V_0$ | | | Vary $N_0$ | | |
|---|---|---|---|---|---|---|
| $h_w$ [m] | $V_0$ [ms$^{-1}$] | $N_0^2$ [s$^{-2}$] | $L_z$ [m] | $V_0$ [ms$^{-1}$] | $N_0^2$ [s$^{-2}$] | $L_z$ [m] |
| 14.29 | 0.05 | $1.23\times10^{-5}$ | 500 | 0.25 | $3.06\times10^{-4}$ | 500 |
| 28.57 | 0.10 | $1.23\times10^{-5}$ | 500 | 0.25 | $7.66\times10^{-5}$ | 500 |
| 42.86 | 0.15 | $1.23\times10^{-5}$ | 500 | 0.25 | $3.40\times10^{-5}$ | 500 |
| 57.14* | 0.20 | $1.23\times10^{-5}$ | 500 | 0.25 | $1.91\times10^{-5}$ | 500 |
| 71.43 | 0.25 | $1.23\times10^{-5}$ | 500 | 0.25 | $1.23\times10^{-5}$ | 500 |
| 85.71 | 0.30 | $1.23\times10^{-5}$ | 500 | 0.25 | $8.51\times10^{-6}$ | 500 |
| 100.00** | 0.35 | $1.23\times10^{-5}$ | 500 | 0.25 | $6.25\times10^{-6}$ | 500 |
| 114.29 | 0.40 | $1.23\times10^{-5}$ | 500 | 0.25 | $4.79\times10^{-6}$ | 500 |
| 128.57 | 0.45 | $1.23\times10^{-5}$ | 500$^+$ | 0.25 | $3.78\times10^{-6}$ | 500 |
| 142.86 | 0.50 | $1.23\times10^{-5}$ | 500$^+$ | 0.25 | $3.06\times10^{-6}$ | 500 |
| 157.14 | 0.55 | $1.23\times10^{-5}$ | 500$^+$ | 0.25 | $2.53\times10^{-6}$ | 500 |

*Similar to the values used in Winters (2015)
**Similar to the values observed in van Haren (2006)
$^+$Simulations also run with $L_z = 650$ m for Vary $V_0^B$ case

can be found in Tables 3.1 and 3.2.

The exchange of fluid between the lower boundary layer and the interior was quantified using a passive, neutrally buoyant, tracer initialized along the entire slope boundary using a hyperbolic tangent function extending 20 m above the slope. This initialization can also be seen in Fig. 3.1. The change in integrated tracer volume in the model compared to the initial volume was on the order of $10^{-10}$ for all simulations, indicating the immersed boundary method used in Oceananigans conserved the dye for this simulation setup sufficiently for the purposes of the following analyses.

In each simulation, mode-1 oscillations were continuously forced in the $v$ momentum equation. The forcing region was determined by a Gaussian centered at $y = 4500$ m, more than 3000 m from the closest point of the slope, as seen in the arrows and gray contours in Fig. 3.1. The

Table 3.2: Constant Simulation Parameters for Main Reference Set

| Parameter | Value | Comment |
|---|---|---|
| $N_0/f$ | 10.7 | Chosen for comparison to Winters (2015) |
| $\sigma/f$ | 2.2 | $\sigma/f > 2$, PSI possible |
| $h$ [m] | 500 | Height of topography |
| $\ell[m]$ | 1406 | Length of topography |
| $\tan\alpha$ | 0.356 | Topographic slope (d$h$/d$\ell$) |
| $\gamma$ | 1.9 | Slope is supercritical ($\tan\alpha/\tan\theta$) |

forcing was derived by taking the $v$ component from linear internal wave theory as

$$v(x, y, z, t) = V_0 \cos(ly + mz - \sigma t), \tag{3.2}$$

with maximum velocity, $V_0$, and frequency, $\sigma$, specified in each simulation. The horizontal wave number, $l$, was determined from the dispersion relation for linear internal waves (Gill, 1982). Simulations were run with mode-1 vertical wave number, $m = \pi/L_z$, representative of an internal tide. Using only the $v$ component was found to be sufficient to set up an oscillating internal wave, with resulting velocities close to the prescribed $V_0$. Typically, tidal velocities would be a few centimeters per second, although this was varied here from $0.05$ ms$^{-1}$ to $0.55$ ms$^{-1}$ to span a wide range of the parameter space (Table 3.1). The wave period, $T_\sigma = 2\pi/\sigma$, from the forced wave, will be used to describe some simulation results. All simulations were run for at least 11 wave periods, with a variable time step between $10^{-4}$ s and 10 s, as determined by a CFL of $0.5$ within the simulation. Diagnostics were calculated every $600$ s, or such that there are at least $15$ snapshots every wave period. A sponge region was added to all fields along the right boundary of the domain to prevent spurious reflections (sponge region marked with gray contours in Fig.

Table 3.3: Simulation Parameters for Assessing Sensitivity to Wave Frequency, $\sigma$, and Criticality, $\gamma$

| Vary $\gamma$ | | | | | | |
|---|---|---|---|---|---|---|
| $h_w$ (m) | $V_0$ (ms$^{-1}$) | $N_0^2$ (s$^{-2}$ | $N/f$ | $\sigma/f$ | $\gamma$ ($\tan\alpha/\tan\theta$) | $\tan\alpha$ ($dh/d\ell$) |
| 42.86 | 0.15 | $1.23\times10^{-5}$ | 10.7 | 2.8 | 1.4 | 0.356 |
| 42.86 | 0.15 | $1.23\times10^{-5}$ | 10.7 | 5.5 | 0.6 | 0.356 |
| 128.57 | 0.45 | $1.23\times10^{-5}$ | 10.7 | 2.8 | 1.4 | 0.356 |
| 128.57 | 0.45 | $1.23\times10^{-5}$ | 10.7 | 5.5 | 0.6 | 0.356 |

3.1).

While varying the buoyancy frequency and wave velocity, some relationships were held constant (Table 3.2), using values from Winters (2015). The slope of internal wave propagation is given by,

$$\tan\theta = \sqrt{\frac{\sigma^2 - f^2}{N^2 - \sigma^2}}. \tag{3.3}$$

For the main set of simulations, a criticality of $\gamma = \tan\alpha/\tan\theta = 1.9$ was used. While the slope used in these simulations was physically steep due to computational limitations, the criticality is within the range of observed values (see for instance van Haren, 2006; Wynne-Cattanach et al., 2024), and results were tested and found to be qualitatively insensitive to the chosen ratio of $\tan\alpha/\tan\theta$ for another supercritical and also a subcritical value. The ratio $\sigma/f = 2.2$ was held constant for the simulations in the main parameter space of Table 3.1, while the additional cases of subcritical and supercritical wave reflection were tested by varying the ratio $\sigma/f$, but holding $N/f$ constant, as shown in Table 3.3. All parameter values varying $\sigma$ and $\gamma$ still followed the relationships found for the supercritical results with $\sigma/f = 2.2$.

## 3.3 Results

### 3.3.1 Physical mechanism and scaling of breaking internal waves

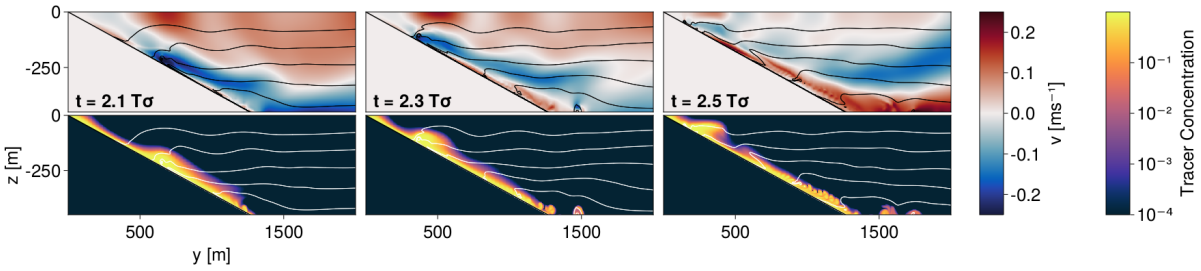



Figure 3.2: Snapshots of velocity (v, top row) and dye concentration (bottom row) during the second wave period. The right column, $t = 2.5\ T_\sigma$, shows the initial small overturns found along the slope during this quasi-spin-up period. Isopycnals are marked as contour lines in all images. Animations can be found of these fields in the supporting information.

Snapshots from the first breaking event above a supercritical slope ($\tan\alpha/\tan\theta = 1.9$), with velocity, $V_0 = 0.25$ ms$^{-1}$, and stratification, $N_0^2 = 1.23 \times 10^{-5}$ s$^{-2}$ are shown in Fig. 3.2. The simulation was started from rest, except for the incoming forced wave. Initially, the internal wave advected isopycnals along the slope. During the second wave period ($t = 2\ T_\sigma$) a bore of denser water was formed and advected up the slope, shown in Fig. 3.2 ($t = 2.1T_\sigma$). Halfway through this upslope phase, the water closest to the slope in the lower 20 meters began to advect back down the slope (Fig. 3.2, $t = 2.3T_\sigma$). Convective instability near the boundary during the wave phase transition resulted in small overturns, with downslope flow carrying lighter water near the boundary while the upslope phase still carried denser water aloft, as seen in Fig. 3.2 ($t = 2.5T_\sigma$). These initial overturns were similar to those described in low amplitude velocity cases (Drake et al., 2020; Kaiser et al., 2022), but this phasing was here only characteristic of those initial few wave periods and is not the focus of this work.

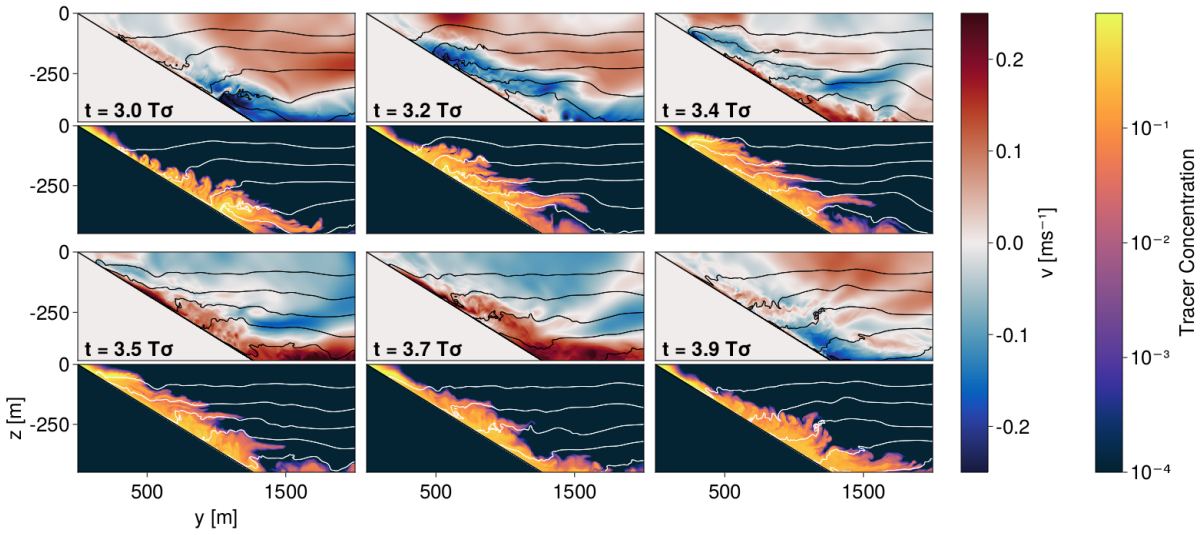



Figure 3.3: Snapshots of velocity (v, first rows) and dye concentration (secondary rows) during the third wave period. The upper left plots, $t = 3.0T_\sigma$, show the initial large upslope bore (blue). Isopycnals are marked as contour lines in all images. Animations can be found of these fields in the supporting information.

Following these initial small breaking events in the same simulation, the characteristic overturning process depicted in Fig. 3.3 is representative of the evolution seen across the surveyed parameter space. At the beginning of the upslope phase, a much larger bore of dense water immediately overturned and broke along the slope around 300 m depth (Fig. 3.3, $t = 3.0 - 3.2T_\sigma$). This was followed by smaller overturns at the transition to downslope flow ($t = 3.4T_\sigma$), similar to those discussed in the earliest wave periods. However, these were not as significant as the second overturn event which occurred when downslope flow was at a maximum, bringing lighter water under heavier water, as seen at $t = 3.5 - 3.7\,T_\sigma$ in Fig. 3.3. Similar downslope overturns observed in the Kaena Ridge, and in LES have been attributed to shear instability (Aucan et al., 2006; Gayen and Sarkar, 2011). The bore leading a sharp transition to upslope flow, and the intensified flow near the boundary during the downslope phase, often accompanied by an increase in turbulence and mixing, have been found in both numerical simulations and observa-

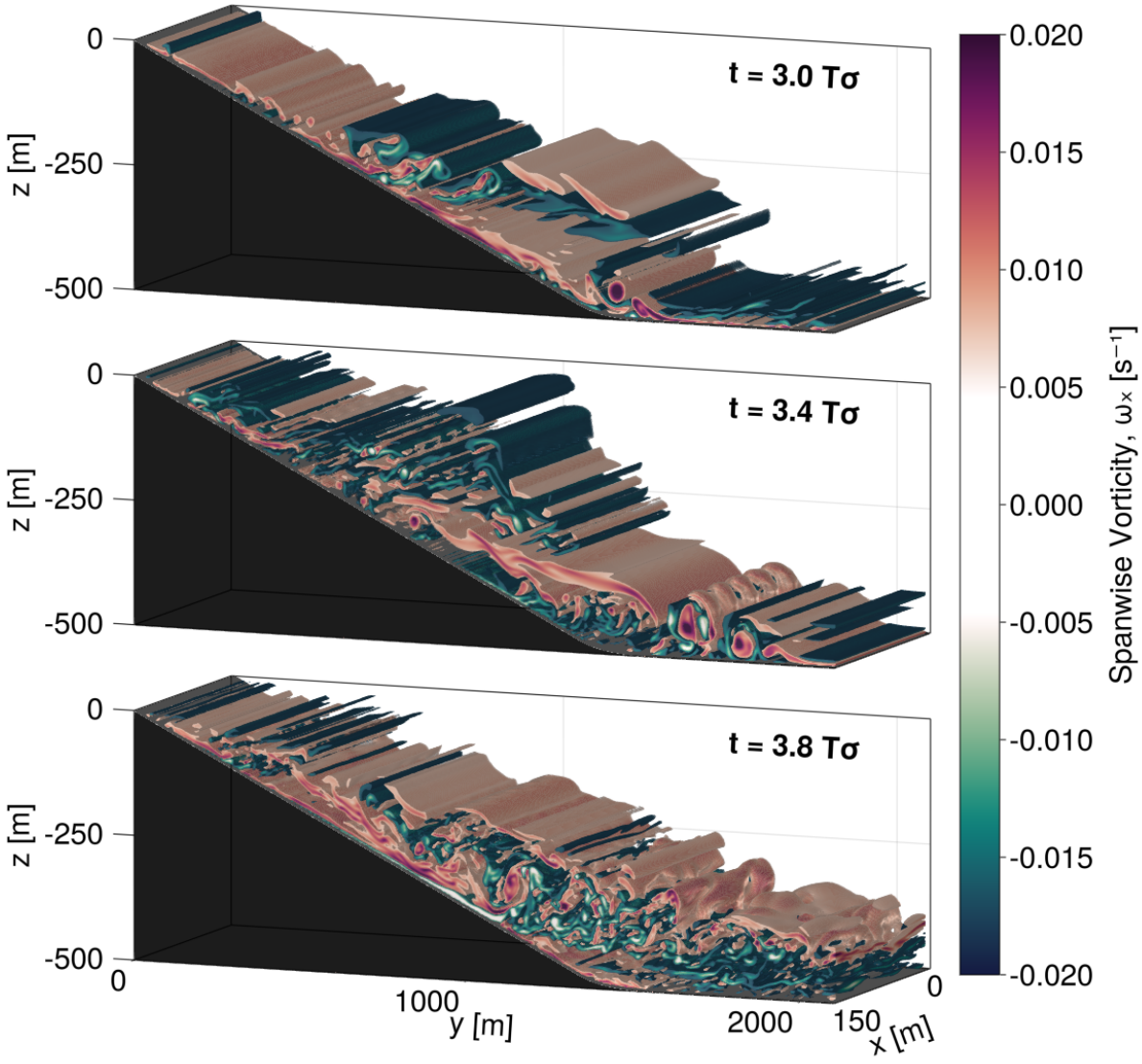



Figure 3.4: 3D contours of the spanwise ($\omega_x$) component of the vorticity for the same simulation in Fig. 3.3. Values shown at three points within the wave period indicate the development of 3D structures and the transition to turbulence. An animated version of this figure is available in the supplementary material.

tions of tidal flow over steep topography (Cyr and van Haren, 2016b; Aucan et al., 2006; Winters, 2015; Gemmrich and Klymak, 2015; Slinn and Riley, 1998). As the transition to upslope flow was particularly rapid, the upslope bore often directly interacted with the downslope overturns in these simulations. The velocity structure in the interior, away from the mixing zone, also

showed signs of wave reflection off the slope and the domain walls in Fig. 3.3. These competing velocities created multi-layered gravitational instabilities resulting in even larger overturns and more mixing. The spanwise vorticity for the same simulation shows the transition to three-dimensional turbulence during this wave period (Fig. 3.4). Along-slope vortices developed, with across-slope variations at the transition between up and downslope flow (Fig. 3.4, $t = 3.4\,T_\sigma$). The downslope breaking event caused an increase in turbulence, with smaller-scale structures appearing, and more regions of high vorticity developing along the slope. This process continued with two overturning and mixing events during each wave period, though following wave periods start with pre-existing three-dimensional structures instead of the two-dimensional overturning features seen at $t = 3.0\,T_\sigma$ in Fig. 3.4.

A survey of simulations with velocities ranging from $V_0 = 0.05$ to $0.55$ ms$^{-1}$ and stratifications between $N_0^2 = 2.56 \times 10^{-6}$ and $3.6 \times 10^{-4}$ s$^{-1}$, showed the bores, overturns, and, consequently, breaking events along the slope all follow similar patterns as described above. However, a small set of simulations run with subcritical slopes, small magnitudes of velocity, $V_0 = 0.05$ ms$^{-1}$, or strong initial stratification, $N_0^2 = 3.6 \times 10^{-4}$ s$^{-1}$, did not always show these same general characteristics and breaking events, as topographic interactions remained linear and stably stratified (Klymak et al., 2012; Balmforth and Young, 2002). Smaller velocities or stronger stratification could not be tested, since the grid resolution would not be able to capture the necessary turbulent scales in these cases.

We focus analysis in particular on the importance of what we term the *effective wave height*,

$$h_w = \frac{V_0}{N_0}, \tag{3.4}$$

where again $V_0$ is the magnitude of the wave velocity and $N_0$ is the interior buoyancy frequency (note that this parameter was denoted $\delta$ in Winters, 2015). This height scale is analogous to $h_{eff}$ but scales with the wave velocity itself rather than with the steady interior flow. It can thus be interpreted physically as the largest vertical distance a water parcel can be moved before losing all of its wave kinetic energy to potential energy (Winters, 2015; Winters and Armi, 2013). Below we show the effective wave height parameter organizes many of the simulation results across a wide range of $V_0$ and $N_0$ values, spanning $h_w$ values from 14.3 to 157.1 m (Table 3.1). Both $V_0$ and $N_0$ values were varied to produce the same range of $h_w$ (Table 3.1), ensuring the scaling relationships identified were due to the effective wave height and not changes in the wave velocity or stratification alone.

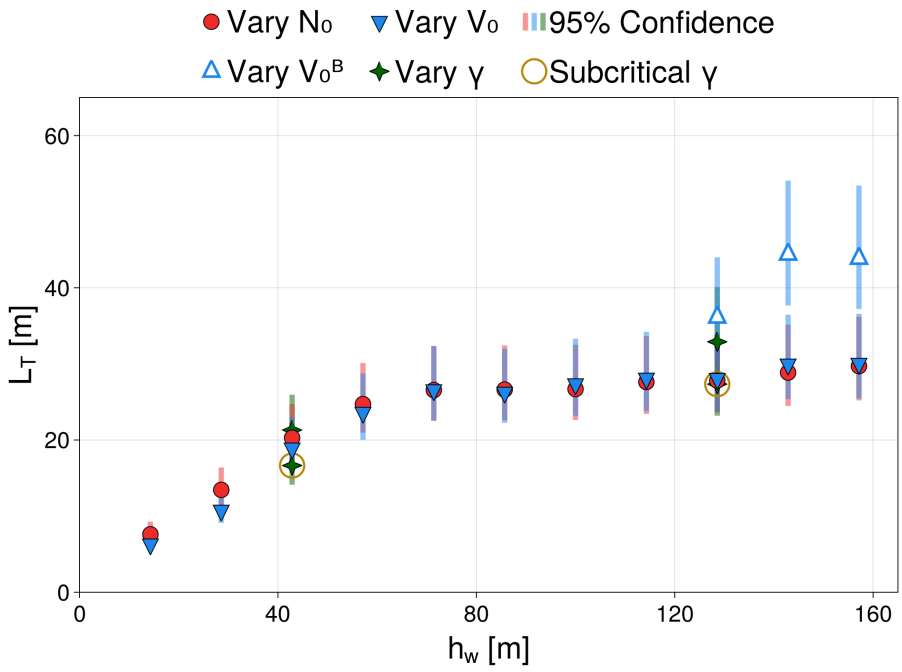



Figure 3.5: RMS Thorpe Scale, $L_T$, for each simulation is related to $h_w$. Simulations varying the slope criticality, $\gamma$, hold $N$ constant for two $V_0$ values, shown by the green stars, including for subcritical cases (gold rings). Simulations with the largest overturns have some domain dependence, as seen in the simulations with added vertical domain, $V_0^B$. Error bars indicate 95% confidence intervals on exponential distributions.

Since the effective wave height is a constraint on a parcel's vertical displacement, $h_w$ is expected to set an upper bound on the wave overturn size. Overturns can be measured with the Thorpe scale (Thorpe, 1977), defined as the root mean square (RMS) of the displacement necessary to adiabatically reorder the buoyancy profile to make it gravitationally stable. Overturns estimated from the simulations were only counted if the buoyancy range within the overturn exceeded a threshold of $\Delta b > 2\,\Delta z\,N_0^2$ and the length scale $L_T > 2\Delta z$ to avoid spurious identification of overturns not resolved by the numerical grid. Thorpe scale has often been used as a way of estimating the available potential energy from a mooring profile (van Haren and Gostiaux, 2012a; McPhee-Shaw and Kunze, 2002; Jones et al., 2020), though its efficacy is dependent on assumptions of the type of turbulence and overturns being measured (Jalali and Sarkar, 2017; Dillon, 1982; Mater et al., 2013). Instead, in these results the effective wave height, $h_w$ was compared directly to the average Thorpe scale, $L_T$, as a bulk direct measure of overturn size within each of the simulations. This relationship between the effective wave height and the resulting Thorpe average for each simulation is shown in Fig. 3.5. There was an approximately piecewise-linear relationship between $h_w$ and $L_T$, with little difference between the simulations where $V_0$ was varied as compared to $N_0$ varied, suggesting that the simple measure of the effective wave height effectively scaled the breaking events near the boundary. The small differences in overturn size for large $h_w$ simulations could be a domain dependence on the calculation of Thorpe scale as $h_w$ approaches $100$ m. A set of simulations, $V_0^B$, where the vertical domain was increased by $150$ m resulted in an increase in the measured $L_T$, consistent with this interpretation. The plateau in these averaged results also heavily sampled an increasing number of small overturns present alongside the larger overturn events discussed earlier. Therefore, the effective wave height could still be controlling the size of the largest parcel displacements, and thereby the most energetic

overturns, while the RMS estimate of Thorpe scale remained smaller. Such a domain dependence could have implications for the relevance of this scaling in shallow coastal waters, but here we focus on applications similar to the abyssal setting, where $h_w$ and overturning features are much smaller than the depth.

### 3.3.2 Overturns and dissipation in breaking waves scaled by $h_w$

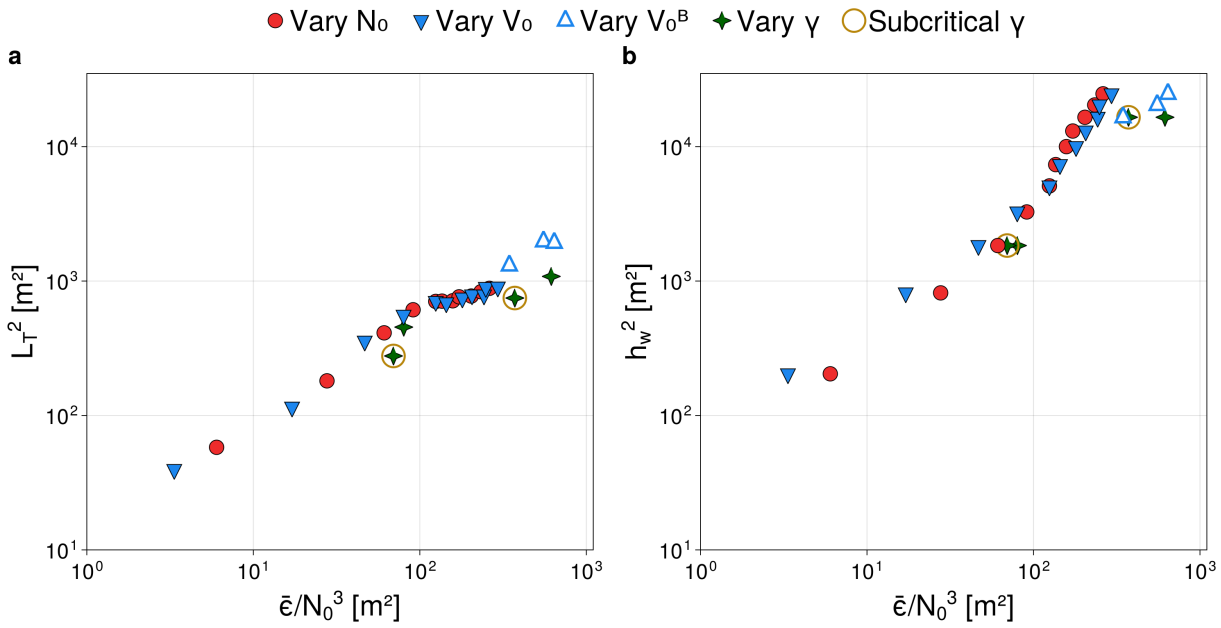



Figure 3.6: Ozmidov scale, using the average dissipation over waves 6-10, is compared to Thorpe Scale (a) and $h_w$ (b). Results are shown for simulations that vary $V_0$ (solid blue markers), holding $N_0 = 3.5 \times 10^{-1}$, and vary $N$ (solid red markers), holding $V_0 = 0.25$ ms$^{-1}$. Simulations varying slope criticality (solid green markers) and increased domain size (open blue markers) also show a similar relationship.

The approximate relationship between $L_T$ and $h_w$ suggests that the effective wave height usefully scales the bulk overturning size. This suggests that the dissipation rate may be inferred from $h_w$, in the same manner that dissipation rate is often inferred from $L_T$ (Dillon, 1982; Mater et al., 2015). This approach is based on an assumption of near-constant Richardson number

which gives that $L_O = CL_T$, where $C$ is an order-1 constant, and $L_O$ is the Ozmidov scale (Dillon, 1982). The Ozmidov scale, $L_O$ (Hopfinger, 1987), gives the size of the largest eddy not dampened by buoyancy (McPhee-Shaw and Kunze, 2002; Jalali et al., 2017), and is directly related to the dissipation rate by,

$$L_O^2 = \epsilon/N^3. \tag{3.5}$$

Thus, the turbulent dissipation rate can be estimated as $\widehat{\epsilon} \approx C^2 L_T^2 N^3$, where the carat notation is used to indicate an approximated quantity. The often-used constant value $C = 0.8$ (Dillon, 1982) results in the relationship $\widehat{\epsilon} \approx 0.64 L_T^2 N^3$. This connection between Thorpe scale and dissipation rate has been taken advantage of in observations where overturns can be quantified in profile data, including those of convective and shear-driven overturns near topography, (Alford et al., 2011; van Haren and Gostiaux, 2012a; Legg and Klymak, 2008; Cyr and van Haren, 2016b).

The relationship between the squared Ozmidov scale and the squared Thorpe scale is shown in Fig. 3.6a for varying simulations, where $\bar{\epsilon}$ is the average dissipation, calculated from model fields as

$$\bar{\epsilon} = \overline{\nu_e \left(\frac{\partial u_i}{\partial x_j}\right)\left(\frac{\partial u_i}{\partial x_j}\right)}. \tag{3.6}$$

$\nu_e$ is the eddy viscosity and $\overline{(\cdot)}$ denotes averaging over wave periods 6 through 11. The Ozmidov scale in Fig. 3.6, was calculated using (3.5), where $N$ was determined by the initial buoyancy frequency, $N_0$. As expected, the Thorpe-scale estimates of the dissipation rate reasonably approximated the true dissipation rate across more than two orders of magnitude. The Thorpe and Ozmidov relationship had a shallower slope at high dissipation rates, due to the same change in slope seen in Fig. 3.5. This flattening was less pronounced for simulations with additional vertical domain size (*Vary* $V_0^B$), suggesting (as above), some potential dependence on the com-

putational domain for the largest wave velocities ($V_0 > 0.4$ ms$^{-1}$) and weakest stratification ($N_0 < 2.1 \times 10^{-3}$ s$^{-1}$).

A similar relationship can be found by replacing the Thorpe scale with the effective wave height, as a simple approximate measure of the bulk overturn size. This gives, $L_O^2 \approx C' h_w^2$, such that the dissipation rate can be approximated using only the wave velocity magnitude and buoyancy frequency,

$$\widehat{\epsilon} \approx C' h_w^2 N_0^3. \tag{3.7}$$

The relationship between Ozmidov scale calculated using the average dissipation rate and the effective wave height for the simulations is shown in Fig. 3.6b, with a best-fit coefficient of $C' \approx 0.02$ over all simulations. This fit to the data gives a good description of the expected relative order of magnitude given a value of $h_w$. Bursts of dissipation of kinetic energy rate on the order of $10^{-6}$ m$^2$s$^{-3}$ observed near breaking internal waves in the Rockall Trough match with the estimate using (3.7), given their approximately measured stratification of $3 \times 10^{-6}$ s$^{-1}$ and wave velocity of $0.2$ ms$^{-1}$, which together imply an $h_w$ of $115$ m (Wynne-Cattanach et al., 2024; Alford et al., 2024). However we emphasize that this agreement may be simply fortuitous, and we do not claim this empirical relationship will always generalize, especially given the inherent variability found here and in observational estimates, as well as complexities of realistic bathymetry (discussed further in section 3.4). However, in the simulations considered here, $h_w$ captured the impact of both changes in the wave velocity magnitude and initial buoyancy frequency on breaking events, including for the simulations with different slope criticality. Since $h_w^2 = V_0^2/N_0^2$, there is a dependence on $N_0$ in both the Ozmidov scale and effective wave height, albeit appearing at different polynomial orders. Increasing the vertical domain size reduced the

steepness in the velocity-varying results, indicating the same dependence on the domain as Fig. 3.6a. Comparisons between these turbulence statistics and the effective wave height are further complicated by spatio-temporal variability crossing several orders of magnitude which will be explored further in section 3.33.3.3. These results, along with those of section 3.33.3.1, indicate that the simple scaling parameter $h_w$ effectively captures the bulk overturning size during these wave breaking, and hence also can be used to characterize the ensuing turbulent dissipation of kinetic energy.

### 3.3.3 Boundary layer and interior exchange through adiabatic pumping

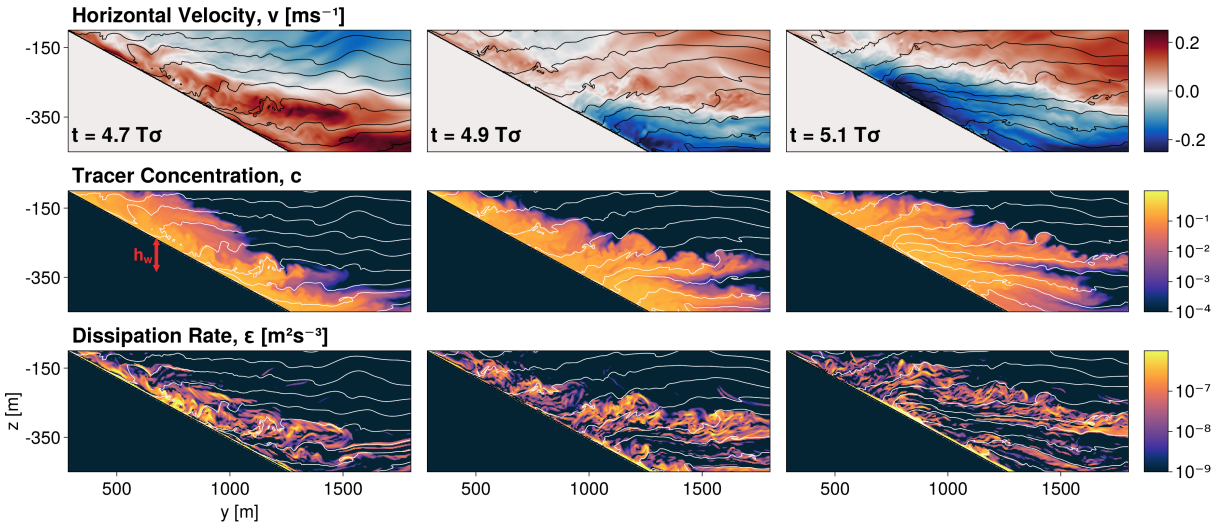



Figure 3.7: Horizontal velocity, slope-initialized tracer, and dissipation of kinetic energy rate during an ejection event. Isopycnals in intervals of $\Delta b = 5 \times 10^{-4}$ ms$^{-2}$ marked in all images. At the end of the downslope breaking event at wave period $4.7$, the water is mixed within one $h_w$ of the slope (marked in red). The upslope bore shown at wave periods $4.9$ and $5.1$ eject tracer into the interior (section 3.33.3.3).

The presence of turbulence and overturns near sloping boundaries alone does not mean breaking internal waves necessarily generate efficient mixing. To maintain efficient mixing along

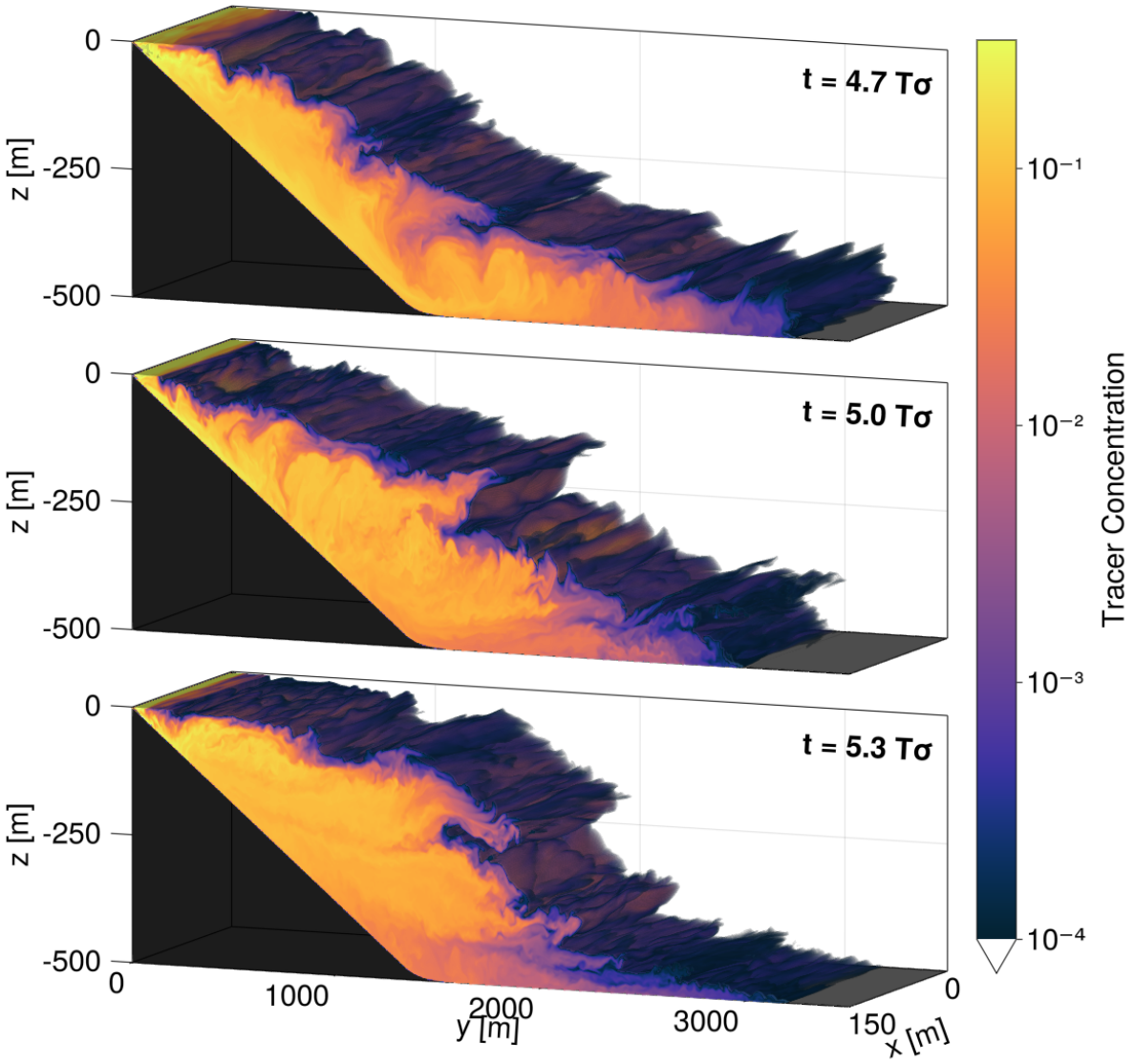



Figure 3.8: 3D contours of slope initialized passive tracer concentration (log scale) for simulation with $V_0 = 0.35$ ms$^{-1}$, $N_0 = 3.5 \times 10^{-3}$ s$^{-1}$, and $h_w = 100.00$ m. Concentrations less than $10^{-4}$ are omitted. Values are shown at three points across the 4th and 5th wave period. Tracer is laterally ejected, extending 2500 m into the interior at $t = 5.0\,T_\sigma$, the transition between up and downslope flow. A 3D animation can be found of this ejection process in the supporting information.

sloping boundaries, there needs to be a pathway for the restratification of the BBL. Understanding the exchange process requires a closer look at the temporal and spatial variations within these simulations, rather than only the integrated metrics discussed in the previous results. The break-

ing of internal waves on the downslope phase created well-mixed boundary waters right before the upslope phase began, over a vertical scale limited by the effective wave height, $h_w$. The incoming dense bore was led by a region of strong buoyancy gradients, visible in the collapsed isopycnals in Fig. 3.7. The presence of the strong downslope velocity from the previous overturn phase, coupled with the incoming dense bore, caused an ejection of the newly mixed boundary waters along the isopycnals into the interior. These intrusions can be seen in Fig. 3.7, through the slope-initialized dye and regions of increased dissipation of kinetic energy rate being expelled at $t = 5.1\ T_\sigma$. Fig. 3.8 shows three-dimensional snapshots after the tracer has been ejected into the interior (for a simulation with $h_w = 100$ m, the reader is referred to animations in the supporting information to help build further physical intuition). Over the course of a wave period, the tracer was pumped back and forth from the boundary, as indicated by the tendrils extending into and retracting from the interior. Such ejections and layers of increased turbulence or materials are often seen in numerical simulations, lab experiments, and observations (Cyr and van Haren, 2016b; McPhee-Shaw, 2006; Edge et al., 2021; Nokes and Ivey, 1989; Winters, 2015; van Haren, 2023; Wynne-Cattanach et al., 2024; McPhee-Shaw et al., 2021a).

The timing of the exchange process can also be seen by looking at phase-averaged Hovmöller plots of the near boundary region in buoyancy space. Each buoyancy class represents a region, $R(b, t)$ of size $\Delta b = 20\ \ N_0^2$ within $1.1\, h_w$ of the sloping topography, creating 25 initially equal volumes. The diagram in Fig. 3.9 indicates such a region shaded in blue. Fig. 3.10 takes the phase average over waves 4 through 10 of a representative simulation. The first row shows the average horizontal velocity (a), dissipation of kinetic energy rate (b), and stratification anomaly (c) in each buoyancy class during a wave period. The upslope phase replenished the boundary with strong stratification, while the downslope phase had increased dissipation and weak stratification,

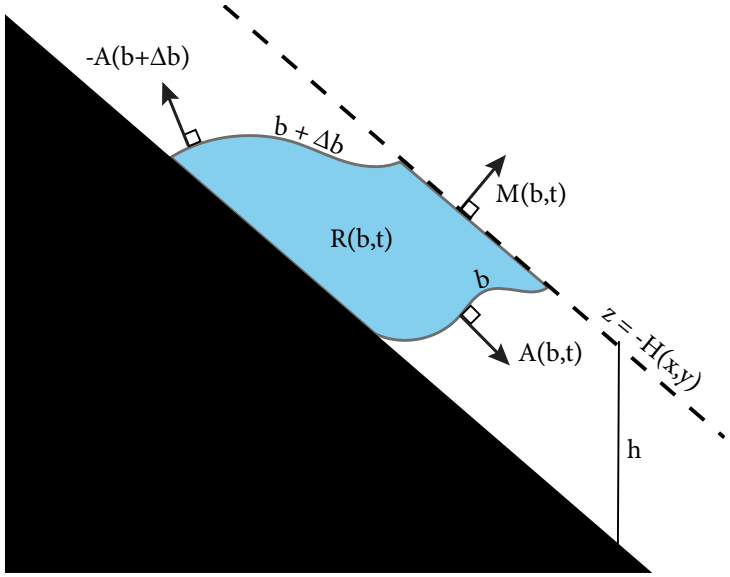



Figure 3.9: Shaded volume bounded by two isopycnals, the topography, and the fixed surface $H(x, y)$. $H(x, y)$ is a vertical distance of $h = 1.1h_w$ from the slope. The diapycnal volume flux through the isopycnal surfaces is $A$ and the flux through $H$ into the interior is $M$ (Marshall et al., 1999).

directly before the ejection. This phasing difference, with dissipation rate and stratification inversely varying, has also been seen in simulations of barotropic tides (Ruan et al., 2025; Gayen and Sarkar, 2011)) as well as in observations (Cyr and van Haren, 2016b; Nielson and Henderson, 2022; Aucan et al., 2006).

The near boundary volume of a specific buoyancy class will only be altered by the diapycnal fluxes through the isopycnal surfaces bounding the class, $A(b + \Delta b) - A(b)$, and volume fluxes into the interior, $M(b)$ (Marshall et al., 1999). The volume budget of a buoyancy class, $R(b, t)$, bounded by $b$ and $b + \Delta b$, is given by,

$$\frac{\partial V(b,t)}{\partial t} = A(b + \Delta b, t) - A(b, t) - M(b, t) \tag{3.8}$$

These terms are compared in Fig. 3.10, where positive values indicate an increase in boundary

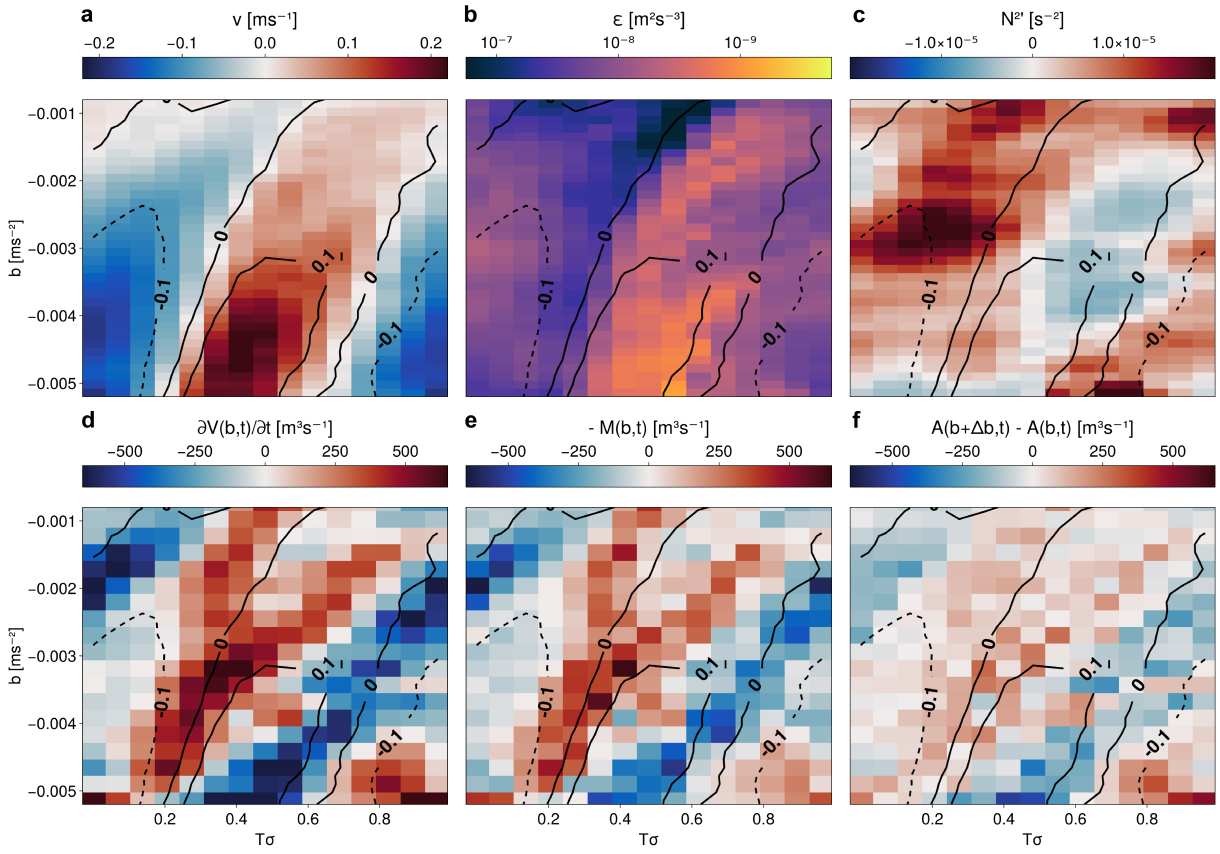



Figure 3.10: Representative simulation with $V_0 = 0.35$ ms$^{-1}$, $N_0 = 3.5 \times 10^{-3}$ s$^{-1}$, and $h_w = 100.00$ m. Row one shows the average (a) horizontal velocity, (b) dissipation of kinetic energy rate, and (c) stratification anomaly in each buoyancy bin. Row two is the buoyancy binned volume budget within $1.1h_w$ of the slope (refer to Fig 3.9 and Eq. 3.8): (d) the buoyancy class volume rate of change, (e) the flux of volume from the interior, (f) the flux through the isopycnal surfaces, calculated as the residual of (e) and (f). All are phase averaged over waves 4 - 10. Contours show the average horizontal velocity in each buoyancy class, indicating the ejections into the interior occur at the transition between up ($v < 0$) and downslope flow ($v > 0$). Dissipation rate is strongest, while stratification is weakest, during the downslope phase.

volume. The contraction and dilation of the near boundary buoyancy classes occurred at the transitions between wave phase, (along the $v = 0$ ms$^{-1}$ contours). These changes in near-boundary volume were largely balanced by the volume fluxes into and out of the interior. At the transition between downslope ($v > 0$) and upslope ($v < 0$) flow the loss of volume near the boundary was accompanied by a flux of volume into the interior ($-M(b,t) < 0$), indicating an adiabatic

pumping process, creating the exchange between the boundary and interior. The ejection of well-mixed fluid at the phase transition before the dense upslope bore restratifies the near-boundary waters, could allow for an efficient mixing process in the BBL. While most of the change in volume close to the slope was due to adiabatic motions, the residual between the $\partial V/\partial t$ and $-M$ was not negligible, indicating there were also irreversible changes due to diapycnal volume flux through isopycnal surfaces, $A(b+\Delta b) - A(b)$ during the exchange process, to be discussed more in section 3.33.3.4.

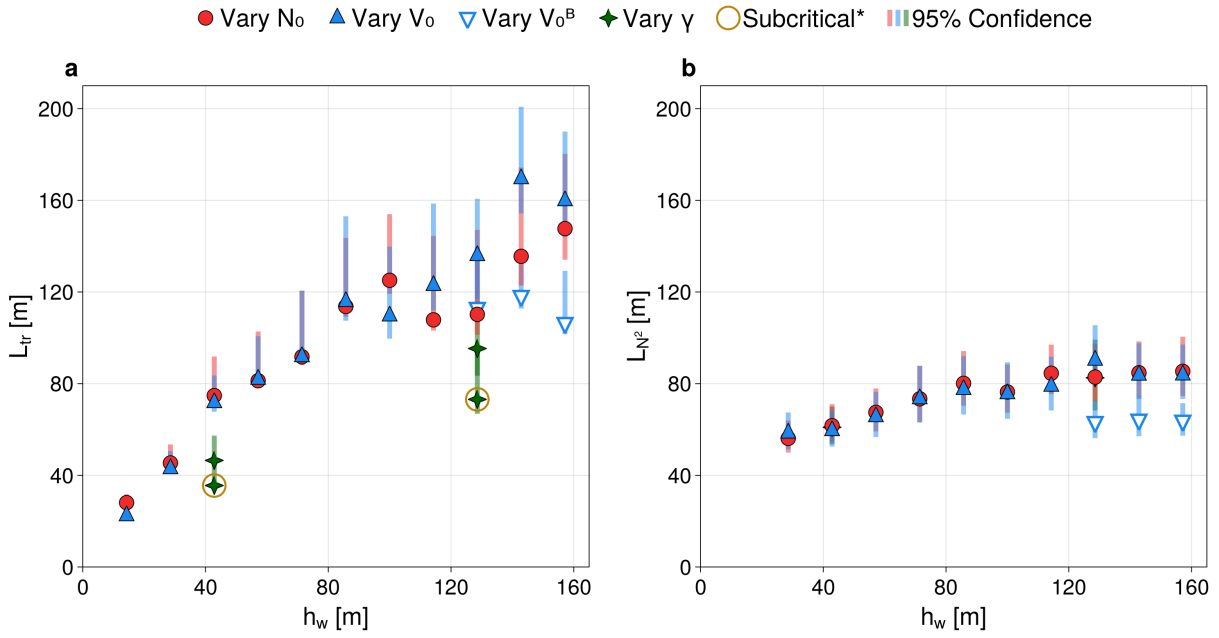



Figure 3.11: Comparing $h_w$ to the thickness of the dye intrusions away from the slope (a) and the thickness of the layers of weak stratification anomalies (b). A linear relationship of order 1 holds over simulations that vary $V_0$ and $N_0$, as well as varying the slope criticality. Subcritical simulations are not shown in panel b, as linear wave dynamics made it difficult to identify well-mixed regions using this method (Appendix B). Error bars indicate $95\%$ confidence intervals on log-normal distributions.

The exchange of fluid between the boundary layer and interior, defined by the rate, $M(b,t)$, can also be quantified using the passive tracer initialized along the slope (eg. Fig. 3.1). The along isopycnal ejections took the form of tendrils of high concentration extending into the interior

(Figs. 3.7, 3.8). For each simulation, we calculated an average tracer intrusion vertical thickness $L_{tr}$. Details of the method and associated uncertainty are given in Appendix A.1, with an example calculation in the associated Fig. A.1. The thickness of these layers in the interior scaled approximately 1-1 with $h_w$, as shown in Fig. 3.11a. We emphasize that there was significant variability in tracer intrusion sizes with each simulation, both as a function of space (distance along the slope) and wave phase, with increased variance in simulations affected by domain dependence (see *Vary* $V_0^B$ in Fig. 3.11). Using the tracer thickness diagnostic method on observations indicated a similar amount of variability. Intrusion thicknesses of dissolved oxygen anomaly as a passive tracer in the Monterey canyon ranged from $50-160$ m with a similar span in estimated effective wave height from observed stratification and current velocity measurements (McPhee-Shaw et al., 2021a; Kunze et al., 2012; Petruncio et al., 1997). Therefore, the observed relationship between $h_w$ and $L_{tr}$ should be interpreted as a bulk constraint, reflective of how the size of near boundary overturns was reflected in the thickness of intrusions resulting from boundary layer-interior exchange.

An alternate signature of exchange between the boundary layer and the interior is stratification anomalies resulting from the along-isopycnal transport of mixed water from the boundary. In a well-mixed intrusion, the buoyancy anomaly, relative to the initial condition, will be positive in the lower half of the intrusion and negative in the upper half, with related stratification anomalies (Fig. A.1c, with details of the calculation given in Appendix A.2). The stratification anomaly thickness, $L_{N^2}$, in Fig. 3.11b also scaled linearly with effective wave height, for simulations with $h_w$ up to $\sim$ 100 m, when averaged over several wave periods for each simulation. The organization of the stratification anomaly with $h_w$ emphasizes the importance of diabatic processes in wave breaking and subsequent ejection. These results again indicate that water mixed along

the lower boundary, with overturn size scaled by $h_w$, was ejected into the interior along isopycnals, setting the magnitude of this interior exchange and connecting the intrusion thickness to the along-boundary mixing.

### 3.3.4 Turbulent buoyancy fluxes

The ejection of mixed water from the boundary into the interior provides a pathway for maintaining efficient mixing, hence here we consider the associated water-mass transformation, as described by the divergence of buoyancy fluxes. Due to the nonlinear nature of the internal waves, it is convenient to decompose the perturbations into periodic wave and turbulent motions such that, (Reynolds and Hussain, 1972)

$$b = \bar{b} + \tilde{b} + b'. \tag{3.9}$$

Here, $\bar{b}$ is the mean buoyancy field, where $\overline{(\cdot)}$ indicates temporal averaging over several wave periods, $\tilde{b}$ is the periodic portion of the buoyancy field found using the phase average, $\langle\cdot\rangle$,

$$\langle b \rangle = \bar{b} + \tilde{b}, \tag{3.10}$$

and $b'$, as the residual, represents the turbulent motion. This triple decomposition using only temporal averaging results in the following equation for the evolution of the mean buoyancy,

$$\frac{\partial \bar{b}}{\partial t} + \overline{\mathbf{u}} \cdot \nabla \bar{b} = -\nabla \cdot \overline{(\tilde{\mathbf{u}}\tilde{b})} - \nabla \cdot \overline{(\mathbf{u}'b')} + \overline{\nabla \cdot \kappa \nabla b}, \tag{3.11}$$

where $\kappa$ is the eddy diffusivity calculated using the LES closure.

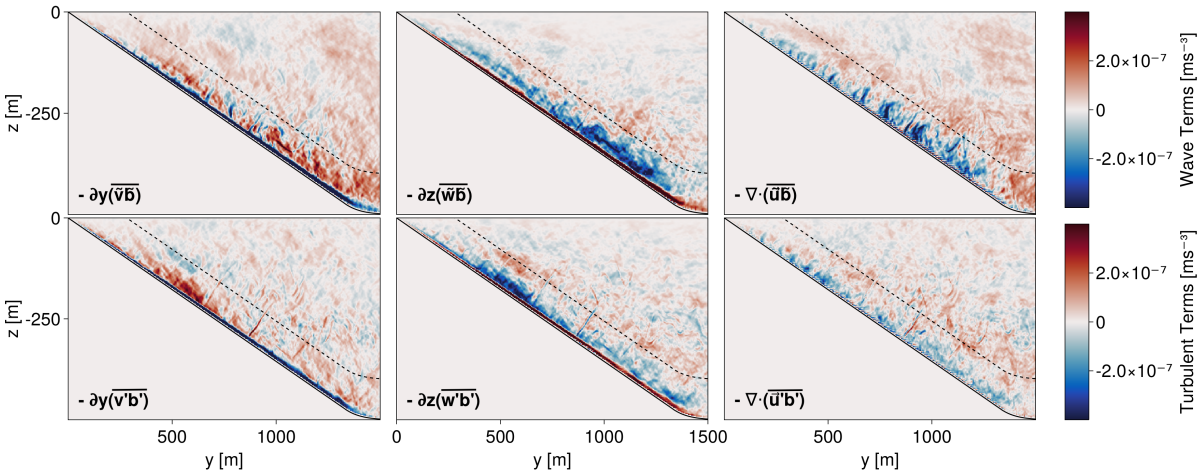



Figure 3.12: Horizontal (column 1) and vertical (column 2) components sum to the total (column 3) divergence of periodic (row 1) and turbulent (row 2) buoyancy flux perturbations. Horizontal and vertical divergences of wave-averaged buoyancy fluxes indicate the similar magnitude importance of the horizontal and vertical buoyancy fluxes to mixing along the slope, as well as a relationship between the mixed region and effective wave height, $h_w$, where the dashed line is one $h_w$ above the slope. The nonlinear wave effects dominate the buoyancy evolution, but both flux terms show near-boundary buoyancy flux divergence.

The flux divergences from the right-hand side of (3.11) are shown in Fig. 3.12. The nonlinear wave term dominated over the turbulent term, though there was little difference between the two in sign throughout the near-slope domain. Directly above the topography, there was a thin layer, $\sim 20$ m thickness, where the vertical flux convergence was positive. Similar boundary convergence has been speculated to be important for upwelling in the abyssal circulation, however critically here we note that this region of vertical flux convergence was matched by a *horizontal* flux divergence. Further from the topography, the vertical flux convergence was negative, but partially offset by positive horizontal flux convergence. Notably, in a rotated coordinate system, the slope-normal component did not have the same convergent boundary region pattern as the vertical buoyancy flux, indicating the importance of the portion of the horizontal buoyancy flux

that projects on the slope-normal direction. These results indicate the total buoyancy flux was divergent near the boundary, with convergence in the interior above the wave-breaking region, as seen in the total $-\nabla \cdot \overline{(\tilde{\mathbf{u}}\tilde{b})}$ in Fig. 3.12 (which we note is coordinate-agnostic). The effective wave height shown to scale the breaking and exchanges also scaled the height above boundary where the buoyancy flux divergence occurred (dashed line in Fig. 3.12).

The vertical buoyancy flux is often assumed to be the dominating component in boundary mixing, but these numerical results suggest both horizontal and vertical components could play a significant role due to the order-1 aspect ratio of overturns and the development of horizontal buoyancy gradients during the wave breaking events (Fig. 3.3). Buoyancy flux plots of 2D tidal simulations by Ruan et al. (2025) also show horizontal and vertical fluxes of similar magnitude, though the relatively large ratio of $h_w$ to grid-spacing in their simulations may have resulted in under-resolved wave-breaking overturns. The order-1 aspect ratio in horizontal and vertical flux variations indicated the horizontal buoyancy flux divergence could not be neglected in these simulations (cf., Holmes and McDougall, 2020). By considering both components, the near-boundary buoyancy flux convergence was canceled out entirely, and the remaining divergence within the overturning region was less than that of the vertical component alone.

The total buoyancy flux convergence in (3.11) was primarily balanced by mean buoyancy advection, such that $\partial\overline{b}/\partial t \approx 0$ (Fig. 3.13). This implies a mean Eulerian downwelling along the topography, again emphasizing the role of the horizontal buoyancy flux in canceling the thin layer of vertical buoyancy flux convergence near the bottom. However, it is important to note that the mean buoyancy did not reach a steady state during these simulations. Fig. 3.14a shows wave-averaged buoyancy (gray contours), compared to the initial condition with uniform stratification (black contours). The water at the top of the slope was getting denser, while water at the bottom

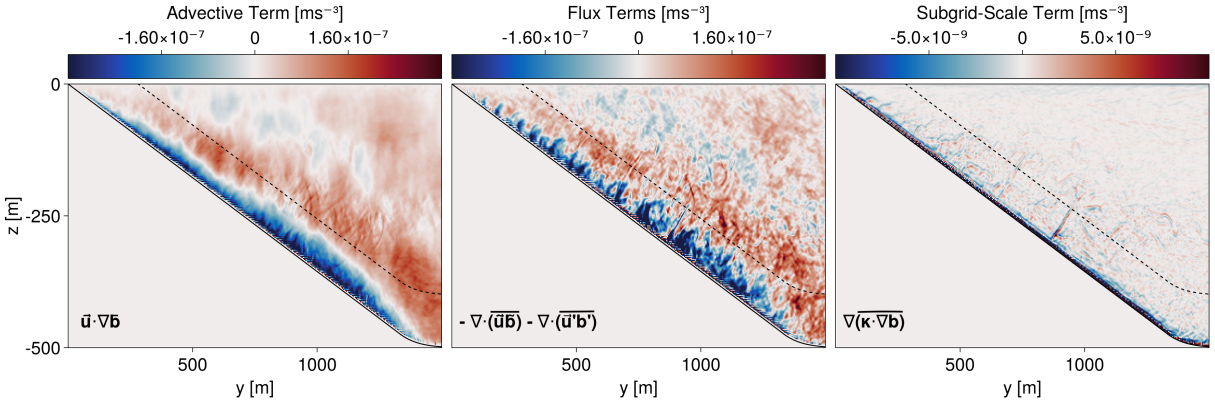



Figure 3.13: Wave-averaged buoyancy budget terms from Eq. (3.11). The flux terms (middle) are the sum of the divergences in Fig. 3.12 column 3. There is good agreement between the wave-averaged advective term (left) and the divergence of the buoyancy fluxes (middle) in a steady-state solution. The subgrid-scale term (right) is negligible.

of the slope got lighter, indicating a convergence of mass into intermediate buoyancy classes. This signature continued to intensify throughout these simulations. Compared to the relative uniformity along the slope of the buoyancy flux divergence in Fig. 3.13, the total change in wave-averaged buoyancy was much more dependent on the location of the initial buoyancy class along the slope. While the mean buoyancy budget suggests net downwelling near the boundary, the total change in buoyancy over time indicates there is variable water-mass transformation with a spatially dependent up- and downwelling pattern along the slope.

The residual in the buoyancy-binned volume budget (Fig. 3.10f) also indicated a phase-dependent diapycnal volume flux through the isopycnal surfaces, $A(b + \Delta b) - A(b)$. Diapycnal fluxes into near-boundary buoyancy classes occurred near the transition from upslope to downslope flow. While the breaking was strongest during the downslope phase, the stratification was also weakest during this phase, allowing for a difference in phase between the strongest diapycnal fluxes and the peak of the breaking event (Fig. 3.10b,c). The instantaneous near-boundary volume budget in (3.8) is wave-averaged in Fig. 3.14c (as compared to the phase-averaging in

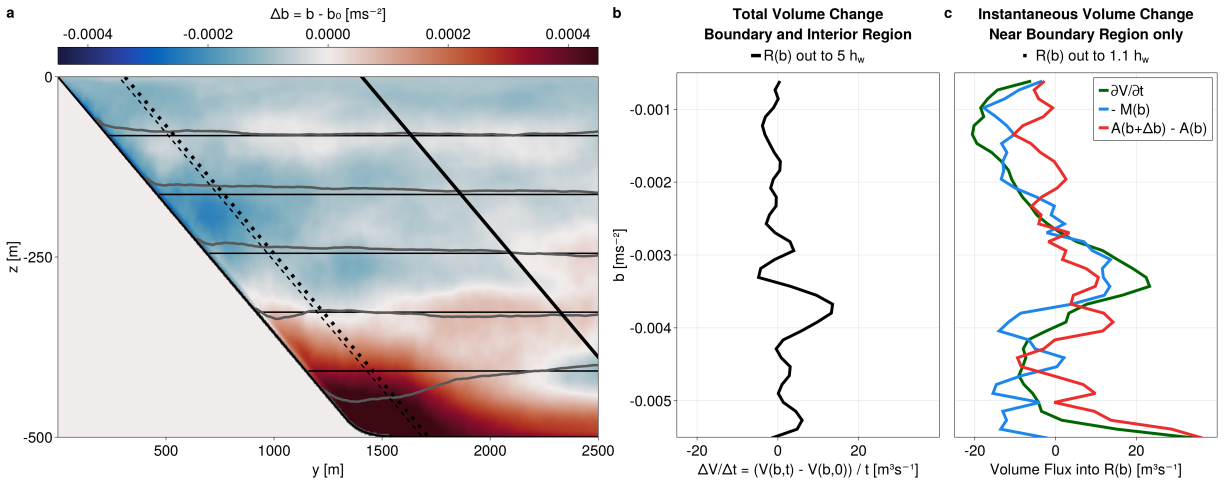



Figure 3.14: (a) shows the change in wave-averaged buoyancy, $\bar{b}$, (gray contours) compared to the initial condition, $b_0$, (black contours). Contours represent isopycnals at $10^{-3}$ ms$^{-2}$ intervals, and the thin dashed line is $1\ h_w$ from the slope, with buoyancy decreasing at the top and increasing at the bottom. Plot (b) shows the integrated volume change in buoyancy space from (a), normalized by the change in time, where $H$ is marked in (a) as the thick solid line, $5\ h_w$ from the slope. Plot (c) shows the instantaneous volume budget from (3.8) over a region extending $1.1h_w$ from the slope, with the near-boundary diapycnal buoyancy flux (red) matching the intermediate buoyancy class experiencing convergence (a) and an increase in volume in (b). All plots are wave-averaged over the same range as the phase averages in Fig. 3.10, waves 4 - 10.

Fig. 3.10) for the same simulation. There was an average gain of volume in the near boundary region through isopycnal surfaces around $b = -0.003$ and $-0.004$ ms$^{-2}$. This volume change was not as large as that of the interior-exterior transport, as that is largely balanced by reversible changes in near-boundary volume. Extending the binned region out to $5h_w$ (the thick black line in Fig. 3.14a), the total change in volume $\Delta V$ indicated a convergence of mass into a similar buoyancy class, shown in Fig. 3.14b. This differs from the profile of the wave-averaged, instantaneous volume rate of change in (c), as the change in volume in (b) is with respect to the initial condition, normalized by the total difference of time. By including interior waters, the volume changes ignored the impact of along-isopycnal motions close to the boundary, focusing on the irreversible volume fluxes. These increases culminated in a buoyancy class that is 90% larger

than it was initially. In physical space, this buoyancy class was also near the transition between the regions getting denser and lighter in Fig. 3.14a.

These results can be synthesized as follows. During the breaking events boundary fluid was mixed on time scales much smaller than a wave period, with brief moments of intense mixing and interior exchange in response to the strong downslope flow and the upslope dense bore (Fig. 3.10). The timing of water-mass transformation during the wave breaking was not necessarily coincident with the strongest kinetic energy dissipation rates, as stratification and turbulence covary (Fig. 3.10f and Cyr and van Haren, 2016b). In the time-mean, this led to a pattern of buoyancy flux divergence within $\sim 1\, h_w$ of the boundary, with horizontal flux divergences playing a significant role in the total (Figs. 3.12, 3.13). This flux divergence was largely balanced by mean downslope advection (Fig. 3.13), however, the simulations were not in steady state, such that there was an ongoing convergence of mass into intermediate density classes (Fig. 3.14). Determining to what extent these results are dependent on our numerical configuration (both domain size and treatment as an initial value problem), and what selects the convergent buoyancy class more generally in realistic settings is beyond the scope of the present work. However, the results presented here offer guidance towards interpreting observations, particularly highlighting the role of lateral fluxes, the dependence of diapycnal volume fluxes on along-slope position, and the subsequent ejection of mixed waters into the interior along-isopycnals.

## 3.4 Conclusion

Three-dimensional LES were used to demonstrate the relationship between breaking internal waves on sloping topography, overturn size, and along-isopycnal intrusions, through the

*effective wave height*, $h_w$. The simulations indicated there were two main wave breaking points within the wave period. The internal waves overturned and broke when the downslope velocity was strongest, which was followed by the rapid appearance of a dense, upslope bore and the next overturn event (Fig. 3.3). Such overturns are often seen in observations and other numerical simulations (Aucan et al., 2006; Cyr and van Haren, 2016b; Winters, 2015; van Haren and Gostiaux, 2012a; Gayen and Sarkar, 2011). Our results suggest the effective wave height, $h_w$, defined as the ratio of wave velocity to background buoyancy frequency (3.4), governed the scale of the overturns found along the slope as well as the resulting dissipation rate of kinetic energy (Figs. 3.5, 3.6).

After mixing boundary waters, the strong stratification at the head of the upslope bore forced the mixed fluid into the interior. This lateral pumping with ejections into the interior between the most energetic breaking downslope phase and the strongly stratified upslope phase is shown in Fig. 3.10. The effect of the near-boundary wave breaking was communicated into the interior through these along-isopycnal intrusions, with tracer intrusion thicknesses again scaled by the effective wave height, $h_w$ (Fig. 3.11a and see Winters, 2015). During a breaking event, fluid was mixed over a near-boundary layer approximately 1 $h_w$ thick and was subsequently ejected into the interior, resulting in stratification anomaly thicknesses in the interior also scaled by the effective wave height (Fig 3.11b). There is variability in the thickness of individual intrusions (in both time and space), however $h_w$ provides a useful bulk diagnostic and provides a connection between physical processes, from the near-boundary overturns to the boundary layer - interior exchanges and diapycnal mixing.

The total buoyancy flux averaged over several wave periods (Fig. 3.12) showed especially strong divergence within the overturning region extending a height of approximately $h_w$ above the

slope. In this region, both horizontal and vertical buoyancy fluxes contributed significantly to the total flux divergence, a consequence of the order-1 aspect ratio of overturning features along with the development of strong horizontal buoyancy gradients that preceded breaking events. While this near-slope divergence was mainly balanced by mean downslope advection (Fig. 3.13), a volume budget in buoyancy space shows there was a net diapycnal flux into intermediate buoyancy classes along the slope, with a convergence of mass due to adiabatic exchanges in nearby buoyancy classes as well (Fig. 3.14). The net diapycnal flux was driven by short bursts of intense mixing within a wave phase (Fig. 3.10), at the transition between the upslope and downslope phases. Covariances of turbulent dissipation and stratification anomalies (Fig. 3.14 b,c), along with the role of lateral fluxes (Fig. 3.12), suggest caution in the interpretation of vertical profile data or the use of time-averaged fields to infer the resulting water mass transformation.

How these results change in the presence of a more realistic slope geometry and internal wavefield—including variations in slope criticality, bottom roughness, 3D bathymetry such as canyons, and time-varying wave forcing—is an open question with important implications for understanding the net mixing during these types of breaking events. Likewise, the Lagrangian watermass evolution, in the presence of near-boundary mixing and strong interior-boundary layer exchanges could be usefully considered in future work. Results presented here give insight into the turbulent mixing generated by waves breaking on topography and suggest that the effective wave height, $h_w$, provides a useful constraint on wave energetics that can be applied to understanding the near-boundary breaking zone, adiabatic exchanges of mixed-fluid with the interior, and the rate of turbulent dissipation.

# Chapter 4: Symmetric instability and modification of near-inertial waves in dense-water overflows

## 4.1 Introduction

Gravity-driven currents descending from marginal seas and high-latitude shelves, known as dense overflows, play a crucial role in the global thermohaline circulation (Lumpkin and Speer, 2007; Killworth, 1983). Buoyancy loss from cooling as well as brine rejection during sea-ice formation (most common in some regions in the Southern Ocean) produces dense, well-ventilated waters that descend along sloping topography, transporting oxygen, carbon, and nutrient-rich water into the deep ocean, while entraining warmer ambient water (Killworth, 1983; Lumpkin and Speer, 2007; Bullister et al., 2013). Dense overflows from the Denmark Strait, Labrador Sea, and Iceland-Scotland Ridge are fundamental to the formation of North Atlantic Deep Water and therefore the Atlantic Meridional Overturning Circulation (Lumpkin and Speer, 2007; Almansi et al., 2017; Dickson and Brown, 1994; Evans et al., 2022). Similar dense overflows occur globally, including in the Mediterranean, Red, Ross, and Weddell Seas, where they transport deep and intermediate dense water (Killworth, 1983; Lumpkin and Speer, 2007; Legg, 2012). The properties of these water masses are strongly shaped by localized mixing along dense overflow pathways, yet the influence of small-scale processes, such as symmetric instability (SI) and near-

inertial waves (NIWs), on their mean flow remains poorly understood (Magaldi and Haine, 2015; Yankovsky and Legg, 2019; Qu et al., 2021b). Understanding the physical mechanisms that can govern water-mass transformation and their coupling to other dynamical pathways is therefore essential for accurately representing large-scale ocean circulation, improving global models, and informing climate projections.

The steep isopycnal slopes, strong geostrophic shear, and surface buoyancy fluxes generated by dense overflows onl create conditions that make these topographic regions highly susceptible to SI. SI is a submesoscale overturning instability triggered by negative (Northern Hemisphere) Ertel potential vorticity (PV) in strongly sheared, stratified flows. The resulting slantwise convection cells extract kinetic energy from the background geostrophic flow, contributing to a downward cascade toward dissipation and bringing the PV back to marginal stability (near zero) (Haine and Marshall, 1998; Thomas et al., 2016; Taylor and Ferrari, 2009; Chor et al., 2022). Cooling associated with dense water formation produces these negative (Northern Hemisphere) PV conditions, further favoring the development of SI (Haine and Marshall, 1998). Observational evidence of SI in dense water formation and overflow regions continues to grow (Le Bras et al., 2022; Lin et al., 2020; Brearley et al., 2012), with some studies suggesting its presence in the deep boundary currents generated by dense overflows (Yankovsky and Legg, 2019). In contrast, the results presented here show no SI in the stratified layer that forms along the boundary, but reveal active SI on the shelf above, persisting long after cooling has ceased. Propagation of SI cells towards the shelf break indicates that SI may meaningfully enhance dense overflow mixing and shelf exchange, along with the more commonly attributed changes to the geostrophic flow.

NIWs are known to interact with baroclinicity and vortical structures, enhancing high-frequency shear and mixing (Kunze, 1985; Whitt and Thomas, 2013), but how these processes

manifest near dense overflows, which share these characteristics, remains unclear. The North Atlantic and Arctic experience intense winter storm activity that injects energy near the local inertial frequency, exciting inertial oscillations and NIWs (Alford et al., 2016; Voet et al., 2024; Kunze et al., 2023). At high latitudes, the frequency of the semidiurnal internal tide is also close to inertial, further augmenting the NIW field near dense overflows (Kunze et al., 2023). Baroclinic, geostrophically balanced flows modify both the minimum frequency and the propagation angle of NIWs. The minimum allowable frequency for internal waves in the presence of a steady geostrophic background flow is also dependent on the geostrophic PV (Whitt and Thomas, 2013). The combination of slope-following isopycnals and along-slope flow commonly found near overflow pathways (Girton and Sanford, 2003; Magaldi et al., 2011; Spall et al., 2019) may promote critical reflection off the sloping topography or trapping of NIWs within slantwise critical layers (Qu et al., 2021b). Observations and simulations in other boundary current settings show that such trapping and reflection intensify vertical shear, dissipation, and bottom mixing (Qu et al., 2021a, 2022). In the North Atlantic, similar processes may transform overflow water properties before their incorporation into the Deep Western Boundary Current, with broader relevance to global overturning circulation and deep-ocean ventilation.

This study examines how the flow and stratification shaped by dense overflows influence NIW propagation and persistent SI, and how these processes extract energy from the mean flow, drive cross-shelf transport, and possibly enhance bottom mixing. Large Eddy Simulation (LES) of a dense overflow system captures key small-scale dynamics during overflow formation, propagation, and the subsequent evolution once cooling is removed and the gravity current abates. These simulated stages are representative of the temporal variability of dense overflows (Chafik et al., 2023; Magaldi et al., 2011; Köhl et al., 2007). Surface cooling initiates overflow formation

and establishes a mean geostrophic, along-isobath flow field with sloping isopycnals. Once cooling is removed, SI overturning cells are visible on the shelf, while NIWs propagate through the interior. While surface cooling reduces PV, the PV budget used in this analysis indicates these downslope currents can also inject PV, allowing subinertial NIWs in some regions while trapping them in others.

The paper is organized as follows. Section 4.2 describes the numerical configuration used to generate the dense overflow. Section 4.3 presents the evolution and dynamical behavior of the overflow, including its transition after cooling is shut off. Section 4.4 examines the PV budget and the associated boundary fluxes at each stage. In section 4.5, we characterize shelf SI behavior and its influence on PV and cross-shelf exchange, followed by an analysis of NIW propagation and associated mixing downstream in section 4.6. Conclusions and implications for future work are summarized in Section 4.8.

## 4.2 Numerical Set Up

To explore the dynamics of dense overflows, we used high-resolution LES, with a cooling surface boundary condition to develop a dense water overflow along sloping topography. The non-hydrostatic model in the Julia package Oceananigans (Wagner et al., 2025b) was used to solve the incompressible Navier-Stokes equations under the Boussinesq approximation. A ninth-order weighted essentially non-oscillatory (WENO) scheme advects velocities and tracers, with a third-order Runge–Kutta time-stepping method (Wagner et al., 2025b). Poisson's equation for the non-hydrostatic pressure is solved using a conjugate gradient iterative solver, with a fast Fourier transform-based solver as a preconditioner (Wagner et al., 2025b). We employed the explicit

Smagorinsky–Lilly subgrid-scale model for the LES turbulence closure, with a turbulent Prandtl number of $1.0$.

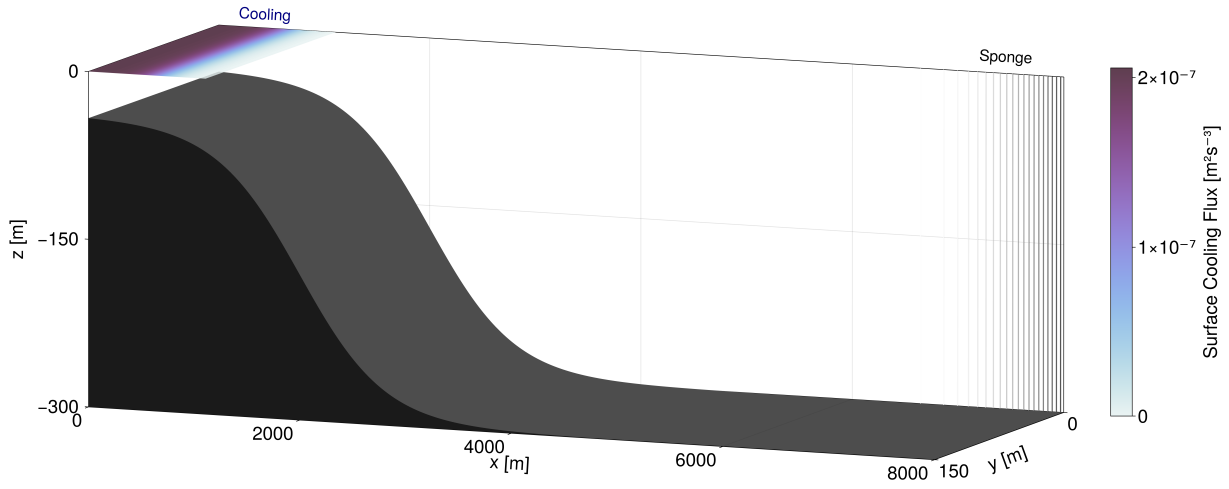



Figure 4.1: Set up for 3D dense overflow LES. Gray contours show where the sponge region was applied to $u, w$ (across-slope and vertical velocities). Blue contours and colorbar indicate the shelf region cooling from the $b$ surface boundary condition.

The domain, shown in Fig. 4.1, is three-dimensional, with size $(L_x, L_y, L_z) = (8000, 150, 300)$ m, with periodicity in the alongshore ($y$) direction and uniform grid spacing of $\Delta x = \Delta y = 4$ m and $\Delta z = 2$ m. A two-dimensional simulation with $(L_x, L_z) = (8000, 300)$ m is also used for the PV analysis in section 4.4. A $1500$ m sponge was applied on the offshore edge in $x$, damping $u, w$ velocities back to $0$ to avoid wave reflection (gray contours, Fig. 4.1). Topography was included in the simulation using a grid-fitted immersed boundary method (see Chapter 2). The topographic slope is given by a $\tanh$ function, uniform in the alongshore direction, with depths ranging from $40$ m on the shelf to the domain height of $300$ m. Boundary conditions in the bottom normal direction were no flux on buoyancy and tracers and quadratic drag on momentum.

The model begins from rest with an initial stratification of $N_0^2 = 4 \times 10^{-7}$ s$^{-2}$ and a constant Coriolis frequency, $f$, of $1.43 \times 10^{-4}$ s$^{-1}$, chosen to match values found in the Denmark

Strait, as well as previous simulations (Yankovsky and Legg, 2019). Stronger stratification was tested ($N_0^2 = 4 \times 10^{-6}$ s$^{-2}$), but resulting overflows could not propagate into the deepest part of the domain, making the former case more amenable for further analysis. A cooling flux was applied to the buoyancy as a surface boundary condition over the shelf, extending approximately $400$ m before decaying over the next $300$ m, tapering off in the interior (blue surface contours in Fig. 4.1). This negative buoyancy forcing is set to approximately $2.057 \times 10^{-7}$ m$^2$s$^{-3}$, or equivalently a heat flux of 500 Wm$^{-2}$. A smaller heat flux of $50$ Wm$^{-2}$ was also simulated with qualitatively similar results, but the larger length scales of the resulting overflow with the $500$ Wm$^{-2}$ case make explanations and visualization clearer. The buoyancy forcing is temporally constant for over 40 inertial periods, $T_f$, but is then tapered off over $5$ inertial periods, reducing the strong overflow features and entrainment-related turbulence. The bulk of the analysis is done after the cooling is shut down. The simulation is run for a total of $80\,T_f$, with a variable time step between $10^{-4}$ and $30$ s, as determined by a CFL of $0.5$ within the simulation. An inertial period is approximately $12.2$ hours, indicating a total simulation time of about $40$ days. Diagnostics were calculated every $2400$ s, except for the PV analysis (section 4.4), which required $60$ s resolution.

## 4.3 Behavior of dense-water overflows from simulations

The following discussion of the general characteristics during the simulation will be split into two stages: active surface cooling from the shelf (overflow stage, $0-40\,T_f$) and after cooling is shut down (adjustment stage, $40-80\,T_f$). The overflow stage is mainly characterized by dense water formation (Magaldi et al., 2011; Girton and Sanford, 2003; Dickson and Brown, 1994). Once surface cooling is shut off, the resulting geostrophic adjustment and development of a deep

boundary current serve as an idealized representation of the dynamics associated with surface buoyancy flux variability or the downstream response to an upstream cooling event (Chafik et al., 2023; Köhl et al., 2007; Koszalka et al., 2013; Saberi et al., 2020).

### 4.3.1 Dense water formation and overflow

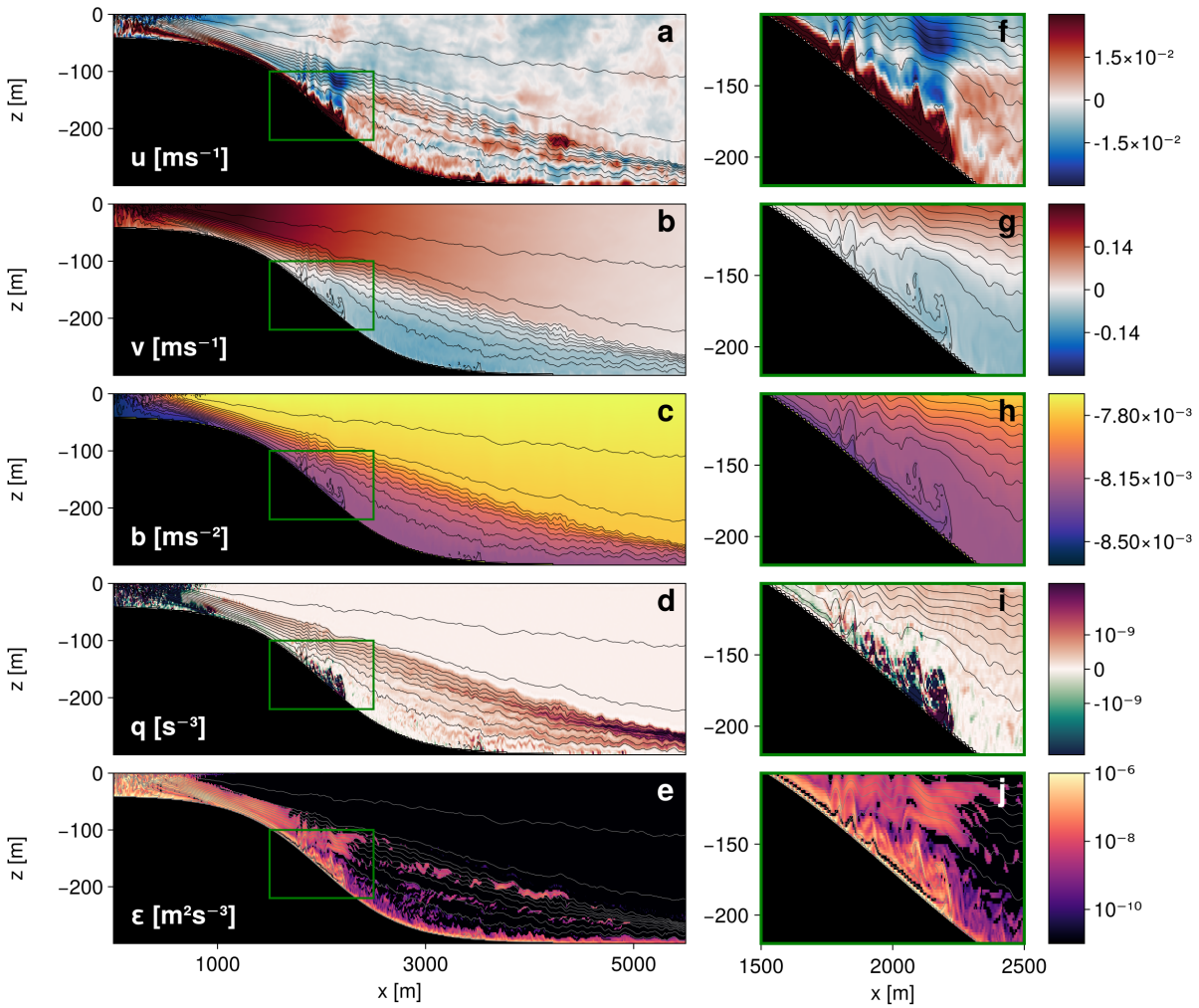



Figure 4.2: Snapshots during the cooling phase at $t = 30.5\,T_f$ of the 3D simulation at $y = 74$ m. Fields shown are the across (a,f) and along-slope (b,g) velocities, $u, v$, (c,h) buoyancy, (d,i) the Ertel PV, and (e,j) in log scale, the dissipation rate of kinetic energy. Contour lines on all plots are isopycnals from evenly spaced buoyancy classes. (f-j) is a close-up of the green box in (a-e), showing a dense pulse positive PV down the slope.

The simulation starts from rest, but surface cooling quickly generates convection on the shelf. The dense water then begins to move down the slope due to a horizontal pressure gradient arising from the density contrast across the slope, but is deflected to the right ($v < 0$) by Coriolis, undergoing geostrophic adjustment. This results in a bottom geostrophic jet ($v < 0$), and, coupled with a return flow, a surface jet above ($v > 0$) (Fig. 4.2b). The along-slope velocity speed is an order larger than $u$ (Fig. 4.2a), consistent with the flow being nearly geostrophic, though friction in the bottom boundary layer (BBL) induces a small ageostrophic component allowing the current to continue down the slope (Cenedese et al., 2004). The dense overflow results in isopycnals aligned with topography within the first 10 inertial periods (Fig. 4.2c).

During this formation stage, the shelf cooling modulates the downslope flow by producing periodic, sub-inertial pulses of newly formed gravity currents, each bringing a new, denser buoyancy class down the slope (Fig. 4.2 f–j). Similar sub-inertial overflow variability in simulations and observations has been attributed to upstream forcing, mesoscale boluses, or passing Rossby waves (Almansi et al., 2017; Girton and Sanford, 2003; von Appen et al., 2014), but in this constrained domain, these mechanisms are not viable. The periodic descent is more likely associated with the rate of cooling and shelf convection as it increases the shelf buoyancy anomaly, though more study is needed to verify this process.

Strong surface cooling and the relatively shallow domain allow for the gravity current to reach a neutral buoyancy level in the bottom depths. During the cooling period, PV decreases on the shelf, but the gravity current gains PV as it travels down the slope (Fig. 4.2i). Ertel PV, $q$, is calculated as,

$$q = (\boldsymbol{f} + \boldsymbol{\omega}) \cdot \nabla b, \tag{4.1}$$

where $f$ is the Coriolis parameter, $\boldsymbol{\omega}$ is the vorticity vector, and $b$ is buoyancy. As the flow descends along the topography, there is a frictional injection of PV that is advected along with the overflow. The periodic passage of these currents and associated injection events result in a layered history of high PV that "caps" the dense overflow at the bottom of the slope ($x \approx 5000$ m in Fig. 4.2d). This phenomenon will be explored more in section 4.4.

The simulation during the cooling period is very energetic and turbulent. With velocities near $0.04$ ms$^{-1}$, both strong vertical shear and bottom friction result in a dissipation of kinetic energy rate along the current on the order of $10^{-6}$ m$^2$s$^{-3}$ (Fig. 4.2e,j). The dissipation rate, $\epsilon$, is calculated directly from model fields as,

$$\epsilon = \nu_e \frac{\partial u_i}{\partial x_j} \frac{\partial u_i}{\partial x_j}, \tag{4.2}$$

where $\nu_e$ is the turbulent eddy viscosity. The overflow also generates a robust internal wave field propagating both in the interior and, most notably, in banded structures within the stratified bottom region along the slope ($x = 3000 - 5000$ m, Fig. 4.2a). The internal waves within the slanted layer also dissipate kinetic energy, with banded structures of dissipation of kinetic energy rate on the order of $10^{-8}$ m$^2$s$^{-3}$ in the stratified bottom interior ($x = 3000 - 5000$ m, Fig. 4.2e). This is much weaker than the dissipation along the shelf and in the current, but still important as an indicator of the physical processes involved in this region.

### 4.3.2 Adjustment after the shutdown of the dense overflow

After the cooling is shut down, the gravity current largely stops, and the system further adjusts into geostrophic balance with the strongest buoyancy gradients near the shelf-break front

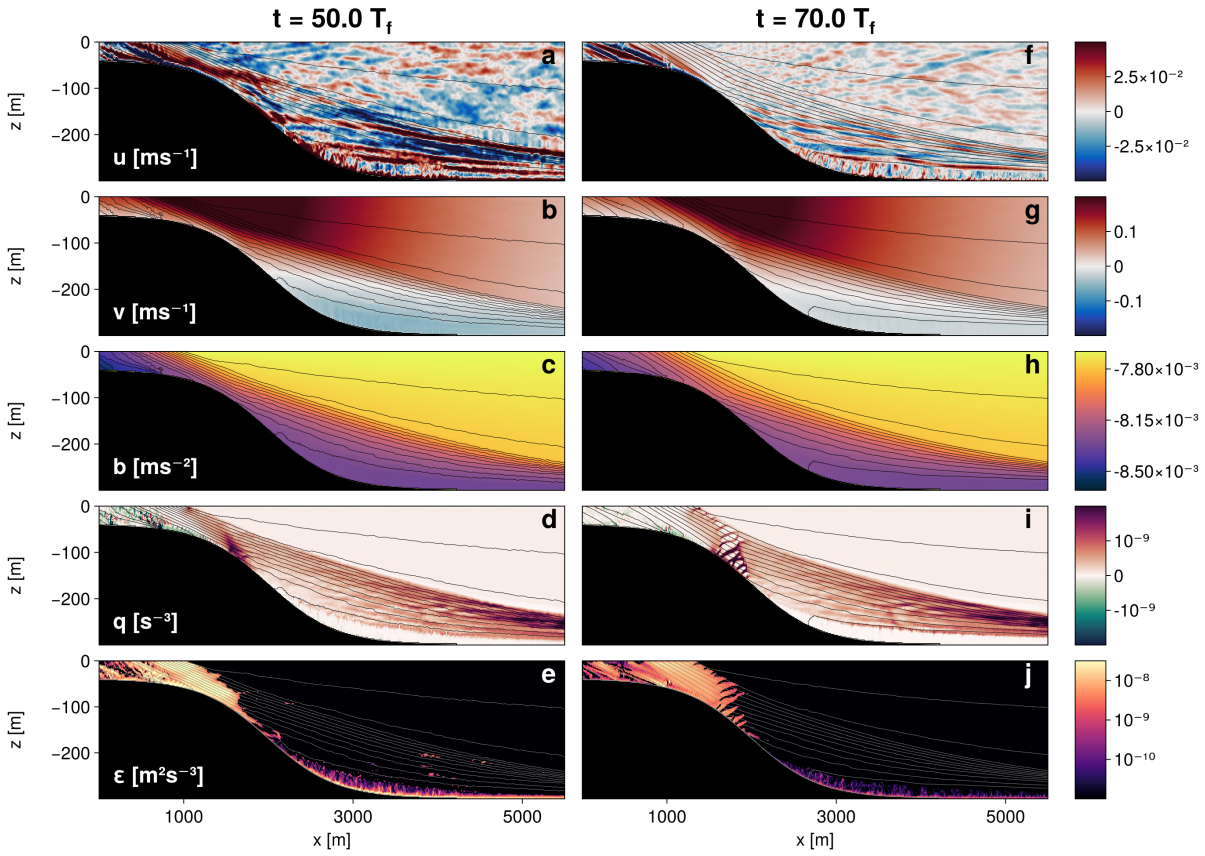



Figure 4.3: Snapshots at $t = 50\,T_f$ (a-e) and $70\,T_f$ (f-j) of the 3D simulation at $y = 74$ m, after cooling has been shut off. Fields shown are the across (a,f) and along-slope (b,g) velocities, $u, v$, (c,h) buoyancy, (d,i) the Ertel PV, and (e,j) in log scale, the dissipation rate of kinetic energy. Contour lines on all plots are evenly spaced isopycnals.

(Fig. 4.2b,c). In this second stage, the isopycnals are approximately aligned with the slope, outcropping over the shelf ($x = 700-1000$, Fig. 4.3c). The associated along-slope velocity structure remains for the duration of the simulation with a slow spin-down over time (Fig. 4.3b). Within the interior stratified layer, where isopycnals are relatively slope-aligned, the banded structures in the across-slope velocity field are much clearer ($x = 3000 - 5000$ m, Fig. 4.3a). Similar features from larger-scale dense overflow simulations have been attributed to SI (Yankovsky and Legg, 2019), but it will be shown in section 4.6 that the bands are propagating NIWs, a remnant of the internal wave field generated during cooling. There are also internal waves in the more weakly

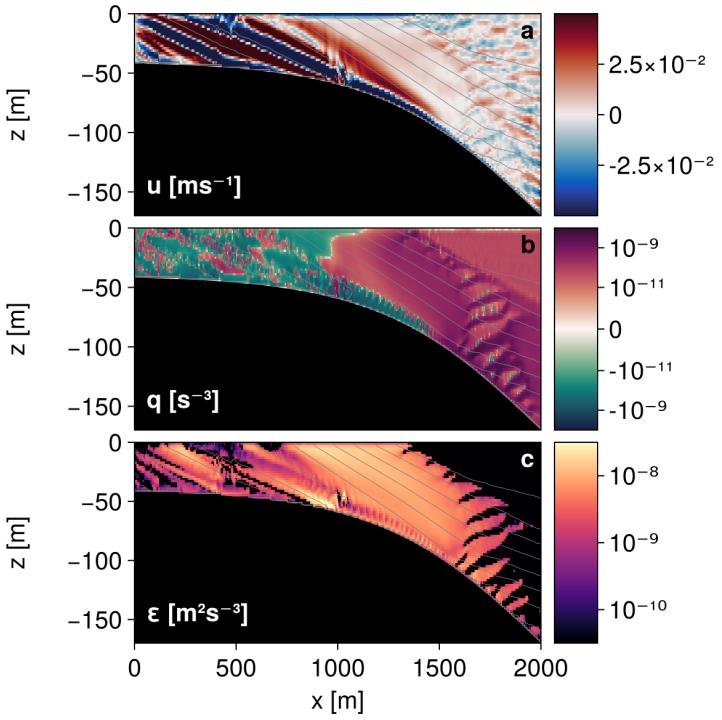



Figure 4.4: The shelf region at $t = 70\,T_f$ of the 3D simulation at $y = 74$ m. (a) across-slope velocity, (b) Ertel PV, and (c) dissipation rate of kinetic energy. Both (b,c) are on a log scale. Contour lines are evenly spaced isopycnals.

stratified upper interior, seen most clearly in the classic cross pattern from reflected waves in the $u$ velocity field (Fig. 4.3f). These waves propagate towards the shelf break, where they break and reflect, possibly causing increased mixing.

On the shelf, buoyancy-aligned overturning structures persist for the rest of the simulation (Fig. 4.4a). This, along with a continued negative PV signature (Fig. 4.4b), points to a sustained SI above the shelf break. While there is no longer constant downslope flow, there are still intermittent dense water pulses from the shelf, occurring every $3 - 5$ inertial periods. One of these pulses is visible near $x = 1000$ m in Fig. 4.4, associated with an increase in dissipation of kinetic energy at the head of the pulse. It will be shown in section 4.5 that the dense pulses are related to the across-slope propagation of SI cells. Unlike the subinertial pulsing during the

formation stage, these pulses of dense water find a resting buoyancy part of the way down the slope ($x = 1500 - 2000$ m) and do not propagate further along the topography.

The layers of high PV in the interior stratified layer ($x = 3000 - 5000$ m, Fig. 4.2d) generated by the gravity current during cooling persist after cooling is shut down, but without the gravity current advecting newly generated PV down the slope, no new layers are formed (Fig. 4.3d,i). Instead, a new feature of high PV appears on the shelf shortly after cooling is shut down, located just after the shelf break ($x \approx 1500$ m, Fig. 4.3d). The PV is generated from a combination of injection from the surface PV along the shelf break front as cooling is shut off and continued injection from the small pulses along the topography near the shelf break (to be discussed further in section 4.4). Without the continued overflow, the high PV from these near-shelf injections accumulates near their resting buoyancy height around $x = 1500 - 2000$ m. Over time, the wedge of high PV organizes into tendrils of high stratification and high PV, intermixed with weak stratification and low PV. This feature is shown in better detail in Fig. 4.4b with a change to log-scale PV indicating the low PV between the layers of high PV. The accumulation of high PV results in an accompanying wedge of high dissipation of kinetic energy rate, creating corresponding tendrils of high dissipation of kinetic energy rate in the low PV regions (Fig. 4.4c). This could be an indicator of preferential mixing from reflecting NIWs that propagate from the interior (section 4.6), as this feature continues to grow with tendrils eventually extending to the surface.

The surface cooling and subsequent dense overflow create a rich environment to study both submesoscale instabilities and NIW interactions. The slope-aligned isopycnals and high-PV capping modify the propagation of incoming waves, as discussed in section 4.6, while the negative PV generated on the shelf during cooling satisfies the instability criteria for SI (Fig.

4.4, $x < 1000$ m). The persistence of this signal over the 40 inertial periods of the adjustment stage will be examined in section 4.5. Although the following analysis primarily focuses on the more quiescent adjustment stage, these dynamics ultimately come from the cooling stage and the structures that the dense overflow establishes.

## 4.4 Potential vorticity in dense-water overflow

### 4.4.1 Description of the PV budget

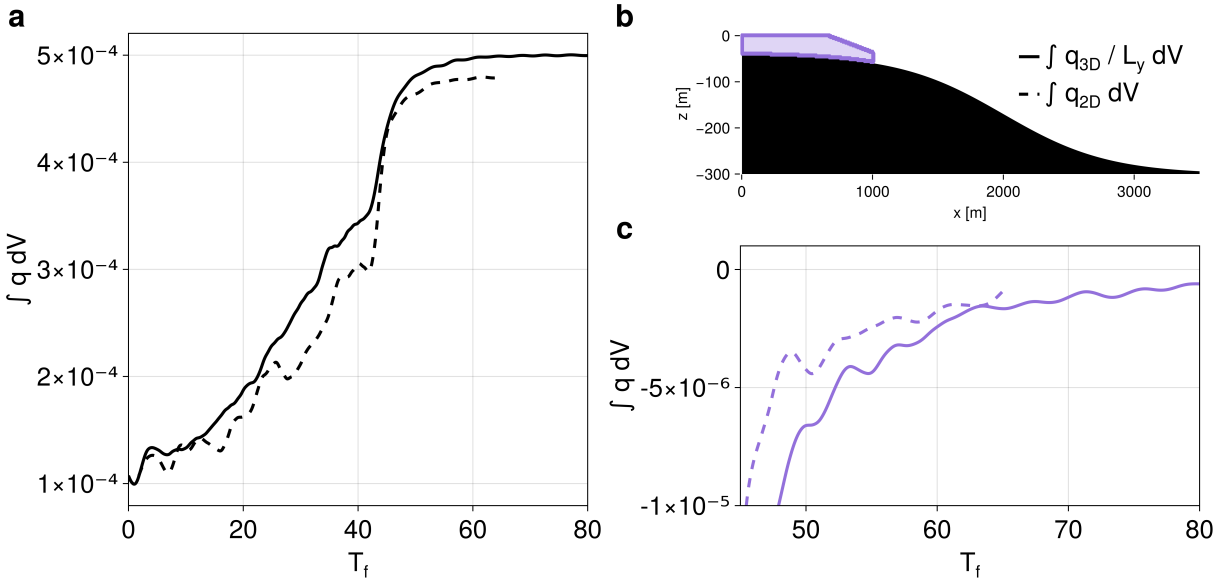



Figure 4.5: Comparison between volume integrated PV from the 2D (dashed line) and 3D domain setups shows good agreement when 3D is normalized by the along-slope width ($L_y$) (solid line). (a) volume integrated PV in the full domain. (c) volume integrated PV on the shelf (region marked in purple in (b), cut to exclude the shelf break front) after cooling has been shut off. All terms have been smoothed by averaging over a rolling window of 1.75 $T_f$.

To understand the source of the PV structures discussed above, a PV budget can show where different fluxes originate. We evaluate this in a 2D domain with $(L_x, L_z) = (8000, 300)$ m, which is computationally more efficient given the extremely high-temporal resolution (60 s)

output found to be needed to sufficiently close the PV budget. The evolution of PV in the 2D domain closely follows that from the 3D domain (Fig. 4.5), which is consistent with the 3D configuration being relatively shallow in the along-isobath ($y$) direction. Therefore, a 2D PV budget will be informative of the 3D dynamics while being cost-effective with the higher time resolution necessary for closing this budget in a turbulent system.

The Boussinesq governing equations on the $f$-plane for momentum and buoyancy are given by,

$$\frac{\partial \boldsymbol{u}}{\partial t} + \nabla \cdot (\boldsymbol{u}\boldsymbol{u}) + \boldsymbol{f} \times \boldsymbol{u} = -\frac{1}{\rho_0}\nabla p + b\hat{\boldsymbol{k}} + \boldsymbol{F} \tag{4.3}$$

$$\frac{\partial b}{\partial t} + \nabla \cdot (\boldsymbol{u} b) = \mathscr{D} \tag{4.4}$$

$$\nabla \cdot \boldsymbol{u} = 0 \tag{4.5}$$

where $\mathscr{D}, \boldsymbol{F}$ are the diffusion term and friction vector, respectively, which, for LES, include parametrized turbulent fluxes, as well as relevant boundary conditions. $\boldsymbol{f} = \langle 0, 0, f \rangle$ is the Coriolis parameter vector held constant for these simulations. Using these equations, the governing equation for PV is often written as

$$\frac{\partial q}{\partial t} = -\nabla \cdot \boldsymbol{J} = -\nabla \cdot \big( \underbrace{\boldsymbol{u} q}_{\text{Adv}} - \underbrace{\boldsymbol{\omega} \mathscr{D}}_{\text{Diab}} - \underbrace{\boldsymbol{F} \times \nabla b}_{\text{Fric}} \big), \tag{4.6}$$

where the PV can evolve due to advection (Adv), diabatic (Diab), or friction (Fric) "$\boldsymbol{J}$-fluxes". In a 2D system, where all fields are assumed to be uniform in $y$, $\boldsymbol{J}$ can also be written as

$$\boldsymbol{J} = \big( \nabla b \times \frac{\partial \boldsymbol{u}}{\partial t} \big) - \boldsymbol{\omega} \frac{\partial b}{\partial t} \tag{4.7}$$

(Schär, 1993; Marshall et al., 2001). Extensive testing here showed that (4.7) is better for closing the PV budget since the buoyancy and velocity tendency terms include any nonconservative numerical terms implicitly. With some minimal rearrangement, the components of $\boldsymbol{J}$ under the assumptions used in (4.7), can be written as

$$\text{Fric} \equiv -\boldsymbol{F} \times \nabla b = (\nabla b \times \frac{\partial \boldsymbol{u}}{\partial t}) + \boldsymbol{\omega A}, \tag{4.8}$$

$$\text{Diab} \equiv -\boldsymbol{\omega}\mathscr{D} = -\boldsymbol{\omega}\frac{\partial b}{\partial t} - \boldsymbol{\omega A} \tag{4.9}$$

where $\boldsymbol{A} = w\frac{\partial b}{\partial z}\hat{\boldsymbol{i}} + u\frac{\partial b}{\partial x}\hat{\boldsymbol{k}}$ is the flux of PV due to vertical (horizontal) advection of the vertical (horizontal) buoyancy gradient. While (4.7) will be used to calculate the PV budget due to its comprehensive inclusion of all resolved and parameterized processes, the following discussion will use the classical frictional and diabatic terms to explain the evolution of PV in the simulation, since they are equivalent.

Taking the integral over a fixed volume, $V$, and assuming no advection through the boundary, $\partial V$,

$$\frac{\partial}{\partial t}\int_V q\big|_{2D} dV = \oint_{\partial V} -\Big(\text{Fric} + \text{Diab}\Big) \cdot \hat{\boldsymbol{n}}\, dS. \tag{4.10}$$

The formulation in (4.10), along with the definitions in (4.8, 4.9), shows the steady-state conservation of PV in $V$, indicating that only boundary fluxes changing the buoyancy or velocity can have net PV effects. Expanding (4.10), with the frictional and diabatic formulation,

$$\int \frac{\partial q}{\partial t}\Big|_{2D} dV = \oint_{\partial V} \Big( \underbrace{(-\frac{\partial v}{\partial z}\mathscr{D})\hat{n}_x}_{\text{Diab}_x} + \underbrace{(\frac{\partial b}{\partial z}F^y)\hat{n}_x}_{\text{Fric}_x} + \underbrace{((f+\frac{\partial v}{\partial x})\mathscr{D})\hat{n}_z}_{\text{Diab}_z} + \underbrace{(-\frac{\partial b}{\partial x}F^y)\hat{n}_z}_{\text{Fric}_z} \Big)\, dS, \tag{4.11}$$

where $\langle \hat{n}_x, \hat{n}_z \rangle$ is positive (negative) for fluxes from the top (bottom) and right (left) boundaries. The four terms in (4.11) are labeled by whether it is a diabatic or frictional contribution, as well as whether it is a flux from the horizontal or vertical boundaries. Instead of the more general '$z$' subscript to denote vertical fluxes, a superscript will be used to further differentiate between top and bottom fluxes in some analysis, such that $\text{Fric}^{\text{top}} = -\frac{\partial b}{\partial x} F^y \big|_{z=0}$ and $\text{Fric}^{\text{bot}} = \frac{\partial b}{\partial x} F^y \big|_{z=\text{topo(x)}}$, with equivalent expressions for $\text{Diab}_z$. topo(x) is the bottom boundary based on the topography. Some results will be discussed in terms of the total PV flux from a given boundary. For instance, the "top" PV flux is the net flux from the frictional and diabatic contributions along the surface: $\text{Fric}^{\text{top}} + \text{Diab}^{\text{top}}$. The topography is a grid-fitted boundary, and therefore, there are left PV fluxes along the topography. For ease of description and as these are qualitatively fluxes along the sloping bottom, the contributions from Fric, $\text{Diab}^{\text{left}}$ along the topography will be included in Fric, $\text{Diab}^{\text{bot}}$ or "Bottom", when labeled in plots.

### 4.4.2 PV evolution during dense water formation and overflow

The volume integrated PV (Fig. 4.5a) indicates a net positive tendency in this configuration with a sharp increase when cooling is shut off ($t = 43\,T_f$), before leveling off for the rest of the simulation. The rate of change in volume-integrated PV over time ($\partial_t \int q dV$, Fig. 4.6a) also indicates a net increase in PV during cooling, with a sharp peak at $t = 43\,T_f$. After cooling is shut down, the net rate of PV injection is much smaller and steadily decreasing, but remains positive for the duration of the simulation (Fig. 4.6d). The residual from the calculated budget from (4.11) indicates a small underrepresentation of the evolution of the volume integrated PV, with a mean residual of $2.7 \times 10^{-11}$ m$^2$s$^{-4}$ during cooling and $4.6 \times 10^{-12}$ m$^2$s$^{-4}$ after cooling

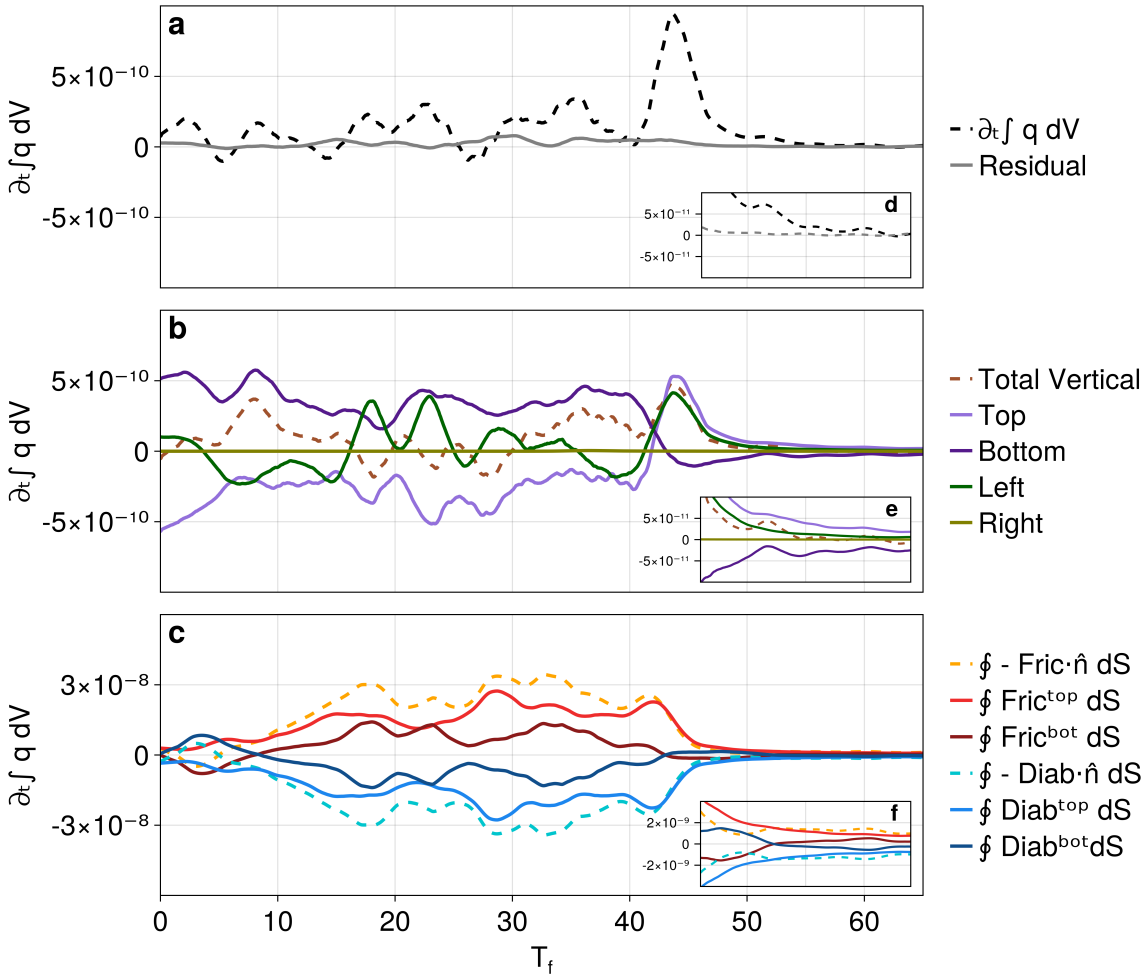



Figure 4.6: Evolution of the volume integrated PV along with the components of the budget from (4.11). (a) rate of change of PV (black, dashed) calculated directly from the left-hand side of the PV budget (4.11), along with the residual (gray, solid) from the right-hand side of (4.11). Terms from the PV budget are divided into (b) the flux contribution of each boundary wall and (c) the friction and diabatic components, as discussed in section 4.4.1 with total components in (4.10). The subplots (d-f) cover the time period where the box sits ($t = 46 - 64\, T_f$), with smaller vertical axes limits, to be able to see the flux contributions after cooling is shut down. All terms have been smoothed using a rolling average with a window length of 3 $T_f$.

has shut down (Fig. 4.6a).

The positive tendency in the volume integrated PV is due to contributions from the vertical fluxes as well as from the left boundary (Fig. 4.6b). The positive flux from the left wall arises from the return flow above the dense overflow, where geostrophic adjustment creates acceleration

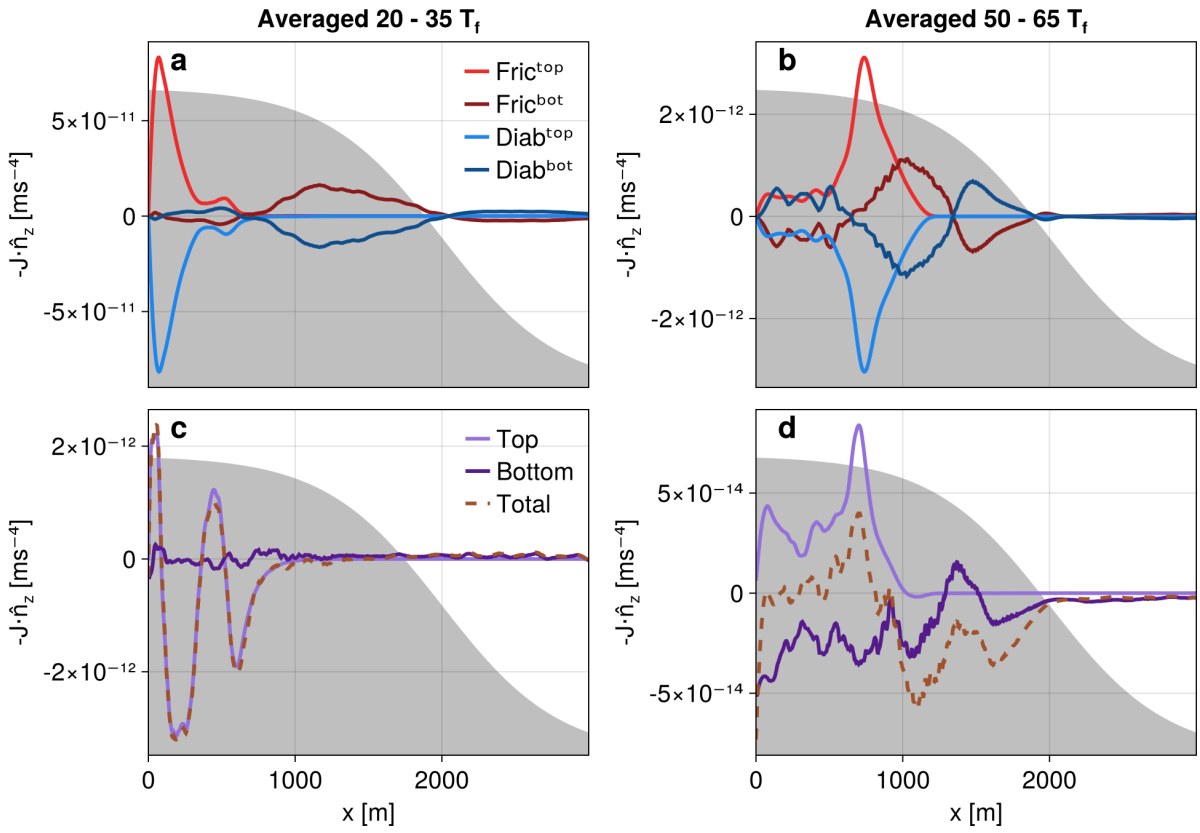



Figure 4.7: Contribution to the vertical flux terms in the $x$ direction before integrating (4.11), averaged over equivalent amounts of time during the cooling period ($20 - 35T_f$, a,c) and after cooling has completely shut down ($50 - 65T_f$, b, d), highlighting the location along the slope where different vertical PV flux components dominate. (a,b) split the fluxes by both the location and physical component of the flux, while (c,d) show the net vertical flux along the top and bottom wall, as well as their combined contribution. Values are smoothed in $x$ by averaging over a rolling window of $40$ m.

along the back wall in the presence of negative stratification. This causes a diabatic flux since cooling increases the density at the surface, but along the left wall, the dense fluid is carried down into lighter ambient fluid, resulting in a positive Lagrangian buoyancy evolution, and therefore a large positive contribution to the total PV. While the integrated left flux is of similar magnitude to the vertical fluxes, the individual positive and negative flux contributions from the vertical PV fluxes are responsible for the important local dynamical processes that contribute to NIW modi-

fication in the interior and SI on the shelf. Therefore, the subsequent discussion will concentrate on the local vertical PV flux patterns along the slope and shelf, where the competing injection and destruction of PV reveal the underlying impact of the overflow behavior.

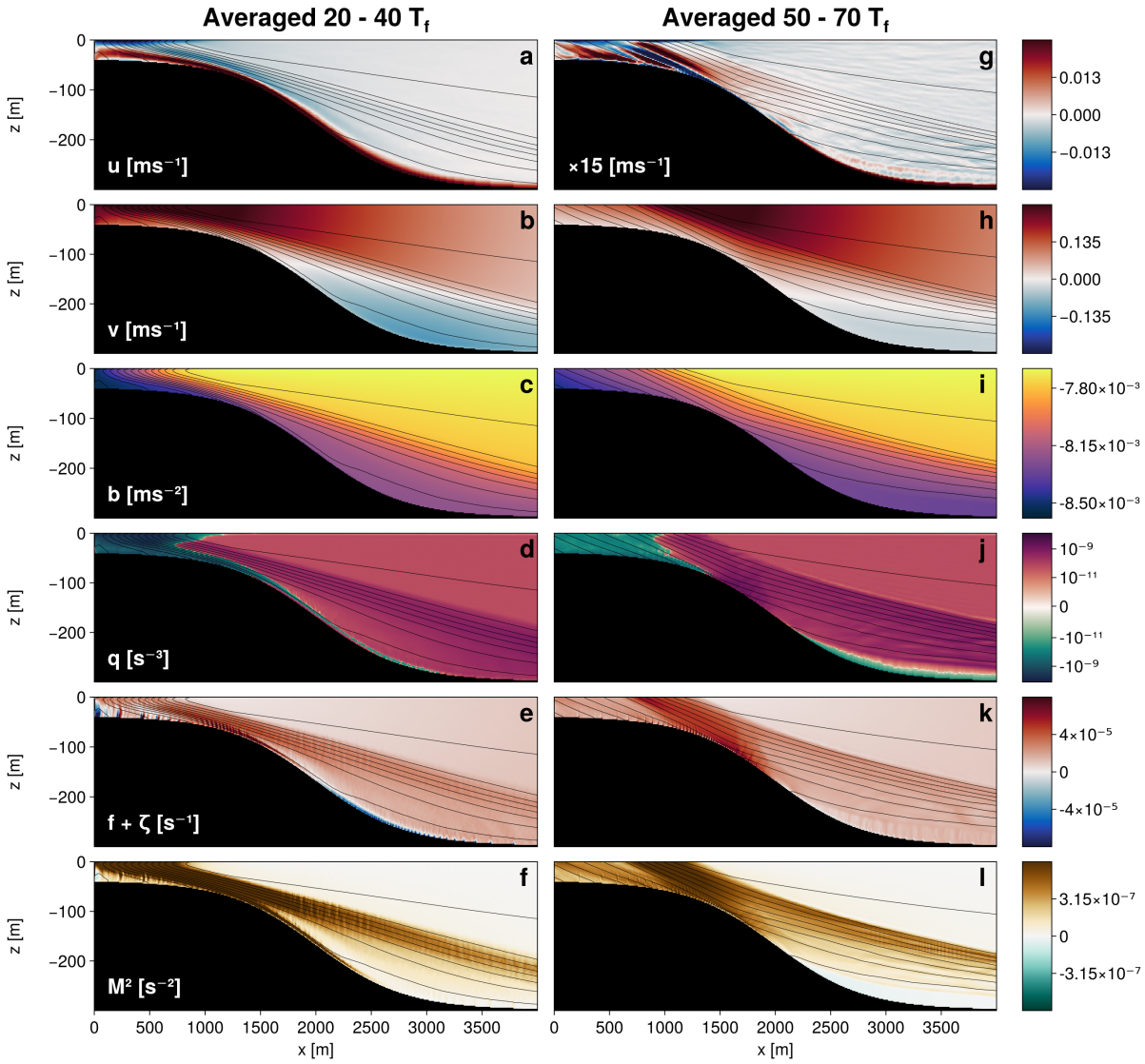



Figure 4.8: Long-term averages over $20-40\,T_f$ (a-f) and $50-70\,T_f$ (g-l) from the 3D simulation. (a,g) across-slope velocity, $u$, where (g) is multiplied by $15$ ms$^{-1}$ to be able to show both the dense overflow and the weaker magnitudes found after cooling is shut off, (b,h) along-slope velocity, $v$, (c,i) buoyancy, (d,j) PV, (e,k) total vertical vorticity, and (f,l) horizontal stratification, $M^2 = \partial b/\partial z$. Uniformly spaced isopycnals are included as contours in all plots.

During the cooling stage, the negative diabatic flux dominates the net surface contribution

(Fig. 4.6b,c). Before spatially integrating, the average $\text{Diab}^{\text{top}}$ contribution during cooling (Fig. 4.7a) is constrained to the shelf region where cooling is forced ($x < 600$ m) in the presence of the positive horizontal gradient in the along-slope flow (Fig. 4.8e). Surface frictional stresses from the along-slope flow along the positive buoyancy gradient are also injecting PV during this time (Fig. 4.6b), but the total surface PV flux is mostly negative on the shelf (Fig. 4.7a,c).

The average bottom fluxes during cooling, shown in Fig. 4.7a, are variable in sign along the topography, with the diabatic and frictional terms remaining opposite to each other. Below the cooling region, where the surface fluxes are strong, there is a small, negative frictional PV destruction that dominates over a positive diabatic flux. In this region, a frictional deceleration of the along-slope flow in the presence of a positive buoyancy gradient destroys PV. The across-slope velocity, $u$, is upslope ($x < 700$, Fig. 4.8a), bringing light water into the denser shelf environment. Positive vertical vorticity (Fig. 4.8e) and this negative Lagrangian evolution of buoyancy on the shelf result in the positive $\text{Diab}^{\text{bot}}$ (Fig. 4.7a). The negative along-slope stress and upslope flow could be indicative of upslope Ekman transport causing the local destruction of PV. The idea of upslope Ekman flow destroying PV runs contrary to more classic sloping bottom Ekman results, due to the positive horizontal buoyancy gradient found on the shelf (Benthuysen and Thomas, 2012). Usually, upslope Ekman transport would bring dense water up, but here the shelf is denser upslope.

Closer to the shelf break, the gravity current impinges on the bottom topography, changing the sign of the friction and diabatic fluxes ($x = 800 - 2000$ m, Fig. 4.8a) with the downslope flow inducing a negative along-slope flow (positive along-slope stress) and carrying buoyancy towards lighter water. The strong, positive buoyancy gradient near the shelf break front along the bottom topography (Fig. 4.8f) causes an injection of frictional PV with the passing of the dense

pulses. This positive PV signal from $\text{Fric}^{\text{bot}}$ is advected by the current. An example of this high PV being carried by the gravity current is shown at $x = 2500$ in Fig. 4.2i. This advected high PV resides in the interior stratified layer ($x = 3000 - 5000$ m) as a layered history of the injected PV carried by the new buoyancy class generated by each gravity current (Fig. 4.2d, 4.8d). While some simulations of dense overflows have found layers of negative and positive PV in the interior stratified region (Yankovsky and Legg, 2019), our setup only shows positive PV (Fig. 4.8), with only a small, growing BBL with weakly negative PV at the bottom of the slope, most visible after cooling is shut off (Fig. 4.8j).

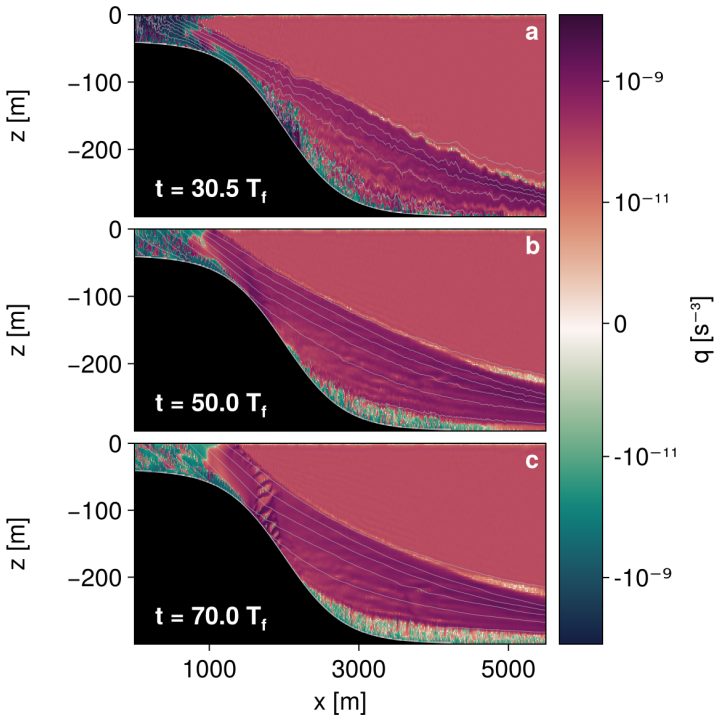



Figure 4.9: PV on a log color scale from the 3D simulation at $y = 74$ m for the three times shown in Figs. 4.2 and 4.3: (a) $t = 30.5\,T_f$, (b) $t = 50.0\,T_f$, and (c) $t = 70.0\,T_f$. Contour lines are evenly spaced isopycnals.

At the bottom of the slope, $x = 2000 - 3000$ m, the bottom fluxes change sign again (Fig. 4.7a). In this region, the stress on the negative along-slope velocity results in a reduction in

the along-slope velocity magnitude near the boundary compared to the geostrophically balanced flow in the stratified interior. Due to the steep sloping topography in this region, this results in a negative horizontal velocity gradient and anticyclonic vorticity along the boundary (Fig. 4.8e). The gravity current continues to bring dense water into lighter regions, causing a small dominating injection of PV on the bottom boundary (Fig. 4.7c). This injection of PV is minimal, and most likely not the driving force in the high PV found at the bottom of the slope, compared to the larger frictional injection at the shelf break clearly advected by the dense pulse ($x = 2000$ m, Fig. 4.9a). The integrated bottom fluxes during cooling are consistently positive, while integrated $\text{Diab}^{\text{bot}}$ remains negative, highlighting the relative importance of the injection by $\text{Fric}^{\text{bot}}$ at the shelf break (Fig. 4.6b,c).

The surface diabatic fluxes explain the negative PV found on the shelf ($x < 1000$ m, Fig. 4.9a), while the gravity current flowing past the shelf break injects positive PV along the bottom boundary. It is this injection that is responsible for the positive PV found in the stratified bottom interior ($x = 3000 - 5000$ m, Fig. 4.8d). Though the bottom PV fluxes are significantly weaker than the surface cooling flux, once integrated the surface PV destruction is only moderately dominating over the bottom injection (Fig. 4.6b). Both the diabatic cooling flux and the frictional injection have big impacts on the resulting features found within the dense overflow during cooling.

### 4.4.3 PV evolution after the shutdown of the dense overflow

There is a distinction between the behavior of the PV as cooling shuts down ($t \in 40 - 45\, T_f$) and after cooling has shut off completely and the domain is no longer as turbulent ($t >$

$45\,T_f$). When cooling shuts down, the PV fluxes decrease dramatically, as seen in the loss of magnitude in Fig. 4.6, but in the process of frontal adjustment, there is also a brief strong surface injection (Fig. 4.6a). On the shelf, in the absence of a cooling flux, the buoyancy on the surface stabilizes, resulting in a quick reduction in the $\text{Diab}^{\text{top}}$ magnitude. As the previously buoyancy-forced gravity current dies off, the velocity comes more into geostrophic balance with the slanted isopycnals (Fig. 4.8h). Frontal adjustment drives a rapid increase in vertical shear at the shelf-break front, where the buoyancy gradient is strongest, producing a strong, localized PV injection along the front. There is an abrupt change in the sign of the top PV flux near $t = 45\,T_f$ in Fig. 4.6b, mirrored in the total rate of change of PV in Fig. 4.6a as it is suddenly dominated by the positive frictional flux instead of the negative diabatic cooling flux. The bottom fluxes do not play a major role during this time, with the total vertical PV flux dominated by the surface during the shutdown (Fig. 4.6b). It is this flux that causes the sharp jump in the volume integrated PV as cooling is shut down (Fig. 4.5a) in both the 3D and 2D simulations. It is also this flux that initiates the high PV wedge at the shelf break in Fig. 4.8j, where the PV injected at the surface finds a resting buoyancy class.

After the transition period, the fluxes are more than an order of magnitude smaller than during the cooling, but their horizontal structure remains similar (Fig. 4.7b,d). The top fluxes are now net positive, and the bottom negative (Fig. 4.6e). The peak in the surface PV flux has moved to the shelf-break front due to the frontal adjustment discussed above (Fig. 4.7b). The along-slope shear is concentrated where the largest buoyancy gradients remain, producing strong surface velocities seen at the shelf break (Fig. 4.3h,l). The relative vorticity maximizes where the horizontal shear is strongest (Fig. 4.8k). The positive along-slope flow on the shelf and a mean upslope flow in $u$ (Fig. 4.8g,h) is possibly consistent with an on-slope Ekman transport along the

surface and the bottom (MacCready and Rhines, 1991). Since the shelf waters are still denser than the interior from surface cooling, there is a positive lateral buoyancy gradient (Fig. 4.8j). Therefore, $\text{Fric}^{\text{top}}$ is positive while $\text{Fric}^{\text{bot}}$ is negative on the shelf (Fig. 4.7b). As during cooling, this frictional destruction of PV runs counter to classic upslope Ekman transport along sloping bottom topography due to the positive buoyancy gradient on the shelf (Benthuysen and Thomas, 2012). In this region, the frictional fluxes dominate over the diabatic contributions, with a small net PV injection from the surface (Fig. 4.7d).

The change in sign of the friction and diabatic fluxes along the shelf at the shelf break in Fig. 4.7b is due to the convergence of the dense pulses along the bottom that are propagating towards the shelf-break front. At the edge of the front, in these periods of convergence, mixing increases, eroding stratification along the bottom. This process reduces the local PV, producing a briefly dominant region of negative $\text{Diab}^{\text{bot}}$, and a local destruction of PV (Fig. 4.7d). The temporal variability in the shelf processes and ultimately inefficient stabilization and slow injection of PV on the shelf are further discussed in section 4.5. The rest of the slope above $x = 2000$ m experiences an upslope return flow in the shelf-break front along the bottom topography (Fig. 4.8g), resulting in similar fluxes as higher on the shelf, with a net bottom destruction of PV coming from the frictional component (Fig. 4.7d).

The surface cooling and subsequent dense overflow create a rich PV field, with features such as the banded high PV in the interior stratified region, the high PV wedge along the shelf break, and the negative PV on the shelf. These features make the shelf unstable to symmetric instability (section 4.5) and modify the propagation of NIWs in the interior (section 4.6). Understanding the generation and persistence of these PV features can help us understand where these might show up in more realistic simulations or in observations, as well as offer a mechanism for

generating offshelf export or mixing in regions that experience dense overflows.

## 4.5 Symmetric Instability and downslope pulsing on shelf

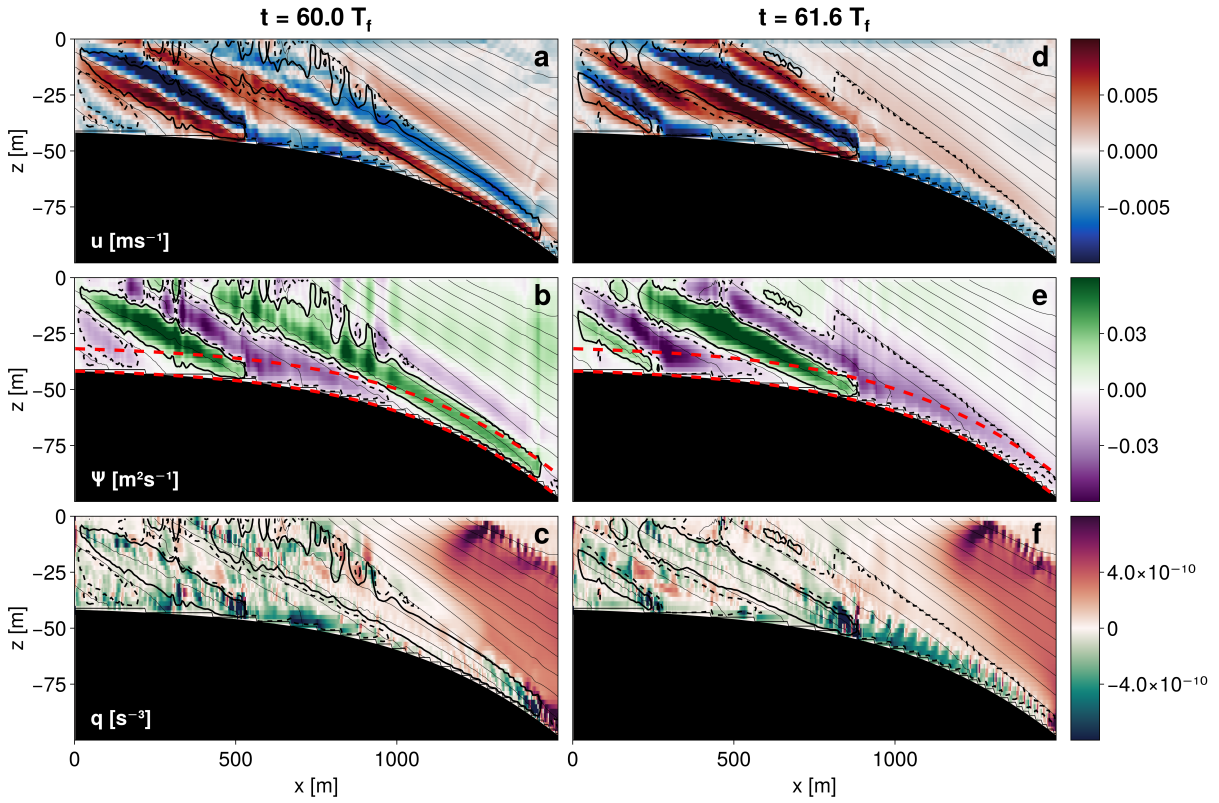



Figure 4.10: Shelf region contours of (a,d) $u$, (b,e) stream function for the flow, and (c,f) PV at two times, $t = 60\,T_f$ and $t = 61.6\,T_f$. Uniformly spaced isopycnal contours are superimposed as thin lines, while clockwise (counter-clockwise) stream function contours are marked with thick dashed (solid) lines. Red dashed contour lines in (b,e) mark the region used in Fig. 4.11. The two snapshots show the across-slope propagation of the SI cells towards the shelf-break front, where the magnitude of the vertical shear is strongest.

After cooling has shut down, the dense overflow gravity current decays, but the shelf remains a dynamically rich region. Here we define the shelf as the first 1000 m with a slanted offshore boundary to avoid the shelf-break front in the following analysis. The shelf based on this definition is outlined and shaded in purple in Fig. 4.5b. The PV on the shelf is strongly

negative from the surface cooling (Fig. 4.10c). These conditions allow for the shelf to be symmetrically unstable and give rise to coherent slantwise convective cells oriented along isopycnals on the shelf, indicative of SI (Haine and Marshall, 1998). We note that, unlike previous work (Yankovsky and Legg, 2019), there is no evidence of SI in the interior, since the PV in the interior stratified layer is entirely positive ($x = 3000 - 6000$, Fig. 4.9b,c) above a thin, Ekman-driven BBL. The overturning structure can be seen in the $u$ velocity and corresponding streamlines, $\Psi$, in Fig. 4.10, where green, $\Psi > 0$, indicates cyclonic rotation. These cells persist throughout the full simulation time after shutdown ($45 - 80\, T_f$), even as the interior flow becomes quieter. The shelf may be susceptible to SI during cooling, as well, but shelf convection and the gravity current make it more difficult to diagnose than the clear signal of slantwise convecting cells seen after shutdown. The cells usually work to quickly bring the PV back to marginal stability (near zero) (Thorpe and Rotuno, 1989; Taylor and Ferrari, 2009; Chor et al., 2022), but the negative PV signature on the shelf is slow to stabilize despite these persistent SI cells. The total volume integrated PV on the shelf after cooling is shut down slowly adjusts to zero PV over the last 30 inertial periods (Fig. 4.5c).

The SI cells propagate slowly offshore in time, contrary to what is often seen in simulations of surface fronts, where the cells are stationary. For instance, in Fig. 4.10b, the first cyclonic cell marked in green is initially spanning $x = 0 - 500$ m. After $1.6\, T_f$, the same SI cell has propagated forward about 250 m (Fig. 4.10e), with a group speed around 0.4 cm s$^{-1}$. This is consistent with theoretical expectations, where slow, across-shelf variation ($x$) of the along-shelf vertical shear ($\partial V/\partial z$) produces SI cell propagation in the across-shelf direction towards the stronger vertical shear (Pedlosky, 2014). This theory predicts that both changes in depth and gradients in PV can affect cell propagation direction (Pedlosky, 2014), but in this area of the

shelf, the topographic slope is small and the gradient is reversed from that seen in other settings (Allen and Newberger, 1996). We have also tested a flat shelf with no depth variation, and still see the cell propagation towards the strong vertical shear, indicating this is the dominant envelope propagation process. Similar across-slope translations of SI cells have been seen in simulations of the Oregon continental shelf and other idealized models (Allen and Newberger, 1996; Brink and Cherian, 2013).

This consistent shelf propagation pattern is clear in the near boundary, vertical average along the slope, delineated in Fig. 4.10b,e by the red dashed lines, plotted over $45\,T_f$ after cooling is shut down in Fig. 4.11. Convergent regions between neighboring SI cells, marked in red in the rotated, along-slope convergence ($-\partial_s U$), propagate towards the shelf break (Fig. 4.11e). Along the bottom, this propagation carries dense shelf waters offshore, with dense pulses reaching the shelf break every 3-5 inertial periods. Buoyancy contours along the shelf bottom show these buoyancy anomalies coinciding with the downslope velocity in rotated, slope-aligned coordinates, $U$ (Fig. 4.11a,b). This pulse is highly dissipative and carries strongly negative PV (Fig. 4.11d,f). Note that the PV and dissipation rate of kinetic energy also show the generation of the high PV wedge after the shelf break, between $x = 1500 - 2000$ m (Fig. 4.11d,f). The lined structure is from the tendrils of high dissipation rate of kinetic energy and high stratification that grow over time in the wedge, as discussed in section 4.3. The structure does not appear to be related to pulsing frequency on the shelf, but the explanation of the exact mechanism is left for future work.

The convergent regions between SI cells are associated with strong bottom PV fluxes, seen in the Hovmöller of the total bottom PV flux, $-\boldsymbol{J} \cdot \hat{n}_{bot}$ along the shelf (Fig. 4.12c), where the energetic transition at the head of the pulses can be seen (bracketed by gray contours) along

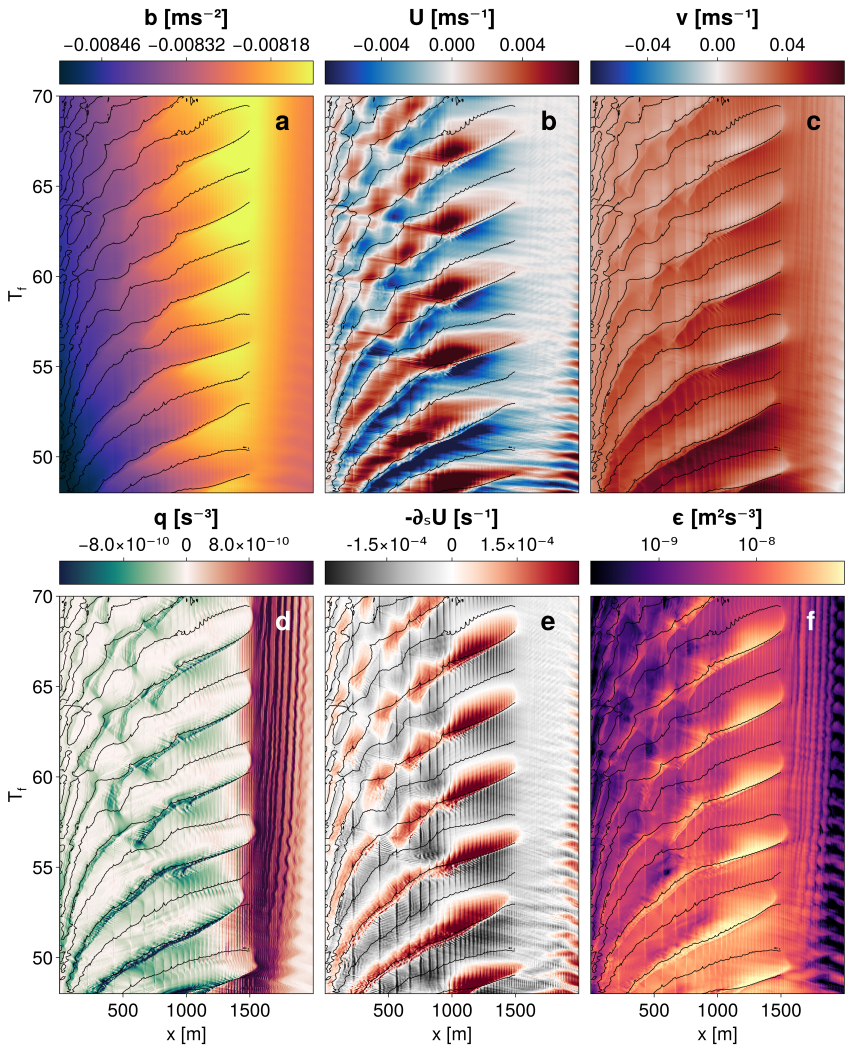



Figure 4.11: Hovmöller plots of (a) buoyancy, (b) rotated across-slope velocity, $U$, (c) along-slope velocity, $v$, (d) PV, (e) across-slope velocity convergence, $-\partial_s U$, where $s$ is the rotated, across-slope coordinate, and (f) the dissipation rate of kinetic energy, $\epsilon$, along the shelf averaged over the bottom 10 m after cooling is shut down, as marked by red dashed lines in Fig. 4.10b,e. Black contours mark the high-pass filtered buoyancy anomaly, $b' = 0$, to denote the passing pulses, stopped before the shelf-break front at $x = 1500$ m.

the transition to the dense, downslope flow (Fig. 4.12a,b). The buoyancy anomaly, $b'$, in Fig. 4.12a is defined with a high-pass Gaussian filter removing trends longer than 6 $T_f$ to exclude the slow evolution of the shelf, highlighting the dense pulses ($b' < 0$). These pulses are strong in magnitude for both components of the PV, defined in (4.11), making the total bottom flux quite

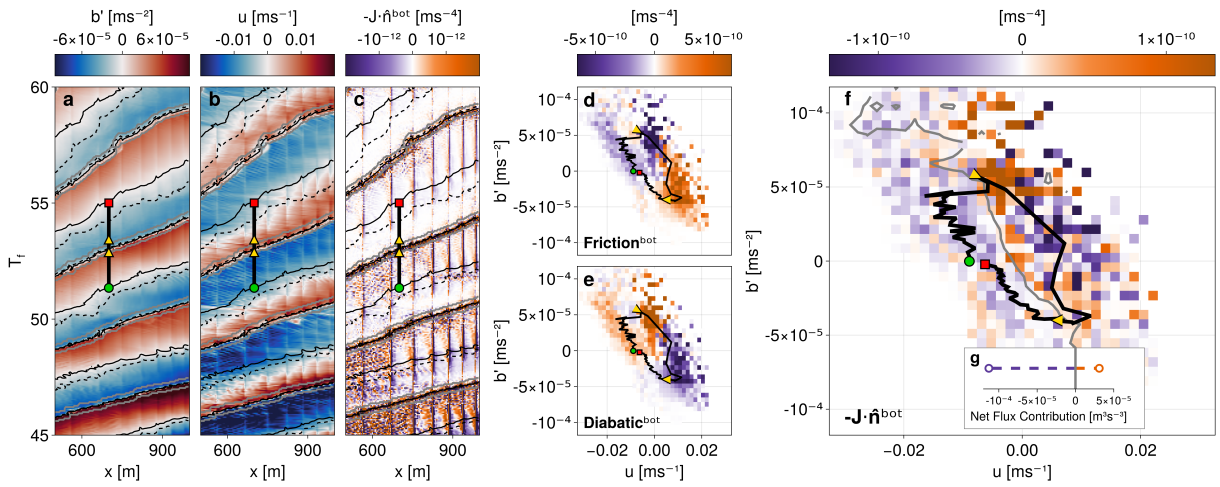



Figure 4.12: Hovmöller plots of (a) across-slope velocity, $u$, (b) buoyancy anomaly, $b'$, based on a Gaussian high-pass filter removing trends longer than $6\,T_f$, and (c) total bottom PV flux along the shelf bottom after cooling is shut down ($45 - 60\,T_f$), before integrating along the bottom boundary (as in Fig. 4.7). The $b' = 0$ (black, solid) and 20th percentile of $b'$ (black, dashed) contours are included on (a-c). 2D histograms of the net (d) friction, (e) diabatic, and (f) total bottom PV fluxes in 2D are binned by $u$ and $b'$ in the region shown in (a,b). A representative trajectory throughout one buoyancy pulse is shown in all plots with a black line, starting at the end of one dense buoyancy anomaly (green circle) and traveling through $u - b'$ space clockwise before reaching the end of the next dense pulse (red square). Yellow arrow markers and a gray contour bracket the highly energetic transition at the head of the dense pulse. The subplot (g) compares the total bottom flux contribution integrated in time and space during the passage of the dense pulse (right of gray contour) and between pulses (left of gray contour).

noisy. To understand the impact of these strong pulses, Fig. 4.12d,e show the joint distribution of the friction and diabatic PV fluxes, respectively, as well as the total (f), of the bottom PV flux based on the across-slope velocity and the buoyancy anomaly. A trajectory through the joint PDFs at a representative location, $x = 700$ m, is shown starting at the end of a dense pulse (green circle), moving clockwise through the energetic flux period at the transition to the dense pulse (between the yellow triangles), and finishing at the end of the next dense pulse (red square). The strong flux magnitudes in (d-f) are found on the right side of the gray demarcating line during the sharp transition as dense pulses propagate through. The same gray contour is shown on the Hovmöllers in Fig. 4.12(a-c), separating the transition at the start of the dense pulse from the rest

of the pulse period. The transition phase at the head of the pulse is dominated by the diabatic term, which first injects PV when the velocity has started to change signs to downslope flow, but the buoyancy anomaly is still positive. The passage of the dense anomaly changes the sign of the diabatic term and subsequently the total bottom PV flux, resulting in compensating short bursts of strong injection/destruction by the bottom PV fluxes.

After the passage of the dense pulse, the PV fluxes are much weaker (left side of the gray demarcation line in Fig. 4.12(d-f). This phase of the bottom flow lasts much longer, though (Fig. 4.12(a-c)). During this time, the total bottom PV fluxes (Fig. 4.12f) are dominated by the friction term (Fig. 4.12d). After cooling is shut down and the system becomes geostrophically adjusted, there is a positive vertical shear along with a positive near-bottom flow ($v > 0$, Fig. 4.11). This is associated with an upslope Ekman transport (MacCready and Rhines, 1991) that follows the bottom boundary, which, in this case, where the dense water is onshore (such that $\partial b/\partial x > 0$), results in a frictional destruction of PV. This matches with the description in section 4.4 and the negative $\text{Fric}^{\text{bot}}$ on the shelf in Fig. 4.7.

While the fluxes are weaker after the passage of the head of the pulse, this phase is longer, and the net bottom PV flux is single-signed compared to the energetic phase of mixed destruction and injection (Fig. 4.12f). It is the long-term PV destruction during the quiescent phase that dominates the net impact of the bottom PV fluxes. The subplot (Fig. 4.12g) shows the total integrated bottom PV flux contribution from the more quiescent (left, purple) and energetic (right, orange) periods of time on the shelf. While the magnitudes of the fluxes are much stronger at the head of the dense pulse phase, the net injection of PV during this period is less than a third of the net destruction that occurs during the rest of the time, largely due to it being so brief in time.

Usually, the appearance of SI and the subsequent convective cells acts to quickly entrain

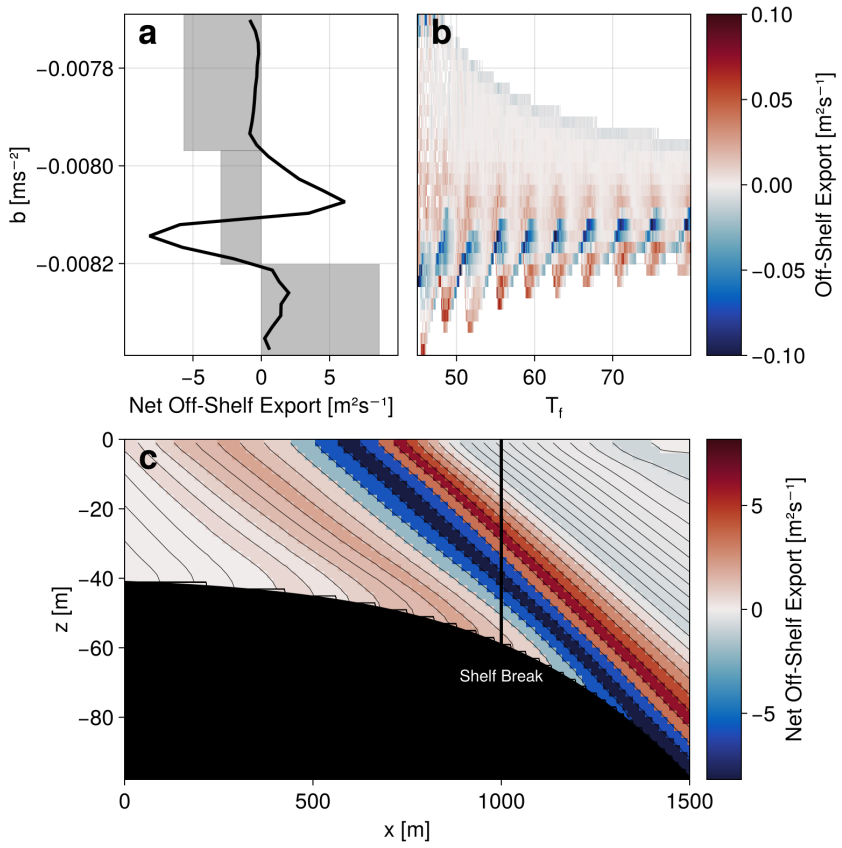



Figure 4.13: Net export off shelf in buoyancy space as defined by the vertical cross section at $x = 1000$ m, shown by the labeled black line in c. (a) the sum over time, after cooling is shut off $(45 - 80\,T_f)$, of the transport across the shelf break, binned in 30 buoyancy bins. The gray bars show the net transport over the buoyancy classes spanned, showing that the export by the densest shelf buoyancy classes is larger than the import/export at the shelf break. (b) buoyancy-binned transport in time, before the sum is taken. (c) net export plotted from (a) in the corresponding buoyancy bin in physical space, using the buoyancy averaged over the same time period as (a,b). Positive values in all plots indicate off-shelf export.

high PV and remove negative PV until the region is stable to SI, with low or zero PV with time scales on the order of an inertial period (Thorpe and Rotuno, 1989; Chor et al., 2022; Taylor and Ferrari, 2009, 2010). While the SI cells are stabilizing the shelf region and bring the PV to zero (Fig. 4.5c), they do so slowly because of the net bottom destruction of PV competing with the more commonly documented injection at the surface (Fig. 4.7c). The negative PV generated by the mean flow between dense pulses is briefly advected along the bottom with the next dense pulse

and then entrained back up the shelf by the cells themselves. This process can be seen in Fig. 4.10c, where negative PV generated along the bottom between $x = 500 - 1000$ m is accumulated and advected along the SI cell's streamline in Fig. 4.10f. This destruction could also be enhanced by the mixing and convergence of these propagating cells at the front, as discussed in 4.4. These processes maintain the net negative PV on the shelf long after cooling is shut down.

The propagation of the SI cells and the associated dense pulses towards the shelf break indicate that these submesoscale instabilities might be an important mechanism for shelf export. Along the shelf bottom, the dense pulses initially propagate at the cell propagation speed, but as the pulse approaches the shelf break where the topography is steeper, these pulses break from the cell and propagate down the slope beyond the region where the cells are located on the shelf (see pulse at $x = 1500$ m, Fig. 4.10a-c). This pulse descends until it reaches a resting buoyancy class near $x = 1500$ m. (This is also the location of the high PV wedge, due to the same resting buoyancy class.) The slope-aligned rotated velocity, $U$, in Fig. 4.11 shows how the velocity of the cell accelerates between $x = 1000 - 1500$ m, a possible indication that the pulse has become a gravity current (Wienkers et al., 2021).

Fig. 4.13 shows the off-shelf export in buoyancy space, defined as the total transport within each buoyancy bin at the "shelf break," located at $x = 1000$ m (as marked in Fig. 4.13c). The offshelf export events are periodic, timed with the dense pulses, which bring the denser buoyancy classes to the shelf break (Fig. 4.13b). The density of the densest buoyancy class is also decreasing with a slow timescale as the shelf region warms, changing the buoyancy class that is experiencing this off-shelf export. By $t = 80\,T_f$, the buoyancy class that was originally part of the import flow above pulses is now the dense buoyancy class being exported. The change in available buoyancy classes on the shelf is tied to these pulsing events, and shows SI can be

a source of subinertial cross-shelf export. To see the net effect of this pulsing process, Fig. 4.13a takes the total transport from each buoyancy class in Fig. 4.13b over the time shown. For more physical intuition, this quantity has also been plotted on the buoyancy field averaged over the same time period in Fig. 4.13c. The dense pulse export is from the lighter red regions, mostly located before the shelf break in (c), below $b = -0.0082$ ms$^{-2}$ in (a). The buoyancy classes along the left edge of the shelf-break front experience much stronger import and export of these lighter buoyancy classes, but in terms of gross export, these competing regions along the front mostly cancel each other out, making the dense water export almost three times stronger than the intermediate buoyancy class import. (See gray bars in Fig. 4.13a for the net export from upper, intermediate, and lower buoyancy classes). The densest buoyancy classes on the shelf, shown in Fig. 4.13c as the first $4$ classes on the left, do not reach the shelf break directly. However, SI-driven mixing partially lightens this dense shelf water, transferring it into warmer buoyancy classes that can be advected past the shelf break and exported offshore. By the end of the simulation, these buoyancy classes no longer exist on the shelf, indicating this water-mass transformation. In larger-scale models where SI is parametrized, the models produce significantly greater off-shelf transport than simulations without it (Yankovsky et al., 2021). This periodic pulsing process highlights one mechanism that could be contributing to this correlation between SI and shelf transport.

In summary, after the surface cooling is shut down, the shelf region remains dynamically active due to persistent SI, driven by strongly negative PV. The resulting slantwise convective cells propagate toward the shelf-break front following the gradient in vertical shear, generating subinertial dense pulses that transport negative PV and dense water downslope. While these pulses produce energetic bursts of bottom PV flux as they propagate, the net bottom PV budget

is dominated by weaker frictional destruction during the longer quieter phases between pulses, due to upslope Ekman transport. This continuous bottom destruction of PV, combined with re-entrainment by the SI cells themselves, maintains negative PV on the shelf, slowing the stabilization process. Though these SI cells might be inefficient in reducing the negative PV, they play a crucial role in shelf export. Dense pulses that reach the steepening topography near the shelf break detach from the cells and descend the slope, producing periodic off-shelf transport that exports nearly three times more dense water than is imported at intermediate buoyancy classes, demonstrating significant water-mass transformation on the shelf due to SI.

## 4.6 Modification of NIWs by background dense overflow

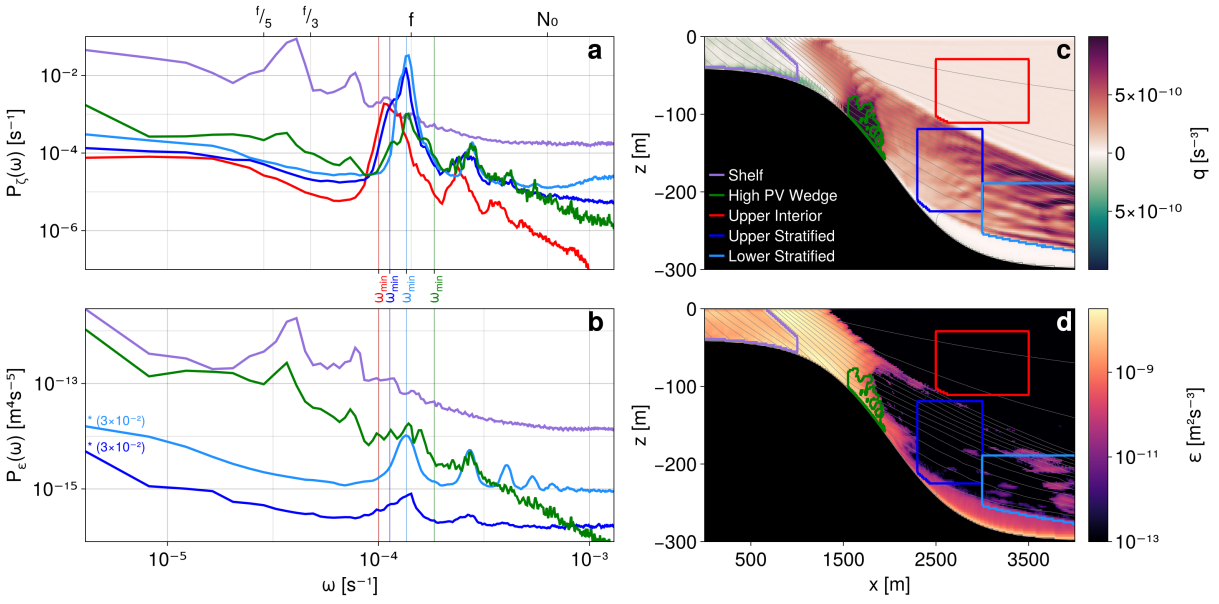



Figure 4.14: Power spectra of (a) vertical vorticity and (b) dissipation rate of kinetic energy taken over different regions of interest. The colors of the lines in the spectra match the color of the regions they represent (see legend for naming conventions), marked in the post-cooling, inertially averaged plot of (c) minimum wave frequency normalized by $f$ and (d) dissipation of kinetic energy rate.

The dense overflow creates a rich internal wave field (Fig. 4.15c,d), which persists after cooling shuts down, modified by the resulting features of high PV and sloping isopycnals along the shelf from the overflow. Internal waves near the inertial frequency (NIWs) are known to interact strongly with balanced flow features, possibly causing enhanced dissipation and mixing (Mooers, 1975; Kunze, 1985; Whitt and Thomas, 2013). Assuming waves propagating only in $(x, z)$, with a mean background flow, $V$, and mean stratification $N^2$ the dispersion relation is given by

$$\omega^2 = \alpha^2 N^2 + f(f + \frac{\partial V}{\partial x}) - 2f\frac{\partial V}{\partial z}\alpha, \tag{4.12}$$

where $\alpha = k/m$ is the aspect ratio of the wave (Whitt and Thomas, 2013). [1] The minimum wave frequency is given by the frequency of waves propagating along isopycnals, ($\alpha_{min} = \frac{M^2}{N^2} = s_b$) (Whitt and Thomas, 2013), which can be written in terms of the mean PV of the background flow, $\bar{q}$,

$$\omega^2_{\text{min}} = f\bar{q}/N^2, \tag{4.13}$$

(Whitt and Thomas, 2013). In regions where PV is enhanced, the minimum allowable frequency is superinertial, reducing the permissible frequency range for waves (Whitt and Thomas, 2013). Trapping and reflection of these waves as they propagate towards regions with a higher minimum frequency than their own can drive enhanced dissipation and mixing in this region (Whitt and Thomas, 2013; Qu et al., 2021b).

The waves generated by the dense overflow are within the near-inertial end of the wave frequency spectrum. Power spectra were taken at all points in the regions marked on in Fig.

[1] The use of $\omega$ for wave frequency and $\alpha$ for the wave aspect ratio differ from the definitions and variables previously used in Chapters 2 and 3 to match the notation in (Whitt and Thomas, 2013).

4.14c,d and then averaged. The labels in the legend in Fig. 4.14c will be used to discuss the spectra results from those regions. The power spectra of the vertical vorticity (Fig. 4.14a) indicate that the waves in the upper interior have subinertial frequencies, with a peak around $0.74f$, indicative of the lowered minimum frequency in the upper interior, with an average value marked by the corresponding vertical line in Fig. 4.14a,b. The upper and lower stratified regions have frequencies closer to inertial with peaks between $0.94$ and $1f$. Banded shear and PV within the interior stratified layer have been found in other dense overflow simulations, but were attributed to SI due to thin negative PV bands found in the region (Yankovsky and Legg, 2019). In this simulation, the interior stratified layer is stable to SI (Fig. 4.14c) because of the current-generated injection of PV advected down the slope during the stratified layer creation (see section 4.4). The near-inertial frequency peak in the spectra shows these banded signatures can be attributed to propagating NIWs instead (Fig. 4.14a). The dominant vertical wavelength of the waves in the interior stratified layer is approximately $16$ m, which is well resolved at the baseline grid spacing of $\Delta z = 2$ m (Arbic et al., 2010; Remmler et al., 2015). Moreover, a companion run with doubled horizontal and vertical resolution confirms the robustness of the inertial-frequency peaks presented here.

The peak on the shelf region in Fig. 4.14a matches the subinertial frequency of the dense pulses and corresponding behavior discussed in section 4.5. Waves propagating along isopycnals, at the minimum frequency, will not be able to propagate onto the shelf, where the mean PV remains negative after cooling is shut down. Therefore, the following analysis will focus on waves propagating in the interior, as the bulk of the interior wave field is close to the minimum frequency (Fig. 4.14a). The high PV wedge at the shelf break after cooling shuts down, and the slope-aligned isopycnals and high PV capping in the interior stratified layer (Fig. 4.14c)

modify the propagation of NIWs, resulting in different patterns of wave trapping, breaking, and reflection.

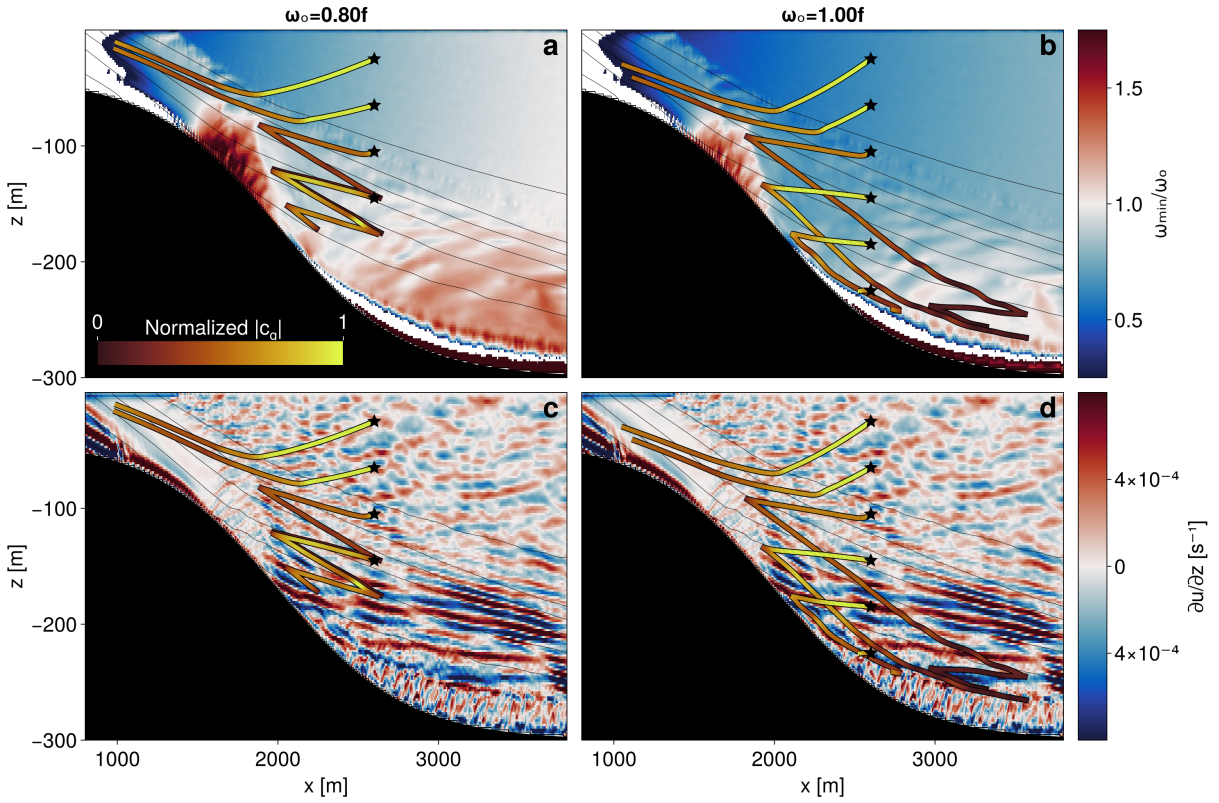



Figure 4.15: Ray tracing at two different frequencies $\omega = 0.8\,f$ (a,c) and $f$ (b,d) starting at initial locations given by the black stars, are shown over a background given by (a,b) the ratio of the minimum frequency to the ray frequency, averaged over $50 - 70\,T_f$. Red regions where the minimum frequency is higher than the ray's indicate how the background flow can modify the propagation of NIWs. (c,d) a snapshot of vertical shear at $t = 70\,T_f$, with weakened magnitudes in the high PV wedge, indicating the agreement of ray tracing to the true wave propagation. The color of the ray is given by the normalized group velocity of that ray.

After achieving a quasi-steady background flow (once cooling has been shut off), the theoretical path along which NIW energy would propagate through the domain can be modelled using the group velocity of the wave. The rays of energy propagation for a given initial condition can

be found using ODE solvers on the slope of the wave characteristics, $\lambda$,

$$\frac{dz^r}{dx^r} = \lambda = s_b \pm \sqrt{\frac{\omega^2 - \omega_{\min}^2}{N^2}} \tag{4.14}$$

where $s_b$ is the slope of the isopycnals and ($x^r$,$z^r$) is the location of the ray (Whitt and Thomas, 2013; Qu et al., 2021b). Ray tracing for two representative wave frequencies, $\omega_0 = 0.8, 1.0f$, is shown in Fig.4.15, with initial locations (black stars) chosen to span the depth of the simulation.

Rays originating from the more weakly stratified upper interior with either frequency initially propagate downward along the lower characteristic, in the negative $z$ direction, but quickly bend upwards, following the strongly stratified isopycnals along the topography. Across-slope velocity shear bands from the waves generated in this region show the bending of these incoming NIWs as they encounter the shelf-break front (Fig. 4.15c,d). Before the high PV wedge has extended above the shelf ($50 - 70T_f$), these waves propagate into the shelf-break front. The waves slow down as they turn and converge, but encounter negative PV on the shelf well before the group velocity approaches $0$. Though similar in behavior or shape to slantwise critical layers (Qu et al., 2021b), these waves are entering a region where the minimum frequency is decreasing, on the way to becoming a complex-valued growth rate. Therefore, this is not a slantwise critical layer. Due to the negative PV and strong ageostrophic across-slope flow in the shelf region (Fig. 4.8g,j), the fate of the upper rays cannot be confirmed from ray tracing.

Subinertial rays originating from the region of slope-aligned isopycnals exhibit upward propagation ($\lambda > 0$), from the ray characteristic that would typically propagate downward ($m > 0$) under classical linear theory without flow modifications (Fig. 4.15a,c). This counterintuitive upward trajectory results from the steep slope of the isopcynals, which alters the ray

path geometry compared to the case with no mean flow ((4.14), Whitt and Thomas, 2013). Upon encountering the high PV wedge, which abruptly increases the minimum frequency, the upward-propagating rays reflect off the wedge itself (where $\omega_{\min}$ is superinertial) and are funneled down toward the interior bottom boundary (Fig. 4.15a,c). The vertical growth of the high PV wedge over time blocks the subinertial waves, seen in the greatly reduced across-slope shear compared to the banded wave structures in the stratified interior (Fig. 4.15c,d) and increased dissipation rate of kinetic energy (Fig. 4.4c). The high PV wedge vorticity spectrum shows a similar peak in the same near-inertial range as the interior (Fig. 4.14a, $\omega = 0.94f$), but this spectral peak is below the minimum allowable frequency in this region. Therefore, this signature is most likely an evanescent disturbance, pulsing at a similar frequency as a remnant of the waves propagating towards and reflecting off of this region. The ray reflection patterns, increased dissipation, and weakened wave presence near the high PV wedge suggest these waves most likely break or reflect off the strengthening high PV wedge with an expectation of enhanced mixing and energy dissipation in the lower regions of the domain.

To understand the impact of these breaking events in the interior, the dissipation rate of kinetic energy spectra for each region is also shown in Fig. 4.14b. Since the interior regions have much lower dissipation rates than the shelf and high PV wedge, the stratified region spectra have been multiplied by $300\ \mathrm{s}^{-1}$ for visualization purposes. The upper interior had even weaker dissipation rates, with no discernible peaks, and so has been left out of the dissipation plot for clarity. This weaker interior magnitude is expected as the waves generated during the dense overflow quickly weaken after cooling is shut down (Fig. 4.3a,f). The decaying internal waves generated by the dense overflow are used here as a proxy for the full internal wave field that would be present along dense overflow pathways (Voet et al., 2024; Kunze et al., 2023; Alford et al.,

2016). While the magnitudes of the power spectra for dissipation of kinetic energy rate in the interior are relatively weaker than on the shelf, the peaks are still useful indicators of processes that might generate more turbulence in a more realistic and energetic background wave field.

The subinertial vorticity peak in the upper stratified region in Fig. 4.14a, representing the region where these rays are reflected and funneled down, is aligned with a peak in the dissipation rate of kinetic energy in its own spectra as well as one in the high PV wedge (Fig. 4.14b). The frequency peak in the dissipation rate of kinetic energy in the upper stratified region ranges from the minimum allowable frequency in this region to the new superinertial minimum allowable frequency in the PV wedge (Fig. 4.14b), indicating it may be the transition to a higher minimum frequency causing the increased breaking of the subinertial interior waves.

Rays initialized in the same region, but with a higher frequency of $\omega_0 = f$ (Fig. 4.15b,d), also propagate towards the high PV wedge, reflecting down into the interior towards the bottom boundary. These waves are allowed to propagate further away due to their higher frequency compared to the local minimum. Initially spaced $40$ m apart, the rays converge after reflection, aligning with the isopycnals that run parallel to the bottom boundary. As their frequency approaches $\omega_{\min}$, their group velocity tends to zero, trapping and amplifying the waves in a slantwise critical layer, where increased mixing and dissipation are expected (Qu et al., 2021b,a). Some enhanced dissipation of kinetic energy rate can be seen in this region in the inertially averaged $\epsilon$ in Fig. 4.14d. The lower stratified region spectra also show an inertial peak in the dissipation rate of kinetic energy and the vorticity (Fig. 4.14b). The peaks in dissipation rates found in these highly stratified regions suggest the induced breaking and trapping will result in efficient mixing. The higher harmonic peaks in this spectrum, as well as the high PV region and the upper interior vorticity spectra, could be indicative of wave-wave interactions generated by NIWS that either

break or radiate away. The reflection and convergence into a slantwise critical layer seen here is very similar to the behavior found in realistic and idealized simulations of NIWs along the Texas-Louisiana shelf for the case of topography-aligned isopycnals induced by Ekman arrest (Qu et al., 2021a). While the mechanism for generating the background flow structure and baroclinicity is different, the resulting slantwise critical layer could still result in enhanced breaking and mixing.

## 4.7 Discussion

High-resolution ($\sim 1/10°$) eddy-resolving ocean models can capture the broad geometry and pathways of dense overflows and deep western boundary currents, but they do not resolve the small vertical scales and boundary-layer processes that control bottom PV fluxes and the associated interactions with resulting PV anomalies (e.g., Maltrud and McClean, 2005; Legg and Klymak, 2008; Colombo et al., 2020; Danabasoglu et al., 2010). Our analysis suggests that PV injection by the gravity current impinging along the shelf break during cooling, and PV destruction on the shelf from upslope Ekman transport after cooling ceases, can significantly impact NIW-driven mixing, as well as the longevity of SI and associated across-shelf transport. A better understanding of how the presence of PV structures generated by dense overflow or found near dense overflow pathways modifies NIWs and SI will enable more accurate quantification of energy exchange, mixing, and transport in global ocean models.

The topography-aligned isopycnals and elevated PV injected by the dense overflow establish a background state favorable for both trapping and breaking of NIWs within the stratified interior (Figs. 4.14,4.15). Previous studies in larger-scale, realistic models have documented internal wave generation by dense overflows, finding that a proper representation of the internal

wave field requires non-hydrostatic simulations, but the inertial frequency band was not examined in detail (Magaldi and Haine, 2015). In the present idealized configuration, the overflow generated its own NIW field, which was used for the analysis in section 4.6. In reality, overflow regions often experience frequent storms that generate energetic NIWs, further supplemented by semidiurnal tidal energy, which lies near the inertial frequency in the North Atlantic (Alford et al., 2016; Kunze et al., 2023; Voet et al., 2024). Thus, the waves examined here should be considered a proxy for the stronger NIW fields typically present in overflow regions. Observed spectral peaks in dissipation (Fig. 4.14b) indicate that reflection off high-PV regions and trapping within slantwise critical layers can substantially enhance wave breaking along dense overflow pathways and deep western boundary currents, consistent with prior studies which also find intensified mixing in these regions (Qu et al., 2021b, 2022). While a more realistic incident wave field would be required to estimate absolute dissipation rates and quantify water mass transformation, the enhanced dissipation associated with NIW breaking and trapping near strongly stratified bottom boundaries could guide future parametrizations of mixing along overflow pathways.

The banded velocity features observed in the stratified interior (Fig. 4.14c,d) have previously been attributed to SI in similar overflow configurations (Yankovsky and Legg, 2019). Here, because the interior region is symmetrically stable, we considered an alternative interpretation in which NIWs interact with the background state. Variations in bottom injection and destruction of PV have been linked to current speed and topographic structure (Gula et al., 2015; Benthuysen and Thomas, 2012; Falcini and Salusti, 2015). Therefore, negative PV anomalies in the lower stratified region in other simulations may reflect differences in the structure, speed, or pulsing frequency of gravity currents impinging on the shelf break, which set the scale of PV injection. This work has also shown that an accurate representation of the BBL and its interaction with

the gravity current is likely important for obtaining a reliable interior PV signature. In coarser models, such regions may be misclassified as SI-dominated if parameterizations rely solely on local PV thresholds (Yankovsky et al., 2021), potentially underestimating the role of propagating NIWs and the associated dissipation and mixing.

While the NIW field was shown here to be an active contributor to kinetic energy dissipation, the strong shear and lateral buoyancy gradients found in dense overflow regions still suggest SI can be important for efficiently converting geostrophic shear into dissipation (Magaldi and Haine, 2015; Ruan et al., 2017; Garabato et al., 2019; Beaird et al., 2013; Wenegrat and Thomas, 2020; Thomas et al., 2013; Benthuysen and Thomas, 2012). Some eddy-resolving models may occasionally exhibit SI-like overturning, but the resulting energy conversion and diapycnal mixing are often underestimated, necessitating parametrization (Jiang et al., 2022; Yankovsky et al., 2021; Bachman and Taylor, 2014; Chor et al., 2022). Regional SI parameterizations have been shown to influence not only mixing but also cross-shelf exchange (Jiang et al., 2022; Yankovsky et al., 2021). In the present simulations, dense water is transported by convergent regions between SI cells as they propagate towards the shelf break, providing a potential explanation for the enhanced cross-shelf exchange.

Notably, SI — and therefore dense-water export — persists for the duration of the simulation after cooling ends ($40\,T_f$), due to continued bottom PV destruction by upslope Ekman transport, which reduces the efficiency of SI cells at restoring marginal stability. Eddy-resolving models can capture broad overflow pathways but cannot represent the sustained low-PV conditions necessary for prolonged SI-driven transport. Hence, SI persistence and its impact on KE dissipation and off-shelf export should be included in SI parametrizations. While previous studies argued that bottom Ekman transport plays a limited role in shelf export (Klinck and Dinniman,

2010), our results demonstrate that accurately parameterizing the duration of propagating SI cells and the resulting off-shelf export requires accounting for bottom PV destruction by bottom Ekman transport. Importantly, the diagnostics required, such as bottom stress and stratification, are typically available in larger-scale models (Berntsen et al., 2018; Colombo et al., 2020; Yankovsky et al., 2021; Klinck and Dinniman, 2010), suggesting that SI parameterizations could be improved by incorporating the continued PV destruction by bottom Ekman transport that controls SI persistence. In energetics-based SI parametrizations (Bachman et al., 2017), kinetic energy is extracted from fronts at rates consistent with resolved SI (Wenegrat and Thomas, 2020), without explicit reliance on SI slumping timescales as in PV-based formulations. While this approach has been shown to capture SI-driven restratification and dissipation (Bachman et al., 2017), its implications for tracer fluxes and sustained dense-water export, particularly in boundary-influenced settings, remain less well constrained. Incorporating even a simple representation of Ekman-driven PV destruction into existing PV-based schemes (Yankovsky et al., 2021), or further evaluating the ability of energetics-based parameterizations to capture off-shelf export in boundary-driven regimes, could help bridge the gap between small-scale physics and realistic estimates of dense off-shelf transport in coarser models.

Taken together, these results highlight the importance of bottom PV fluxes in controlling both the SI longevity on the shelf and NIW interactions with dense overflow pathways. By modifying the background stratification and PV structure, dense overflows create conditions that favor sustained SI-driven transport of dense water off the shelf and enhanced NIW dissipation in strongly stratified layers adjacent to the boundary. These mechanisms provide a physically grounded link between small-scale boundary processes and larger-scale mixing and transformation along deep western boundary currents, underscoring the need for parameterizations that

account for mean-flow interactions with SI and NIWs.

## 4.8 Conclusion

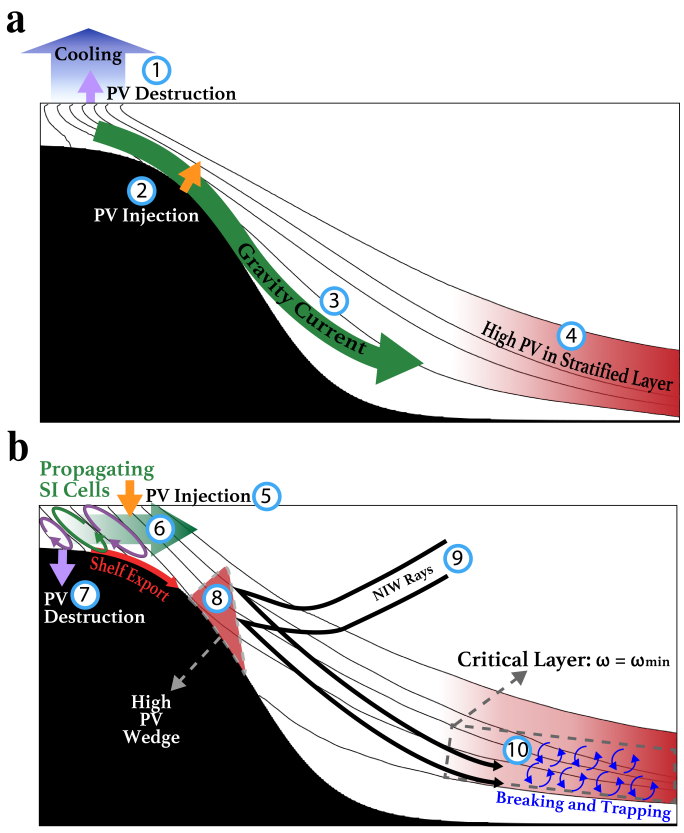



Figure 4.16: Schematic of dense overflow processes (a) during cooling and (b) after cooling is shut down. Numbers in blue circles will be used to reference different regions and processes.

A three-dimensional LES was used to examine how submesoscale dynamics and their interaction with NIWs modify and are modified by flow in the pathway of dense overflows through PV boundary fluxes. The schematic in Fig. 4.16 integrates the key elements discussed in this work that will be summarized below. Different regions and processes will be referenced using the numbers marked by blue circles.

The simulated overflow exhibited behavior consistent with observational and numerical

studies of dense overflows (Yankovsky and Legg, 2019; Gawarkiewicz and Chapman, 1995; Beaird et al., 2013; Lin et al., 2020; Girton et al., 2001; Muench and Gordon, 1995). Surface cooling generated gravitationally unstable shelf water that cascaded downslope and equilibrated at depth, forming a region of negative along-slope flow ($v < 0$), with a compensating return flow at the surface ($v > 0$) as seen in previous work (Gawarkiewicz and Chapman, 1995; Yankovsky and Legg, 2019) (Fig. 4.8a,b). Diabatic PV destruction from the surface cooling resulted in a negative PV anomaly on the shelf (Fig. 4.16a, region 1). Large subinertial dense pulses, formed during cooling, flowed down the topography in the form of gravity currents (Fig. 4.16a, region 3), which generated a frictional PV injection where they impinged along the shelf break (Fig. 4.16a, region 2). This PV was advected along the bottom topography and persisted as layered structures within the stratified interior for the duration of the simulation (Fig. 4.16a, region 4).

Due to the destruction of PV by the surface cooling (Fig. 4.16a, region 1), the shelf was susceptible to SI. After cooling was shut down, the resulting SI cells propagated towards the shelf break (Fig. 4.16b, region 6) due to the strong gradient in the vertical shear (Pedlosky, 2014). Convergent regions between cells episodically transported dense water in subinertial pulses across the slope (Fig. 4.16b, region 6). As these pulses reach the shelf break, they detach from the cell structures and descend along the slope, exporting water from the densest buoyancy classes off the shelf (Fig. 4.13). Periodic dense pulses on the order of a few days in realistic simulations and observations have mostly been attributed to mesoscale variability and seasonal changes in overflow waters upstream (Almansi et al., 2017; Girton and Sanford, 2003; von Appen et al., 2014), but here we offer a submesoscale-driven transport process.

This export of dense water was particularly effective due to the persistence of the SI on the shelf long after cooling had been shut off ($\sim 40\, T_f$). The shelf never fully returned to marginal

stability over the course of the simulation (Fig. 4.5c). Intermittent PV injection from dense pulses was outweighed by a continual frictional destruction associated with upslope Ekman transport between pulses (Fig. 4.16b, region 7), enabling ongoing SI and a slower net PV injection rate on the shelf. These results demonstrate that SI can actively support off-shelf export in dense overflows, providing a mechanistic pathway that complements previous findings of SI-prone overflow environments (Magaldi et al., 2011; Yankovsky et al., 2021; Goldsworth et al., 2024; Zhou et al., 2022; Allen and Newberger, 1996).

After cooling ceased, frontal adjustment produced rapid surface PV injection at the top of the shelf-break front (Fig.4.16b, region 5), forming a high-PV wedge along the bottom just past the shelf break, at the resting buoyancy class from the surface generation (Fig. 4.16b, region 8). The increase in PV in this feature over time could be due to continued frictional injection at the surface or from the diabatic flux associated with the upslope return flow along topography just after the shelf break (Fig. 4.7c). The mechanism for the organization of this feature into highly stratified tendrils (Fig. 4.4b), innermixed with increased dissipation of kinetic energy rate (Fig. 4.4c), is left for future work, though it is likely related to the propagation and reflection of incoming NIWs. Due to the injections of positive PV during cooling by the gravity current (Fig. 4.16a, regions 2,4) and post-cooling near the shelf break front (Fig. 4.16b, region 5), the interior PV is positive, barring a small mixed BBL under the interior stratified layer along the slope (Fig. 4.8d,j). Therefore, the only regions clearly susceptible to SI were above the shelf break.

Within the overflow interior, the flow generated internal waves with near- and sub-inertial frequencies (Fig.4.16b, region 9). Sloping isopycnals guided NIWs towards the high PV wedge, where wave reflection and possible breaking occurred off the wedge itself (Fig.4.16b, region 8), due to the associated increase in the minimum allowable wave frequency (Whitt and Thomas,

2013). Ray-tracing suggests the reflected waves propagated downward, encountering a slantwise critical layer, where isopycnals are aligned with topography (Fig. 4.16b, region 10). As NIWs propagate into a critical layer, their group velocity approaches zero, and they are trapped and amplified (Qu et al., 2021b). Spectral analysis shows enhanced dissipation of kinetic energy rate in the regions associated with slantwise critical layers and reflection at near-inertial frequencies, indicating breaking and possible mixing (Fig. 4.14b). This mechanism suggests that NIW reflection and critical-layer trapping along dense overflows may enhance diapycnal mixing at depth, with potential consequences for water-mass transformation, tracer distribution, and large-scale circulation.

Incorporating realistic near-inertial forcing and quantifying water-mass transformation associated with NIW trapping and breaking along topography would help identify where NIW–mean flow interactions most strongly enhance mixing and exchange. A more extensive investigation of these interactions could also clarify the mechanism behind the growth of the small banded features in the high-PV wedge at the shelf break (Fig. 4.4). The present domain width is much smaller than the Rossby deformation radius, limiting the formation of baroclinic eddies, which are often a dominant driver in dense overflows (Yankovsky and Legg, 2019; Magaldi et al., 2011; Cenedese et al., 2004; Whitehead et al., 1990; Smith, 1976). Expanding the shelf and domain in more realistic simulations could generate regions unstable to SI while permitting eddy activity near the shelf-break front, potentially altering the persistence and efficiency of SI in cross-shelf export. Future work that couples these dynamics with observations and improved large-scale parameterizations will help resolve their broader significance to global circulation and the climate. Results presented here have demonstrated that SI and NIW–mean flow interactions can substantially modify dense overflow dynamics by enhancing off-shelf export and local dissipa-

tion, potentially increasing bottom mixing and contributing to deep-water transformation.

# Chapter 5: Conclusion

The results presented in this work advance our understanding of mixing, momentum, and buoyancy exchange in turbulent bottom boundary layers (BBLs) over sloping topography, processes that play a central role in the global overturning circulation (Lumpkin and Speer, 2007; Ferrari, 2014; Ferrari et al., 2016; Laurent et al., 2001) as well as in the near-boundary exchange of nutrients, gases, or sediments (Toggweiler et al., 1989; Friedrich et al., 2011; Walin, 1982). While bottom-enhanced mixing primarily drives diapycnal sinking in the ocean interior, recent studies suggest the necessary upwelling may occur through small-scale mixing within turbulent BBLs along slopes (Ferrari et al., 2016; Mashayek et al., 2017; Holmes and McDougall, 2020). The search for this "upside-down mixing" has motivated observational campaigns observational campaigns and numerical studies aimed at identifying the mechanisms that enable mixing and efficient diapycnal exchange along topography (e.g., Wynne-Cattanach et al., 2024; Garabato et al., 2019; Wenegrat et al., 2018; Wenegrat and Thomas, 2020; Holmes et al., 2019; Qu et al., 2021b,a). In parallel, near-topographic mixing and exchange in dense overflow regions transform water masses as they descend, influencing the properties of waters that must later upwell in the deep ocean. This study has shown how multiple processes, including internal tides breaking along slopes (Chapter 3), near-inertial waves (NIWs) interacting with benthic fronts, and symmetric instability (SI) (Chapter 4), can drive turbulence, restratification, and cross-slope or

boundary-interior exchange.

Since topography underlies all the processes examined in this work, validating the grid-fitted IBM in Oceananigans was essential. Chapter 2 showed that the IBM captures laminar, turbulent, and stratified Ekman flows over slopes, with consistent boundary-layer scales and transports across topographic resolutions. Building on this foundation, upslope Ekman flow, where transport impinges directly on vertical step faces, could further test the method's robustness and its sensitivity to grid coarseness. Although the present results revealed only minor differences, mostly in the onset of 2D turbulence, fully three-dimensional simulations will be required to determine how vortical structures and turbulent statistics depend on the immersed topographic representation. Quantifying changes in mixing efficiency using diagnostics such as available potential energy (Winters et al., 1995) would also provide a more direct measure of how discretization affects irreversible mixing.

Chapter 3 demonstrated, using three-dimensional LES, that internal wave breaking on sloping topography drives near-boundary overturns and along-isopycnal intrusions. The effective wave height, representing the ratio of wave velocity to initial stratification, governed overturn scale, the resulting kinetic energy dissipation, and the average thickness of interior ejections, linking turbulent boundary-layer processes to interior water-mass exchanges (Whitley and Wenegrat, 2025). While mean vertical buoyancy fluxes suggest "upside-down" mixing, inclusion of lateral fluxes reveals that the near-boundary region experiences a net buoyancy flux divergence (Whitley and Wenegrat, 2025). However, short, intense bursts of mixing at the phase transition to the downslope flow produced net diapycnal transport into intermediate buoyancy classes. The upslope bore at the beginning of the next phase then restratified the boundary region for the next mixing phase, emphasizing the importance of phase-dependent variability in combination with

time-averaged measures for understanding this efficient water-mass transformation.

Chapter 4 examined dense overflows in three-dimensional LES, where SI and NIWs interacted with the mean flow and stratification to drive subinertial dense-pulse export, modify potential vorticity (PV), and possibly enhance near-topography mixing. Surface cooling generated downslope dense flow and along-slope geostrophic currents that transported high-PV fluid, injected along the topography, into the interior stratified layer. Banded shear features previously attributed to SI (Yankovsky and Legg, 2019) were revealed instead as near- and sub-inertial internal waves. Their reflection off the high-PV wedge at the shelf break and trapping within slantwise critical layers likely promoted wave breaking and enhanced diapycnal mixing. SI did occur on the shelf, where frictional effects maintained negative PV and enabled long-term cross-shelf export of dense water by convergent regions between propagating SI cells. Together, these results show that SI and NIW–mean-flow interactions can substantially influence off-shelf transport, local dissipation, and potentially water-mass transformation.

More broadly, the results of this dissertation highlight a persistent gap between the scales at which boundary-layer mixing and exchange are generated and the scales at which their consequences are represented in ocean and climate models. Turbulent BBL mixing driven by internal waves and submesoscale instabilities occurs on vertical and horizontal scales that are typically unresolved, yet these processes directly influence water-mass transformation, heat transport, and the pathways of the overturning circulation (Wunsch and Ferrari, 2004; Melet et al., 2016; Magaldi and Haine, 2015; Legg et al., 2009). Addressing this mismatch will require coordinated advances in downscaling strategies and process-aware parameterizations. One promising direction is the targeted use of high-resolution nested models in key overflow and slope regions, forced by realistic large-scale simulations, to directly diagnose bottom potential vorticity fluxes, diapy-

cnal exchange, and dissipation in more realistic global settings (Chen et al., 2025; Dong et al., 2022; Gula et al., 2016a). These simulations can then be used to derive empirically grounded closures that relate resolved quantities, such as along-slope velocity, stratification, and internal-wave shear, to boundary PV tendencies, mixing rates, and boundary–interior exchange in coarse-resolution models.

Current parameterizations of internal wave–driven mixing and SI in global and large-scale ocean models rely on idealized assumptions about energy sources, boundary interactions, and isolated mechanisms, limiting their ability to represent the intermittent, topographically- or mean flow-influenced processes that dominate stratified BBLs (Melet et al., 2016; Alford et al., 2016; Yankovsky et al., 2021). Internal wave parameterizations commonly assume fixed fractions of wind or tidal energy, which can underestimate mixing associated with internal waves breaking on topography far from generation sites or with interactions between NIWs and mean flow features (Melet et al., 2016; Alford et al., 2016; Whalen et al., 2020). Spatially varying diffusivity maps informed by observations have been used to compensate for less-canonical methods of wave mixing, but such embedded approaches may not remain robust under changing climate conditions (Jochum, 2009; Nielsen et al., 2018). The work presented here clarifies how NIWs can induce mixing in key transport pathways of the global circulation and calls for physically motivated parameterizations that account for both the evolution of PV along topography by gravity currents and the subsequent mean-flow modifications by NIWs. Similarly, the persistence of SI was shown to depend on bottom PV fluxes from Ekman transport (Chapter 4). Extending SI parameterizations to account for prolonged slumping time scales due to Ekman transport could improve estimates of SI-driven export near overflow pathways and enhance predictions of how these transports may change in a warming climate. Consequently, these findings necessi-

tate building parameterizations that explicitly link evolving mean-flow structure and topographic interactions to internal wave- and instability-driven mixing.

Looking ahead, a central challenge for the oceanographic community is to quantify how near-topographic mixing and exchange feed back onto climate-relevant tracers, including heat, oxygen, carbon, and nutrients. The ocean has absorbed the vast majority of excess planetary heat over recent decades (Riser et al., 2016) and approximately a quarter of anthropogenic carbon emissions (Friedlingstein et al., 2022), underscoring the need for accurate representations of boundary-confined mixing and transport that regulate exchanges between the surface, abyss, and interior. Progress will require tighter integration of dynamical BBL studies with biogeochemical modeling, alongside expanded observations in the deep ocean, particularly near complex topography. Platforms such as Deep Argo floats, autonomous microstructure measurements, and improved velocity and stratification sensing near the seafloor offer an opportunity to directly constrain both the bathymetry and the processes explored here (Racapé et al., 2019; Zilberman et al., 2025; Spingys et al., 2021). At the same time, increasing computational resources and the growing use of non-hydrostatic ocean models in climate applications will enable more faithful simulations of internal-wave breaking, dense overflow dynamics, and instability-driven transport (Magaldi and Haine, 2015; Bellafiore et al., 2018; Kanarska et al., 2007; Óscar Álvarez et al., 2019). Continued development of modeling frameworks in modern computing languages, such as Julia and Python, will further facilitate flexible, efficient exploration of these processes and their extension to biogeochemical tracers across model scales (Wagner et al., 2025a; Strong-Wright et al., 2023). In combination, these observational and modeling advances provide a framework for translating process-level understanding of near-boundary mixing into constraints on global budgets and circulation.

By employing high-resolution, idealized LES with a grid-fitted IBM, this work has provided a detailed view of how topography, internal waves, submesoscale motions, and mean flows interact to shape BBL dynamics. The results emphasize the sensitivity of mixing and exchange to stratification, background currents, and near-boundary fluxes, highlighting the importance of accurately representing topography in numerical models of geophysical flows. Taken together, these findings contextualize how turbulence and exchange in abyssal boundary layers and dense overflow regions connect small-scale dynamics to basin-scale overturning, tracer transport, and energy pathways, shaping global heat, carbon, and nutrient distributions.

# Appendix A: Calculations of Intrusion Thickness

## A.1 Numerical calculation of tracer intrusion thickness

The thickness of interior dye intrusions is calculated for each simulation. At every time step the tracer concentration, initialized as a hyperbolic tangent function along the entire slope, is averaged in $x$, and smoothed in $y$ via a rolling window of 40 grid points, as shown in Fig. A.1 a for a representative time step. For each vertical profile of the tracer, the numerical derivative with respect to $z$ is used to find all local minima in the profile. If the sign of the derivative changes from negative to positive, then the concentration has reached a minimum, indicating a possible boundary for an intrusion. The near-slope region is excluded by removing points within 6 m of the slope, to avoid including the bottom boundary layer itself in the calculation of intrusion thickness.

As can be inferred from the profile in Fig. A.1b, the minima found are not always relevant. The local minima could just be a slight change in concentration within a much larger intrusion, or it could be a minima corresponding to an intrusion with very low concentration. To avoid such cases, intrusions are only included from a dye profile if the maximum concentration within a candidate intrusion reaches a threshold of $10^{-4}$, and its bordering minimums dropped at least half the concentration of the maximum. Such examples can be seen marked by the blue markers in Fig. A.1b. For example, if the maximum concentration of an intrusion in a certain dye profile is $10^{-3}$,

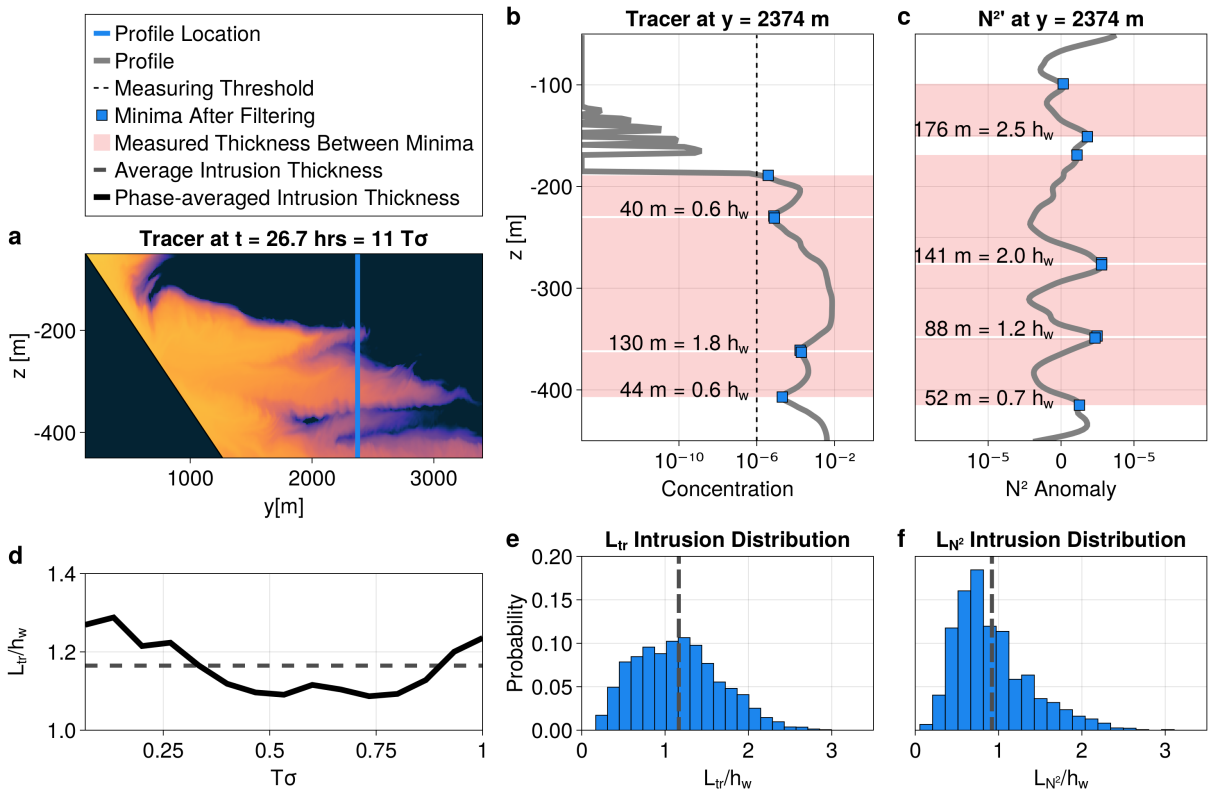



Figure A.1: Depiction of intrusion thickness in a representative profile. (a) tracer concentration at $t = 11T_\sigma$, after the initial smoothing, discussed in Appendix A.1 (b) the vertical profile of the tracer concentration taken at the location marked by the blue line in (a). The dashed line indicates the threshold for allowable values of concentration used in the calculation. (c) the vertical profile of stratification anomalies at the same location. Red shaded regions indicate an included intrusion calculation for either measure, with blue markers at the endpoints. (d) The phase-averaged tracer intrusion thickness normalized by the simulation's $h_w$ shows temporal variation around the mean. Probability distributions of all included tracer intrusions (e) and stratification anomaly intrusions (f).

then the bordering minima would have to be less than $5 \times 10^{-4}$ to include that intrusion in the average. The thickness of each intrusion is then measured above a $10^{-6}$ cutoff concentration of dye in the profile. So, even if the minimums surrounding an intrusion dropped to 0 concentration, the thickness would only measure to where the concentration had dropped to $10^{-6}$.

Once bounds are identified on the intrusions, the thickness can be easily found as the difference between the two minimums. The thickness of three such intrusions is marked in Fig. A.1b

by the red regions. All of these accepted intrusion thicknesses were averaged in space for each time step, and then in time over the last 5 wave periods to get an average intrusion thickness for each simulation. This is the value used in Fig. 3.11.

Various other methods and criteria for extracting intrusion thickness were also tested and the results were found to be qualitatively insensitive. As discussed in the text, we are primarily interested in characterizing the bulk variability, which we do using the mean, however, the median of the estimated tracer intrusion thickness gives similar results. There is however a large amount of variation in the estimated intrusion thickness within a single simulation, as can be seen by the three intrusions measured in Fig. A.1b, and the histogram of all of the measured intrusions for the full simulation in Fig. A.1e, especially for larger values of $h_w$. This variability is a function of both space (where for example position along the slope may lead to different intrusion thicknesses), wave phase as evidenced by the near boundary volume budget depicted in Fig. 3.14, as well as potentially a simple consequence of the turbulent breakdown of the large overturns which will energize a range of different scales. The adiabatic pumping of near boundary fluid will impact the amount of tracer captured in the interior as well as the average thickness. The phase-averaged intrusion thickness is shown in Fig. A.1d, varying $\pm 0.1 h_w$ around the total mean within a wave phase. Error estimates on the mean are calculated assuming a log-normal distribution (Fig. A.1), and treating snapshots in time (but not space) as providing independent degrees of freedom. The confidence intervals in Fig. 3.11 indicate that despite a large amount of variability, the scaling argument shown in the linear relationship still holds.

## A.2 Numerical calculation of interior stratification anomaly thickness

Stratification anomalies can also be used to define the thickness of intrusions, using the instantaneous $N^2$ values calculated in each simulation. The stratification anomaly is defined as $N^{2\prime} = N^2 - N_0^2$. To smooth the resulting values, a rolling average in $y$ of over 41 grid points, and in $z$ of 7 grid points is taken. To avoid the impact of the internal wave forcing, a rolling wave average is taken over one wave period as well. For the smallest $h_w$, as well as for the subcritical cases, this averaging is not enough, and we are unable to extract the impact of the mixing events from the regular wave patterns. Hence, these results are not included in Fig. 3.11b. For each time step, and each vertical profile, we find all the indices for the negative values of $N^{2\prime}$, above the same slope cutoff described in the previous section. Intervals of consecutive indices indicate the vertical extent of the stratification anomaly. The full range of a well-mixed intrusion will also include small positive regions on either side of the negative anomaly. To capture these, the first positive peak in stratification anomaly on either side of the negative range is taken to be the end points of the intrusion. An example of such a profile with the measured intrusions can be seen in Fig A.1c. After averaging over all the calculated thicknesses at a given time step, we again average in time over the last 4 waves (rolling wave average removes the last wave as a possibility) to find an average intrusion thickness for each simulation. The distribution of captured intrusion thicknesses for this method can be seen in Fig. A.1f, with the mean over the whole simulation marked by the gray dashed line. While there is again a lot of variability, the uncertainty calculation, shown by the 95th percent confidence intervals in Fig. 3.11b, indicates the scaling is robust.

# Appendix B: Grid Resolution Analysis

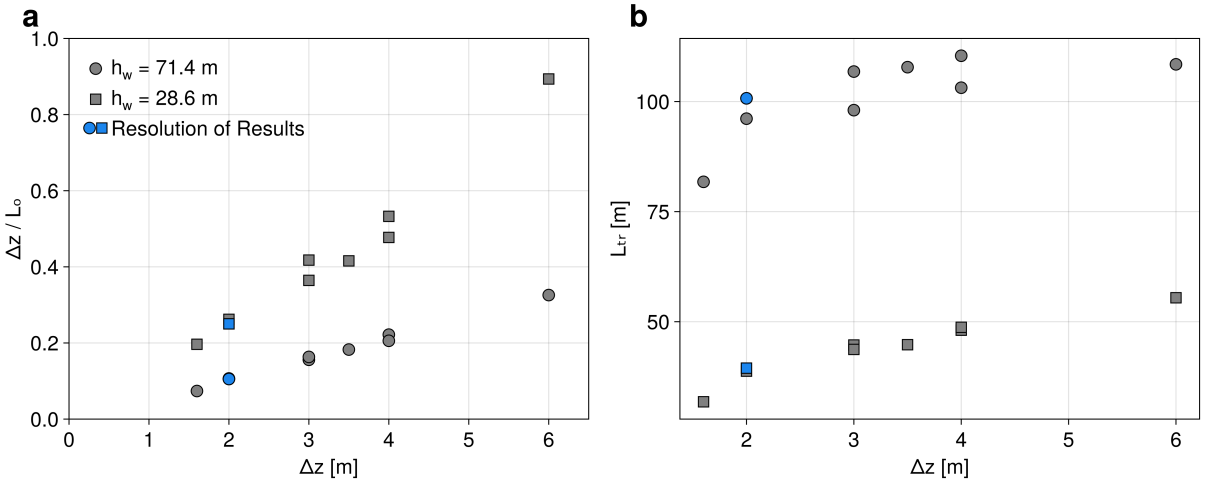



Figure B.1: Testing the resolution of the simulation set up by comparing a range of horizontal and vertical resolutions to the (a) Ozmidov length scale normalized by the vertical resolution and (b) the calculated average tracer intrusion thickness

To verify that our results from Chapter 3 were not dependent on grid resolution, extra simulations were run for two representative points in parameter space ($h_w = 42.86, 71.43$ m) from the Vary $V_0$ parameter set (see Table 3.1), with varying grid resolutions. As the Ozmidov length scale increases with $h_w$, the simulations chosen were on the lower end of the range of parameter space. These simulations were the same as those presented in the results, except for changes to the grid spacing. $\Delta z$ was varied by a factor of $0.8$ to $3$ times the used value of $\Delta z = 2$ m. The ratios $\Delta x/\Delta z = \Delta y/\Delta z$ were also varied between $1$ and $2$ to ensure the simulations were isotropic enough. LES of stratified turbulent flows have been found to produce the correct

results when their grid spacing is approximately equal to or smaller than the Ozmidov length scale (Khani, 2018), defined for this convergence study as

$$L_O = 2\pi\sqrt{\frac{\bar{\epsilon}}{N_0^3}}, \tag{B.1}$$

where $\bar{\epsilon}$ is defined as in Chapter 3 as the average dissipation rate of kinetic over wave periods 6 through 11 and $N_0$ is the buoyancy frequency defined by the initial stratification. The ratio of $L_O$ to the vertical grid resolution $\Delta z$ is plotted as a function of $\Delta z$ in Fig. B.1a, with the chosen resolution used for these results shown in blue for both effective wave heights tested. All simulations exceed the threshold, where $\Delta z/L_O = 1$,indicating that the simulations used for analysis were well-resolved for stratified LES problems (Khani, 2018).

Length scale results, as shown in the scatter plots in Chapter 3, were also not sensitive to the vertical scaling, as long as the effective wave height was well-resolved ($h_w \geq 3\Delta z$). The average tracer weighted thickness for the same range of resolutions is shown in Fig.B.1b with good agreement for all grid resolutions tested for both effective wave heights. Therefore, the resolution choice of $\Delta x = \Delta y = 4$ m and $\Delta z = 2$ m allows for the correct representation of the physics and turbulence found within these simulations.

# Bibliography


Adcroft, A., C. Hill, and J. Marshall, 1997: Representation of topography by shaved cells in a height coordinate ocean model. *Monthly Weather Review*, **125**, 2293–2315, doi: 10.1175/1520-0493(1997)125⟨2293:ROTBSC⟩2.0.CO;2.

Alford, M. H., J. A. MacKinnon, H. L. Simmons, and J. D. Nash, 2016: Near-inertial internal gravity waves in the ocean. *Annual Review of Marine Science*, **8**, 95–123, doi: 10.1146/annurev-marine-010814-015746.

Alford, M. H., and Coauthors, 2011: Energy flux and dissipation in luzon strait: Two tales of two ridges. *Journal of Physical Oceanography*, **41**, 2211–2222, doi: 10.1175/JPO-D-11-073.1.

Alford, M. H., and Coauthors, 2024: Buoyancy flux and mixing efficiency from direct, near-bottom turbulence measurements in a submarine canyon. *Submitted to J. Phys. Oceanogr.,*.

Allen, J. S., and P. A. Newberger, 1996: Downwelling circulation on the oregon continental shelf. part i: Response to idealized forcing. *Journal of Physical Oceanography*, **26**, doi: 10.1175/1520-0485(1996)026⟨2011:DCOTOC⟩2.0.CO;2.

Allen, J. S., and P. A. Newberger, 1998: On symmetric instabilities in oceanic bottom boundary layers. *Journal of Physical Oceanography*, **28**, 1131–1151, doi: 10.1175/1520-0485(1998)028⟨1131:OSIIOB⟩2.0.CO;2.

Almansi, M., T. W. N. Haine, R. S. Pickart, M. G. Magaldi, R. Gelderloos, and D. Mastropole, 2017: High-frequency variability in the circulation and hydrography of the denmark strait overflow from a high-resolution numerical model. *Journal of Physical Oceanography*, **47**, 2999–3013, doi: 10.1175/JPO-D-17-0129.1.

Arbic, B. K., A. J. Wallcraft, and E. J. Metzger, 2010: Concurrent simulation of the eddying general circulation and tides in a global ocean model. *Ocean Modelling*, **32**, 175–187, doi: 10.1016/j.ocemod.2010.01.007.

Armi, L., 1978: Some evidence for boundary mixing in the deep ocean. *Journal of Geophysical Research*, **83**, 1971, doi: 10.1029/JC083iC04p01971.

Arthur, R. S., K. A. Lundquist, D. J. Wiersema, J. Bao, and F. K. Chow, 2020: Evaluating implementations of the immersed boundary method in the weather research and forecasting model. *Monthly Weather Review*, **148**, 2087–2109, doi: 10.1175/MWR-D-19-0219.1.

Aucan, J., M. A. Merrifield, D. A. Luther, and P. Flament, 2006: Tidal mixing events on the deep flanks of kaena ridge, hawaii. *Journal of Physical Oceanography*, **36**, doi: 10.1175/JPO2888.1.

Bachman, S., B. Fox-Kemper, J. Taylor, and L. Thomas, 2017: Parameterization of frontal symmetric instabilities. i: Theory for resolved fronts. *Ocean Modelling*, **109**, 72–95, doi: 10.1016/j.ocemod.2016.12.003.

Bachman, S., and J. Taylor, 2014: Modelling of partially-resolved oceanic symmetric instability. *Ocean Modelling*, **82**, 15–27, doi: 10.1016/j.ocemod.2014.07.006.

Balmforth, N. J., and W. R. Young, 2002: Tidal conversion by subcritical topography. *Journal of Physical Oceanography*, **32**, 2900–2914.

Balwada, D., Q. Xiao, S. Smith, R. Abernathey, and A. R. Gray, 2021: Vertical fluxes conditioned on vorticity and strain reveal submesoscale ventilation. *Journal of Physical Oceanography*, doi: 10.1175/JPO-D-21-0016.1.

Beaird, N. L., P. B. Rhines, and C. C. Eriksen, 2013: Overflow waters at the iceland–faroe ridge observed in multiyear seaglider surveys. *Journal of Physical Oceanography*, **43**, 2334–2351, doi: 10.1175/JPO-D-13-029.1.

Bellafiore, D., W. J. McKiver, C. Ferrarin, and G. Umgiesser, 2018: The importance of modeling nonhydrostatic processes for dense water reproduction in the southern adriatic sea. *Ocean Modelling*, **125**, 22–38, doi: 10.1016/j.ocemod.2018.03.001.

Benthuysen, J., and L. N. Thomas, 2012: Friction and diapycnal mixing at a slope: Boundary control of potential vorticity. *Journal of Physical Oceanography*, **42**, 1509–1523, doi: 10.1175/JPO-D-11-0130.1.

Berntsen, J., G. Alendal, H. Avlesen, and Øyvind Thiem, 2018: Effects of the bottom boundary condition in numerical investigations of dense water cascading on a slope. *Ocean Dynamics*, **68**, 553–573, doi: 10.1007/s10236-018-1138-8.

Berntsen, J., Øyvind Thiem, and H. Avlesen, 2015: Internal pressure gradient errors in -coordinate ocean models in high resolution fjord studies. *Ocean Modelling*, **92**, 42–55, doi: 10.1016/j.ocemod.2015.05.009.

Boccaletti, G., R. Ferrari, and B. Fox-Kemper, 2007: Mixed layer instabilities and restratification. *Journal of Physical Oceanography*, **37**, 2228–2250, doi: 10.1175/JPO3101.1.

Bonnin, J., H. van Haren, P. Hosegood, and G.-J. A. Brummer, 2006: Burst resuspension of seabed material at the foot of the continental slope in the rockall channel. *Marine Geology*, **226**, 167–184, doi: 10.1016/j.margeo.2005.11.006.

Brearley, J. A., R. S. Pickart, H. Valdimarsson, S. Jonsson, R. W. Schmitt, and T. W. Haine, 2012: The east greenland boundary current system south of denmark strait. *Deep Sea Research Part I: Oceanographic Research Papers*, **63**, 1–19, doi: https://doi.org/10.1016/j.dsr.2012.01.001.

Brink, K. H., and D. A. Cherian, 2013: Instability of an idealized tidal mixing front: Symmetric instabilities and frictional effects. *Journal of Marine Research*, **71**, 425–450, doi: 10.1357/002224013812587582.

Brink, K. H., and S. J. Lentz, 2010: Buoyancy arrest and bottom ekman transport. part i: Steady flow. *Journal of Physical Oceanography*, **40**, 621–635, doi: 10.1175/2009JPO4266.1.

Briscolini, M., and P. Santangelo, 1989: Development of the mask method for incompressible unsteady flows. *Journal of Computational Physics*, **84**, 57–75.

Bryden, H. L., A. Mujahid, S. A. Cunningham, and T. Kanzow, 2009: Adjustment of the basin-scale circulation at 26 • n to variations in gulf stream, deep western boundary current and ekman transports as observed by the rapid array. *Ocean Sci*, **5**, 421–433.

Bullister, J. L., M. Rhein, and C. Mauritzen, 2013: *Chapter 10 - Deepwater Formation*, Vol. 103, 227–253. Academic Press, doi: https://doi.org/10.1016/B978-0-12-391851-2.00010-6, URL https://www.sciencedirect.com/science/article/pii/B9780123918512000106.

Cacchione, D. A., and D. E. Drake, 1986: Nepheloid layers and internal waves over continental shelves and slopes. *Geo-Marine Letters*, **6**, doi: 10.1007/BF02238085.

Callies, J., 2018: Restratification of abyssal mixing layers by submesoscale baroclinic eddies. *Journal of Physical Oceanography*, **48**, 1995–2010, doi: 10.1175/JPO-D-18-0082.1.

Callies, J., R. Ferrari, J. M. Klymak, and J. Gula, 2015: Seasonality in submesoscale turbulence. *Nature Communications*, **6**, doi: 10.1038/ncomms7862.

Cenedese, C., J. A. Whitehead, T. A. Ascarelli, and M. Ohiwa, 2004: A dense current flowing down a sloping bottom in a rotating fluid. *Journal of Physical Oceanography*, **34**, 188–203.

Chafik, L., J. Nilsson, T. Rossby, and A. K. Soman, 2023: The faroe-shetland channel jet: Structure, variability, and driving mechanisms. *Journal of Geophysical Research: Oceans*, **128**, doi: 10.1029/2022JC019083.

Chalamalla, V. K., B. Gayen, A. Scotti, and S. Sarkar, 2013: Turbulence during the reflection of internal gravity waves at critical and near-critical slopes. *Journal of Fluid Mechanics*, **729**, 47–68, doi: 10.1017/jfm.2013.240.

Chen, Z., J. Wenegrat, T. Chor, and P. Marchesiello, 2025: Evaluating turbulence parameterizations at gray zone resolutions for the ocean surface boundary layer. *Journal of Advances in Modeling Earth Systems*, **17**, doi: 10.1029/2025MS005104.

Cheriton, O. M., E. E. McPhee-Shaw, W. J. Shaw, T. P. Stanton, J. G. Bellingham, and C. D. Storlazzi, 2014: Suspended particulate layers and internal waves over the southern monterey bay continental shelf: An important control on shelf mud belts? *Journal of Geophysical Research: Oceans*, **119**, doi: 10.1002/2013JC009360.

Chor, T., and J. O. Wenegrat, 2025: The turbulent dynamics of anticyclonic submesoscale headland wakes. *Journal of Physical Oceanography*, **55**, 737–759, doi: 10.1175/JPO-D-24-0139.1.

Chor, T., J. O. Wenegrat, and J. Taylor, 2022: Insights into the mixing efficiency of submesoscale centrifugal–symmetric instabilities. *Journal of Physical Oceanography*, **52**, 2273–2287, doi: 10.1175/JPO-D-21-0259.1.

Chung, M.-H., 2006: Cartesian cut cell approach for simulating incompressible flows with rigid bodies of arbitrary shape. *Computers & Fluids*, **35**, 607–623, doi: 10.1016/j.compfluid.2005.04.005.

Churchill, J. H., P. E. Biscaye, and F. Aikman, 1988: The character and motion of suspended particulate matter over the shelf edge and upper slope off cape cod. *Continental Shelf Research*, **8**, doi: 10.1016/0278-4343(88)90077-5.

Coleman, G. N., J. H. Ferziger, and P. R. Spalart, 1990: A numerical study of the turbulent ekman layer. *Journal of Fluid Mechanics*, **213**, 313–348, doi: 10.1017/S0022112090002348.

Colombo, P., and Coauthors, 2020: Representation of the denmark strait overflow in a z - coordinate eddying configuration of the nemo (v3.6) ocean model: resolution and parameter impacts. *Geoscientific Model Development*, **13**, 3347–3371, doi: 10.5194/gmd-13-3347-2020.

Cyr, F., and H. van Haren, 2016a: Observations of small-scale secondary instabilities during the shoaling of internal bores on a deep-ocean slope. *Journal of Physical Oceanography*, **46**, 219–231, doi: 10.1175/JPO-D-15-0059.1.

Cyr, F., and H. van Haren, 2016b: Observations of small-scale secondary instabilities during the shoaling of internal bores on a deep-ocean slope. *Journal of Physical Oceanography*, **46**, 219–231, doi: 10.1175/JPO-D-15-0059.1.

Danabasoglu, G., W. G. Large, and B. P. Briegleb, 2010: Climate impacts of parameterized nordic sea overflows. *Journal of Geophysical Research: Oceans*, **115**, doi: 10.1029/2010JC006243.

D'Asaro, E. A., 1995a: Upper-ocean inertial currents forced by a strong storm. part ii: Modeling. *Journal of Physical Oceanography*, **25**, 2937–2952, doi: 10.1175/1520-0485(1995)025⟨2937:UOICFB⟩2.0.CO;2.

D'Asaro, E. A., 1995b: Upper-ocean inertial currents forced by a strong storm. part iii: Interaction of inertial currents and mesoscale eddies. *Journal of Physical Oceanography*, **25**, 2953–2958, doi: 10.1175/1520-0485(1995)025⟨2953:UOICFB⟩2.0.CO;2.

DeLeon, R., M. Sandusky, and I. Senocak, 2018: Simulations of turbulent flow over complex terrain using an immersed-boundary method. *Boundary-Layer Meteorology*, **167**, 399–420, doi: 10.1007/s10546-018-0336-8.

Dickson, R. R., and J. Brown, 1994: The production of north atlantic deep water: Sources, rates, and pathways. *Journal of Geophysical Research: Oceans*, **99**, 12 319–12 341, doi: 10.1029/94JC00530.

Dillon, T. M., 1982: Vertical overturns: A comparison of thorpe and ozmidov length scales. *Journal of Geophysical Research*, **87**, doi: 10.1029/jc087ic12p09601.

Dong, J., B. Fox-Kemper, J. O. Wenegrat, A. S. Bodner, X. Yu, S. Belcher, and C. Dong, 2024: Submesoscales are a significant turbulence source in global ocean surface boundary layer. *Nature Communications*, **15**, 9566, doi: 10.1038/s41467-024-53959-y.

Dong, J., Z. Jing, B. Fox-Kemper, Y. Wang, H. Cao, and C. Dong, 2022: Effects of symmetric instability in the kuroshio extension region in winter. *Deep Sea Research Part II: Topical Studies in Oceanography*, **202**, 105 142, doi: 10.1016/j.dsr2.2022.105142.

Drake, H. F., R. Ferrari, and J. Callies, 2020: Abyssal circulation driven by near-boundary mixing: Water mass transformations and interior stratification. *Journal of Physical Oceanography*, **50**, 2203–2226, doi: 10.1175/JPO-D-19-0313.1.

Drazin, P. G., 1961: On the steady flow of a fluid of variable density past an obstacle. *Tellus*, **13**, 239–251, doi: 10.1111/j.2153-3490.1961.tb00081.x.

Edge, W. C., N. L. Jones, M. D. Rayson, and G. N. Ivey, 2021: Calibrated suspended sediment observations beneath large amplitude non-linear internal waves. *Journal of Geophysical Research: Oceans*, **126**, doi: 10.1029/2021JC017538.

Eriksen, C. C., 1985: Implications of ocean bottom reflection for internal wave spectra and mixing. *Journal of Physical Oceanography*, **15**, doi: 10.1175/1520-0485(1985)015⟨1145:ioobrf⟩2.0.co;2.

Evans, D. G., N. P. Holliday, S. Bacon, and I. L. Bras, 2022: Mixing and air-sea buoyancy fluxes set the time-mean overturning circulation in the subpolar north atlantic. *EGUsphere*, 1–36, doi: 10.5194/egusphere-2022-1059.

Fadlun, E. A., R. Verzicco, P. Orlandi, and J. Mohd-Yusof, 2000: Combined immersed-boundary finite-difference methods for three-dimensional complex flow simulations. *Journal of Computational Physics*, **161**, 35–60, doi: 10.1006/jcph.2000.6484.

Falcini, F., and E. Salusti, 2015: Friction and mixing effects on potential vorticity for bottom current crossing a marine strait: An application to the sicily channel (central mediterranean sea). *Ocean Science*, **11**, 391–403, doi: 10.5194/os-11-391-2015.

Farrar, J. T., and Coauthors, 2025: S-mode: The sub-mesoscale ocean dynamics experiment. *Bulletin of the American Meteorological Society*, **106**, E657–E677, doi: 10.1175/BAMS-D-23-0178.1.

Fedkiw, R. P., 2002: Coupling an eulerian fluid calculation to a lagrangian solid calculation with the ghost fluid method. *Journal of Computational Physics*, **175**, 200–224, doi: 10.1006/jcph.2001.6935.

Ferrari, R., 2014: What goes down must come up. *Nature*, **513**, 179–180, doi: 10.1038/513179a.

Ferrari, R., A. Mashayek, T. J. McDougall, M. Nikurashin, and J. M. Campin, 2016: Turning ocean mixing upside down. *Journal of Physical Oceanography*, **46**, doi: 10.1175/JPO-D-15-0244.1.

Fornberg, B., 1980: A numerical study of steady viscous flow past a circular cylinder. *Journal of Fluid Mechanics*, **98**, 819–855.

Fox-Kemper, B., R. Ferrari, and R. Hallberg, 2008: Parameterization of mixed layer eddies. part i: Theory and diagnosis. *Journal of Physical Oceanography*, **38**, 1145–1165, doi: 10.1175/2007JPO3792.1.

Friedlingstein, P., and Coauthors, 2022: Global carbon budget 2021. *Earth System Science Data*, **14**, 1917–2005, doi: 10.5194/essd-14-1917-2022.

Friedrich, T., A. Timmermann, T. Decloedt, D. Luther, and A. Mouchet, 2011: The effect of topography-enhanced diapycnal mixing on ocean and atmospheric circulation and marine biogeochemistry. *Ocean Modelling*, **39**, 262–274, doi: 10.1016/j.ocemod.2011.04.012.

Garabato, A. C. N., X. Yu, J. Callies, R. Barkan, K. L. Polzin, E. E. Frajka-Williams, C. E. Buckingham, and S. M. Griffies, 2022: Kinetic energy transfers between mesoscale and submesoscale motions in the open ocean's upper layers. *Journal of Physical Oceanography*, **52**, 75–97, doi: 10.1175/JPO-D-21-0099.1.

Garabato, A. C. N., and Coauthors, 2017: Vigorous lateral export of the meltwater outflow from beneath an antarctic ice shelf. *Nature*, **542**, 219–222, doi: 10.1038/nature20825.

Garabato, A. C. N., and Coauthors, 2019: Rapid mixing and exchange of deep-ocean waters in an abyssal boundary current. *Proceedings of the National Academy of Sciences*, **116**, 13 233–13 238, doi: 10.1073/pnas.1904087116.

Gardner, W. D., B. E. Tucholke, M. J. Richardson, and P. E. Biscaye, 2017: Benthic storms, nepheloid layers, and linkage with upper ocean dynamics in the western north atlantic. *Marine Geology*, **385**, 304–327, doi: 10.1016/j.margeo.2016.12.012.

Garrett, C., P. Maccready, and P. Rhines, 1993: Boundary mixing and arrested ekman layers: Rotating stratified flow near a sloping boundary. *Annu. Rev. Fluid Mech*, **25**, 291–323.

Gawarkiewicz, G., and D. C. Chapman, 1995: A numerical study of dense water formation and transport on a shallow, sloping continental shelf. *Journal of Geophysical Research: Oceans*, **100**, 4489–4507, doi: 10.1029/94JC01742.

Gayen, B., and S. Sarkar, 2011: Boundary mixing by density overturns in an internal tidal beam. *Geophysical Research Letters*, **38**, doi: 10.1029/2011GL048135.

Gemmrich, J., and J. M. Klymak, 2015: Dissipation of internal wave energy generated on a critical slope. *Journal of Physical Oceanography*, **45**, 2221–2238, doi: 10.1175/JPO-D-14-0236.1.

Gill, A. E., 1982: *Atmosphere-Ocean Dynamics*, Vol. 110. Academic Press, 280-281 pp., doi: 10.1002/qj.49711046322.

Girton, J. B., and T. B. Sanford, 2003: Descent and modification of the overflow plume in the denmark strait *. *Journal of Physical Oceanography*, **33**, 1351–1364, doi: GirtonSanford2003.

Girton, J. B., T. B. Sanford, and R. H. Käse, 2001: Synoptic sections of the denmark strait overflow. *Geophysical Research Letters*, **28**, 1619–1622, doi: 10.1029/2000GL011970.

Goldsworth, F. W., H. L. Johnson, D. P. Marshall, and I. A. L. Bras, 2024: Destratifying and restratifying instabilities during down-front wind events: A case study in the irminger sea. *Journal of Geophysical Research: Oceans*, **129**, doi: 10.1029/2023JC020365.

Gula, J., M. J. Molemaker, and J. C. McWilliams, 2015: Topographic vorticity generation, submesoscale instability and vortex street formation in the gulf stream. *Geophysical Research Letters*, **42**, 4054–4062, doi: 10.1002/2015GL063731.

Gula, J., M. J. Molemaker, and J. C. McWilliams, 2016a: Submesoscale dynamics of a gulf stream frontal eddy in the south atlantic bight. *Journal of Physical Oceanography*, **46**, 305–325, doi: 10.1175/JPO-D-14-0258.1.

Gula, J., M. J. Molemaker, and J. C. McWilliams, 2016b: Topographic generation of submesoscale centrifugal instability and energy dissipation. *Nature Communications*, **7**, 12 811, doi: 10.1038/ncomms12811.

Haine, T. W. N., and J. Marshall, 1998: Gravitational, symmetric, and baroclinic instability of the ocean mixed layer. *Journal of Physical Oceanography*, **28**, 634–658, doi: 10.1175/1520-0485(1998)028⟨0634:GSABIO⟩2.0.CO;2.

Holmes, R. M., C. D. LAVERGNE, and T. J. McDougall, 2019: Tracer transport within abyssal mixing layers. *Journal of Physical Oceanography*, **49**, 2669–2695, doi: 10.1175/JPO-D-19-0006.1.

Holmes, R. M., and T. J. McDougall, 2020: Diapycnal transport near a sloping bottom boundary. *Journal of Physical Oceanography*, **50**, doi: 10.1175/JPO-D-20-0066.1.

Hopfinger, E. J., 1987: Turbulence in stratified fluids: A review. *Journal of Geophysical Research*, **92**, 5287, doi: 10.1029/JC092iC05p05287.

Jagannathan, A., K. Srinivasan, J. C. McWilliams, J. Molemaker, and A. L. Stewart, 2023: Evolution of bottom boundary layers on three dimensional topography—buoyancy adjustment and instabilities. *Journal of Geophysical Research: Oceans*, **128**, doi: 10.1029/2023JC019705.

Jagannathan, A., K. Srinivasan, J. C. McWilliams, M. J. Molemaker, and A. L. Stewart, 2021: Boundary layer-mediated vorticity generation in currents over sloping bathymetry. *Journal of Physical Oceanography*, doi: 10.1175/JPO-D-20-0253.1.

Jalali, M., V. K. Chalamalla, and S. Sarkar, 2017: On the accuracy of overturn-based estimates of turbulent dissipation at rough topography. *Journal of Physical Oceanography*, **47**, 513–532, doi: 10.1175/JPO-D-15-0169.1.

Jalali, M., and S. Sarkar, 2017: Large eddy simulation of flow and turbulence at the steep topography of luzon strait. *Geophysical Research Letters*, **44**, 9440–9448, doi: 10.1002/2017GL074119.

Jiang, Y., J. Dong, X. Zhang, W. Zhang, H. Wang, and W. Zhang, 2022: Evaluating the effects of a symmetric instability parameterization scheme in the xisha-zhongsha waters, south china sea in winter. *Frontiers in Marine Science*, **9**, doi: 10.3389/fmars.2022.985605.

Jochum, M., 2009: Impact of latitudinal variations in vertical diffusivity on climate simulations. *Journal of Geophysical Research: Oceans*, **114**, doi: 10.1029/2008JC005030.

Jones, N. L., G. N. Ivey, M. D. Rayson, and S. M. Kelly, 2020: Mixing driven by breaking nonlinear internal waves. *Geophysical Research Letters*, **47**, doi: 10.1029/2020GL089591.

Kaiser, B. E., L. J. Pratt, and J. Callies, 2022: Low-reynolds-number oscillating boundary layers on adiabatic slopes. *Journal of Fluid Mechanics*, **950**, A4, doi: 10.1017/jfm.2022.794.

Kanarska, Y., A. Shchepetkin, and J. McWilliams, 2007: Algorithm for non-hydrostatic dynamics in the regional oceanic modeling system. *Ocean Modelling*, **18**, 143–174, doi: 10.1016/j.ocemod.2007.04.001.

Khani, S., 2018: Mixing efficiency in large-eddy simulations of stratified turbulence. *Journal of Fluid Mechanics*, **849**, 373–394, doi: 10.1017/jfm.2018.417.

Killworth, P. D., 1983: Deep convection in the world ocean. *Reviews of Geophysics*, **21**, 1–26, doi: 10.1029/RG021i001p00001.

Klemp, J. B., 2011: A terrain-following coordinate with smoothed coordinate surfaces. *Monthly Weather Review*, **139**, 2163–2169, doi: 10.1175/MWR-D-10-05046.1.

Klemp, J. B., W. C. Skamarock, and O. Fuhrer, 2003: Numerical consistency of metric terms in terrain-following coordinates. *Monthly Weather Review*, **131**, 1229–1239, doi: 10.1175/1520-0493(2003)131⟨1229:NCOMTI⟩2.0.CO;2.

Klinck, J. M., and M. S. Dinniman, 2010: Exchange across the shelf break at high southern latitudes. *Ocean Science*, **6**, 513–524, doi: 10.5194/os-6-513-2010.

Klocker, A., and T. J. McDougall, 2010: Influence of the nonlinear equation of state on global estimates of dianeutral advection and diffusion. *Journal of Physical Oceanography*, **40**, 1690–1709, doi: 10.1175/2010JPO4303.1.

Klymak, J. M., S. Legg, M. H. Alford, M. Buijsman, R. Pinkel, and J. D. Nash, 2012: The direct breaking of internal waves at steep topography. *Oceanography*, **25**, 153–159, doi: 10.5670/oceanog.2012.50.

Koszalka, I. M., T. W. N. Haine, and M. G. Magaldi, 2013: Fates and travel times of denmark strait overflow water in the irminger basin*. *Journal of Physical Oceanography*, **43**, 2611–2628, doi: 10.1175/JPO-D-13-023.s1.

Kunze, E., 1985: Near-inertial wave propagation in geostrophic shear. *Journal of Physical Oceanography*, **15**, 544–565.

Kunze, E., 2017: The internal-wave-driven meridional overturning circulation. *Journal of Physical Oceanography*, **47**, 2673–2689, doi: 10.1175/JPO-D-16-0142.1.

Kunze, E., E. Firing, J. M. Hummon, T. K. Chereskin, and A. M. Thurnherr, 2006: Global abyssal mixing inferred from lowered adcp shear and ctd strain profiles. *Journal of Physical Oceanography*, **36**, 1553–1576, doi: 10.1175/JPO2926.1.

Kunze, E., R.-C. Lien, C. B. Whalen, J. B. Girton, B. Ma, and M. C. Buijsman, 2023: Seasonal variability of near-inertial/semidiurnal fluctuations and turbulence in the subarctic north atlantic. *Journal of Physical Oceanography*, **53**, 2717–2735, doi: 10.1175/JPO-D-22-0231.1.

Kunze, E., C. Mackay, E. E. Mcphee-Shaw, K. Morrice, J. B. Girton, and S. R. Terker, 2012: Turbulent mixing and exchange with interior waters on sloping boundaries. *Journal of Physical Oceanography*, **42**, 910–927, doi: 10.1175/JPO-D-11-075.1.

Köhl, A., R. H. Käse, D. Stammer, and N. Serra, 2007: Causes of changes in the denmark strait overflow. *Journal of Physical Oceanography*, **37**, 1678–1696, doi: 10.1175/JPO3080.1.

Lamb, K. G., 2014: Internal wave breaking and dissipation mechanisms on the continental slope/shelf. *Annual Review of Fluid Mechanics*, **46**, 231–254, doi: 10.1146/annurev-fluid-011212-140701.

Laurent, L. C. S., J. M. Toole, and R. W. Schmitt, 2001: Buoyancy forcing by turbulence above rough topography in the abyssal brazil basin *. *Journal of Physical Oceanography*, **31**, 3476–3495.

Le, H., and P. Moin, 1991: An improvement of fractional step methods for the incompressible navier-stokes equations. *Journal of Computational Physics*, **92**, 369–379, doi: 10.1016/0021-9991(91)90215-7.

Le Bras, I. A.-A., J. Callies, F. Straneo, T. C. Biló, J. Holte, and H. L. Johnson, 2022: Slantwise convection in the irminger sea. *Journal of Geophysical Research: Oceans*, **127**, doi: 10.1029/2022JC019071.

Legg, S., 2012: *Overflows and Convectively Driven Flows*, 203–235. Cambridge University Press.

Legg, S., and J. Klymak, 2008: Internal hydraulic jumps and overturning generated by tidal flow over a tall steep ridge. *Journal of Physical Oceanography*, **38**, 1949–1964, doi: 10.1175/2008JPO3777.1.

Legg, S., and Coauthors, 2009: Improving oceanic overflow representation in climate models: The gravity current entrainment climate process team. *Bulletin of the American Meteorological Society*, **90**, doi: 10.1175/2008BAMS2667.I.

Lin, P., R. S. Pickart, K. Jochumsen, G. W. K. Moore, H. Valdimarsson, T. Fristedt, and L. J. Pratt, 2020: Kinematic structure and dynamics of the denmark strait overflow from ship-based observations. *Journal of Physical Oceanography*, **50**, 3235–3251, doi: 10.1175/JPO-D-20-0095.1.

Lumpkin, R., and K. Speer, 2007: Global ocean meridional overturning. *Journal of Physical Oceanography*, **37**, 2550–2562, doi: 10.1175/JPO3130.1.

Lundquist, K. A., F. K. Chow, and J. K. Lundquist, 2012: An immersed boundary method enabling large-eddy simulations of flow over complex terrain in the wrf model. *Monthly Weather Review*, **140**, 3936–3955, doi: 10.1175/MWR-D-11-00311.1.

Lévy, M., P. Klein, A.-M. Tréguier, D. Iovino, G. Madec, S. Masson, and K. Takahashi, 2010: Modifications of gyre circulation by sub-mesoscale physics. *Ocean Modelling*, **34**, 1–15, doi: 10.1016/j.ocemod.2010.04.001.

MacCready, P., and P. B. Rhines, 1991: Buoyant inhibition of ekman transport on a slope and its effect on stratified spin-up. *Journal of Fluid Mechanics*, **223**, 631–661, doi: 10.1017/S0022112091001581.

MacKinnon, J. A., and Coauthors, 2017: Climate process team on internal wave-driven ocean mixing. *Bulletin of the American Meteorological Society*, **98**, 2429–2454, doi: 10.1175/BAMS-D-16-0030.1.

Magaldi, M. G., and T. W. Haine, 2015: Hydrostatic and non-hydrostatic simulations of dense waters cascading off a shelf: The east greenland case. *Deep-Sea Research Part I: Oceanographic Research Papers*, **96**, 89–104, doi: 10.1016/j.dsr.2014.10.008.

Magaldi, M. G., T. W. N. Haine, and R. S. Pickart, 2011: On the nature and variability of the east greenland spill jet: A case study in summer 2003*. *Journal of Physical Oceanography*, **41**, doi: 10.1175/JPO-D-10.

Mahadevan, A., 2016: The impact of submesoscale physics on primary productivity of plankton. *Annual Review of Marine Science*, **8**, 161–184, doi: 10.1146/annurev-marine-010814-015912.

Maltrud, M. E., and J. L. McClean, 2005: An eddy resolving global 1/10° ocean simulation. *Ocean Modelling*, **8**, 31–54, doi: 10.1016/j.ocemod.2003.12.001.

Maronga, B., and Coauthors, 2015: The parallelized large-eddy simulation model (palm) version 4.0 for atmospheric and oceanic flows: model formulation, recent developments, and future perspectives. *Geoscientific Model Development*, **8**, 2515–2551, doi: 10.5194/gmd-8-2515-2015.

Marshall, J., A. Adcroft, C. Hill, L. Perelman, and C. Heisey, 1997: A finite-volume, incompressible navier stokes model for studies of the ocean on parallel computers. *J. Geophys. Res.*, **102**, 5753–5766.

Marshall, J., D. Jamous, and J. Nilsson, 1999: Reconciling thermodynamic and dynamic methods of computation of water-mass transformation rates. *Deep Sea Research I*, **46**, 545–572.

Marshall, J., D. Jamous, and J. Nilsson, 2001: Entry, flux, and exit of potential vorticity in ocean circulation.

Mashayek, A., R. Ferrari, S. Merrifield, J. R. Ledwell, L. S. Laurent, and A. N. Garabato, 2017: Topographic enhancement of vertical turbulent mixing in the southern ocean. *Nature Communications*, **8**, 14 197, doi: 10.1038/ncomms14197.

Mater, B. D., S. M. Schaad, and S. K. Venayagamoorthy, 2013: Relevance of the thorpe length scale in stably stratified turbulence. *Physics of Fluids*, **25**, doi: 10.1063/1.4813809.

Mater, B. D., S. K. Venayagamoorthy, L. S. Laurent, and J. N. Moum, 2015: Biases in thorpe-scale estimates of turbulence dissipation. part i: Assessments from large-scale overturns in oceanographic data. *Journal of Physical Oceanography*, **45**, 2497–2521, doi: 10.1175/JPO-D-14-0128.1.

McPhee-Shaw, E., 2006: Boundary–interior exchange: Reviewing the idea that internal-wave mixing enhances lateral dispersal near continental margins. *Deep Sea Research Part II: Topical Studies in Oceanography*, **53**, 42–59, doi: 10.1016/j.dsr2.2005.10.018.

McPhee-Shaw, E., R. Sternberg, B. Mullenbach, and A. Ogston, 2004: Observations of intermediate nepheloid layers on the northern california continental margin. *Continental Shelf Research*, **24**, 693–720, doi: 10.1016/j.csr.2004.01.004.

McPhee-Shaw, E. E., and E. Kunze, 2002: Boundary layer intrusions from a sloping bottom: A mechanism for generating intermediate nepheloid layers. *Journal of Geophysical Research*, **107**, doi: 10.1029/2001jc000801.

McPhee-Shaw, E. E., E. Kunze, and J. B. Girton, 2021a: Submarine canyon oxygen anomaly caused by mixing and boundary-interior exchange. *Geophysical Research Letters*, **48**, doi: 10.1029/2021GL092995.

McPhee-Shaw, E. E., E. Kunze, and J. B. Girton, 2021b: Submarine canyon oxygen anomaly caused by mixing and boundary-interior exchange. *Geophysical Research Letters*, **48**, doi: 10.1029/2021GL092995.

McWilliams, J. C., 2016: Submesoscale currents in the ocean. *Proceedings of the Royal Society A: Mathematical, Physical and Engineering Sciences*, **472**, 20160 117, doi: 10.1098/rspa.2016.0117.

McWilliams, J. C., E. Huckle, and A. F. Shchepetkin, 2009: Buoyancy effects in a stratified ekman layer. *Journal of Physical Oceanography*, **39**, 2581–2599, doi: 10.1175/2009JPO4130.1.

Meinen, C. S., D. S. Luther, and M. O. Baringer, 2009: Structure, transport and potential vorticity of the gulf stream at 68°w: Revisiting older data sets with new techniques. *Deep Sea Research Part I: Oceanographic Research Papers*, **56**, 41–60, doi: 10.1016/j.dsr.2008.07.010.

Melet, A., S. Legg, and R. Hallberg, 2016: Climatic impacts of parameterized local and remote tidal mixing. *Journal of Climate*, **29**, 3473–3500, doi: 10.1175/JCLI-D-15-0153.1.

Mittal, R., and G. Iaccarino, 2005: Immersed boundary methods. *Annual Review of Fluid Mechanics*, **37**, 239–261, doi: 10.1146/annurev.fluid.37.061903.175743.

Mooers, C. N. K., 1975: Several effects of a baroclinic current on the cross-stream propagation of inertial-internal waves†. *Geophysical Fluid Dynamics*, **6**, 245–275, doi: 10.1080/03091927509365797.

Muench, R. D., and A. L. Gordon, 1995: Circulation and transport of water along the western weddell sea margin. *Journal of Geophysical Research: Oceans*, **100**, 18 503–18 515, doi: 10.1029/95JC00965.

Munk, W., and C. Wunsch, 1998: Abyssal recipes ii: energetics of tidal and wind mixing. *Deep Sea Research Part I: Oceanographic Research Papers*, **45**, 1977–2010, doi: 10.1016/S0967-0637(98)00070-3.

Munk, W. H., 1966: Abyssal recipes. *Deep-Sea Research and Oceanographic Abstracts*, **13**, doi: 10.1016/0011-7471(66)90602-4.

Nash, J. D., M. H. Alford, E. Kunze, K. Martini, and S. Kelly, 2007: Hotspots of deep ocean mixing on the oregon continental slope. *Geophysical Research Letters*, **34**, doi: 10.1029/2006GL028170.

Nasr-Azadani, M. M., and E. Meiburg, 2011: Turbins: An immersed boundary, navier–stokes code for the simulation of gravity and turbidity currents interacting with complex topographies. *Computers & Fluids*, **45**, 14–28, doi: 10.1016/j.compfluid.2010.11.023.

Nielsen, S. B., M. Jochum, C. Eden, and R. Nuterman, 2018: An energetically consistent vertical mixing parameterization in ccsm4. *Ocean Modelling*, **127**, 46–54, doi: 10.1016/j.ocemod.2018.03.002.

Nielson, J. R., and S. M. Henderson, 2022: Bottom boundary layer mixing processes across internal seiche cycles: Dominance of downslope flows. *Limnology and Oceanography*, **67**, 1111–1125, doi: 10.1002/lno.12060.

Nokes, R. L., and G. N. Ivey, 1989: Vertical mixing due to the breaking of critical internal waves on sloping boundaries. *Journal of Fluid Mechanics*, **204**, doi: 10.1017/S0022112089001849.

Pedlosky, J., 2014: Symmetric instability of cross-stream varying currents. *Journal of Marine Research*, **72**, 31–45.

Petruncio, E. T., L. K. Rosenfeld, and J. D. Paduan, 1997: Observations of the internal tide in monterey canyon. *Journal of Physical Oceanography*.

Polzin, K. L., J. M. Toole, J. R. Ledwell, and R. W. Schmitt, 1997: Spatial variability of turbulent mixing in the abyssal ocean. *Science*, **276**, 93–96.

Pope, S. B., 2008: *Turbulent flows*. Cambridge University Press.

Pressel, K. G., S. Mishra, T. Schneider, C. M. Kaul, and Z. Tan, 2017: Numerics and subgrid-scale modeling in large eddy simulations of stratocumulus clouds. *Journal of Advances in Modeling Earth Systems*, **9 (2)**, 1342–1365, doi: https://doi.org/10.1002/2016MS000778, https://agupubs.onlinelibrary.wiley.com/doi/pdf/10.1002/2016MS000778.

Qu, L., L. Thomas, and J. Gula, 2021a: Bottom mixing enhanced by tropical storm-generated near-inertial waves entering critical layers in the straits of florida. *Geophysical Research Letters*, **48**, doi: 10.1029/2021GL093773.

Qu, L., L. N. Thomas, and R. D. Hetland, 2021b: Near-inertial-wave critical layers over sloping bathymetry. *Journal of Physical Oceanography*, **51**, 1737–1756, doi: 10.1175/JPO-D-20-0221.1.

Qu, L., L. N. Thomas, R. D. Hetland, and D. Kobashi, 2022: Mixing driven by critical reflection of near-inertial waves over the texas-louisiana shelf. *Journal of Physical Oceanography*, doi: 10.1175/JPO-D-22-0004.1.

Racapé, V., V. Thierry, H. Mercier, and C. Cabanes, 2019: Isow spreading and mixing as revealed by deep-argo floats launched in the charlie-gibbs fracture zone. *Journal of Geophysical Research: Oceans*, **124**, 6787–6808, doi: 10.1029/2019JC015040.

Ramadhan, A., and Coauthors, 2020: Oceananigans.jl: Fast and friendly geophysical fluid dynamics on gpus. *Journal of Open Source Software*, **5**, 2018, doi: 10.21105/joss.02018.

Remmler, S., S. Hickel, M. D. Fruman, and U. Achatz, 2015: Validation of large-eddy simulation methods for gravity wave breaking. *Journal of the Atmospheric Sciences*, **72**, 3537–3562, doi: 10.1175/JAS-D-14-0321.1.

Reynolds, W. C., and A. K. Hussain, 1972: The mechanics of an organized wave in turbulent shear flow. part 3. theoretical models and comparisons with experiments. *Journal of Fluid Mechanics*, **54**, doi: 10.1017/S0022112072000679.

Riser, S. C., and Coauthors, 2016: Fifteen years of ocean observations with the global argo array. *Nature Climate Change*, **6**, 145–153, doi: 10.1038/nclimate2872.

Ruan, X., Y. Si, and R. Ferrari, 2025: Diapycnal upwelling driven by tidally induced mixing over steep topography. *Journal of Physical Oceanography*, **55**, 229–241, doi: 10.1175/JPO-D-24-0008.1.

Ruan, X., A. F. Thompson, M. M. Flexas, and J. Sprintall, 2017: Contribution of topographically generated submesoscale turbulence to southern ocean overturning. *Nature Geoscience*, **10**, 840–845, doi: 10.1038/ngeo3053.

Saberi, A., T. W. N. Haine, R. Gelderloos, M. F. de Jong, H. Furey, and A. Bower, 2020: Lagrangian perspective on the origins of denmark strait overflow. *Journal of Physical Oceanography*, **50**, 2393–2414, doi: 10.1175/JPO-D-19-0210.1.

Sarkar, S., and A. Scotti, 2017: From topographic internal gravity waves to turbulence. *Annual Review of Fluid Mechanics*, **49**, 195–220, doi: 10.1146/annurev-fluid-010816-060013.

Schneider, T., S. Lan, A. Stuart, and J. Teixeira, 2017: Earth system modeling 2.0: A blueprint for models that learn from observations and targeted high-resolution simulations. *Geophysical Research Letters*, **44**, doi: 10.1002/2017GL076101.

Schubert, R., J. Gula, E. Capó, P. Damien, M. J. Molemaker, C. Vic, and J. C. McWilliams, 2025: The ocean flows downhill near the seafloor and recirculates upward above. *Nature Communications*, **16**, 5873, doi: 10.1038/s41467-025-61027-2.

Schumann, J. E., S. Toosi, and J. Larsson, 2020: Assessment of grid anisotropy effects on large-eddy-simulation models with different length scales. *AIAA Journal*, **58**, 4522–4533, doi: 10.2514/1.J059576.

Schär, C., 1993: A generalization of bernoulli's theorem. *Journal of the Atomspheric Sciences*, **50**, 1437–1443.

Scorer, R. S., 1949: Theory of waves in the lee of mountains. *Quarterly Journal of the Royal Meteorological Society*, **75**, 41–56, doi: 10.1002/qj.49707532308.

Seo, J. H., and R. Mittal, 2011: A high-order immersed boundary method for acoustic wave scattering and low-mach number flow-induced sound in complex geometries. *Journal of Computational Physics*, **230**, 1000–1019, doi: 10.1016/j.jcp.2010.10.017.

Silvestri, S., G. L. Wagner, J.-M. Campin, N. C. Constantinou, C. N. Hill, A. N. Souza, and R. Ferrari, 2024: A new weno-based momentum advection scheme for simulations of ocean mesoscale turbulence. *Journal of Advances in Modeling Earth Systems*, doi: 10.22541/essoar.170110657.76489860/v2.

Slinn, D. N., and J. J. Riley, 1998: Theoretical and computational fluid dynamics turbulent dynamics of a critically reflecting internal gravity wave 1. *Theoret. Comput. Fluid Dynamics*, **11**, 281–303.

Smith, P. C., 1976: Baroclinic instability in the denmark strait overflow. *Journal of Physical Oceanography*, **6**, 355–371, doi: 10.1175/1520-0485(1976)006⟨0355:BIITDS⟩2.0.CO;2.

Soufflet, Y., P. Marchesiello, F. Lemarié, J. Jouanno, X. Capet, L. Debreu, and R. Benshila, 2016: On effective resolution in ocean models. *Ocean Modelling*, **98**, 36–50, doi: 10.1016/j.ocemod.2015.12.004.

Spall, M. A., R. S. Pickart, P. Lin, W.-J. von Appen, D. Mastropole, H. Valdimarsson, T. W. N. Haine, and M. Almansi, 2019: Frontogenesis and variability in denmark strait and its influence on overflow water. *Journal of Physical Oceanography*, **49**, 1889–1904, doi: 10.1175/JPO-D-19-0053.1.

Spingys, C. P., A. C. N. Garabato, S. Legg, K. L. Polzin, E. P. Abrahamsen, C. E. Buckingham, A. Forryan, and E. E. Frajka-Williams, 2021: Mixing and transformation in a deep western boundary current: A case study. *Journal of Physical Oceanography*, **51**, 1205–1222, doi: 10.1175/JPO-D-20-0132.1.

Srinivasan, K., J. C. McWilliams, M. J. Molemaker, and R. Barkan, 2019: Submesoscale vortical wakes in the lee of topography. *Journal of Physical Oceanography*, **49**, 1949–1971, doi: 10.1175/JPO-D-18-0042.1.

Strong-Wright, J., S. Chen, N. C. Constantinou, S. Silvestri, G. L. Wagner, and J. R. Taylor, 2023: Oceanbiome.jl: A flexible environment for modelling the coupled interactions between ocean biogeochemistry and physics. *Journal of Open Source Software*, **8**, 5669, doi: 10.21105/joss.05669.

Talley, L., 2013: Closure of the global overturning circulation through the indian, pacific, and southern oceans: Schematics and transports. *Oceanography*, **26**, 80–97, doi: 10.5670/oceanog.2013.07.

Taylor, J. R., and R. Ferrari, 2009: On the equilibration of a symmetrically unstable front via a secondary shear instability. *Journal of Fluid Mechanics*, **622**, 103–113, doi: 10.1017/S0022112008005272.

Taylor, J. R., and R. Ferrari, 2010: Buoyancy and wind-driven convection at mixed layer density fronts. *Journal of Physical Oceanography*, **40**, 1222–1242, doi: 10.1175/2010JPO4365.1.

Taylor, J. R., and A. F. Thompson, 2023: Submesoscale dynamics in the upper ocean. *Annual Review of Fluid Mechanics*, **55**, 103–127, doi: 10.1146/annurev-fluid-031422-095147.

Thomas, L., S. Kelly, T. Klenz, W. Young, L. Rainville, H. Simmons, V. Hormann, and I. Stokes, 2024: Why near-inertial waves are less affected by vorticity in the northeast pacific than in the north atlantic. *Oceanography*, doi: 10.5670/oceanog.2024.301.

Thomas, L. N., J. R. Taylor, E. A. D'Asaro, C. M. Lee, J. M. Klymak, and A. Shcherbina, 2016: Symmetric instability, inertial oscillations, and turbulence at the gulf stream front. *Journal of Physical Oceanography*, **46**, 197–217, doi: 10.1175/JPO-D-15-0008.1.

Thomas, L. N., J. R. Taylor, R. Ferrari, and T. M. Joyce, 2013: Symmetric instability in the gulf stream. *Deep Sea Research Part II: Topical Studies in Oceanography*, **91**, 96–110, doi: 10.1016/j.dsr2.2013.02.025.

Thorpe, A. J., and R. Rotuno, 1989: Nonlinear aspects of symmetric instability. *J. Atmos. Sci.*, **46**, 1285–1299, doi: 10.1175/1520-0469(1989)046⟨1285:NAOSI⟩2.0.CO;2.

Thorpe, S., and M. White, 1988: A deep intermediate nepheloid layer. *Deep Sea Research Part A. Oceanographic Research Papers*, **35 (9)**, 1665–1671, doi: https://doi.org/10.1016/0198-0149(88)90109-4.

Thorpe, S. A., 1977: Turbulence and mixing in a scottish loch. *Philosophical Transactions of the Royal Society of London*, **286**, 125–181.

Toggweiler, J. R., K. Dixon, and K. Bryan, 1989: Simulations of radiocarbon in a coarse-resolution world ocean model: 1. steady state prebomb distributions. *Journal of Geophysical Research: Oceans*, **94**, 8217–8242, doi: 10.1029/JC094iC06p08217.

Uchida, T., and Coauthors, 2022: Cloud-based framework for inter-comparing submesoscale-permitting realistic ocean models. *Geoscientific Model Development*, **15**, 5829–5856, doi: 10.5194/gmd-15-5829-2022.

Uchoa, I., J. Wenegrat, and L. Renault, 2025: Sink of eddy energy by submesoscale sea surface temperature variability in a coupled regional model. *Journal of Physical Oceanography*, **55**, 993–1007, doi: 10.1175/JPO-D-24-0040.1.

Umlauf, L., and H. Burchard, 2011: Diapycnal transport and mixing efficiency in stratified boundary layers near sloping topography. *Journal of Physical Oceanography*, **41**, doi: 10.1175/2010JPO4438.1.

Umlauf, L., W. D. Smyth, and J. N. Moum, 2015: Energetics of bottom ekman layers during buoyancy arrest. *Journal of Physical Oceanography*, **45**, 3099–3117, doi: 10.1175/JPO-D-15-0041.1.

van Haren, H., 2006: Nonlinear motions at the internal tide source. *Geophysical Research Letters*, **33**, 2006GL025 851, doi: 10.1029/2006GL025851.

van Haren, H., 2023: Kmt, detailing layered mixing governed by internal wave breaking. *Environmental Fluid Mechanics*, **23**, 603–620, doi: 10.1007/s10652-023-09921-5.

van Haren, H., A. Cimatoribus, and L. Gostiaux, 2015: Where large deep-ocean waves break. *Geophysical Research Letters*, **42**, 2351–2357, doi: 10.1002/2015GL063329.

van Haren, H., and L. Gostiaux, 2012a: Detailed internal wave mixing above a deep-ocean slope. *Journal of Marine Research*, **70**, 173–197.

van Haren, H., and L. Gostiaux, 2012b: Energy release through internal wave breaking. *Oceanography*, **25**, 124–131, doi: 10.5670/oceanog.2012.47.

Voet, G., and Coauthors, 2024: Near-inertial energy variability in a strong mesoscale eddy field in the iceland basin. *Oceanography*, doi: 10.5670/oceanog.2024.302.

von Appen, W.-J., R. S. Pickart, K. H. Brink, and T. W. Haine, 2014: Water column structure and statistics of denmark strait overflow water cyclones. *Deep Sea Research Part I: Oceanographic Research Papers*, **84**, 110–126, doi: 10.1016/j.dsr.2013.10.007.

Wagner, G. L., and Coauthors, 2025a: High-level, high-resolution ocean modeling at all scales with oceananigans. *arXiv preprint*, doi: 10.48550/arXiv.2502.14148.

Wagner, G. L., and Coauthors, 2025b: Oceananigans v0.100.7. https://github.com/CliMA/Oceananigans.jl.

Walin, G., 1982: On the relation between sea-surface heat flow and thermal circulation in the ocean. *Tellus A: Dynamic Meteorology and Oceanography*, **34**, 187, doi: 10.3402/tellusa.v34i2.10801.

Waterhouse, A. F., and Coauthors, 2014: Global patterns of diapycnal mixing from measurements of the turbulent dissipation rate. *Journal of Physical Oceanography*, **44**, 1854–1872, doi: 10.1175/JPO-D-13-0104.1.

Wenegrat, J. O., J. Callies, and L. N. Thomas, 2018: Submesoscale baroclinic instability in the bottom boundary layer. *Journal of Physical Oceanography*, **48**, 2571–2592, doi: 10.1175/JPO-D-17-0264.1.

Wenegrat, J. O., and L. N. Thomas, 2020: Centrifugal and symmetric instability during ekman adjustment of the bottom boundary layer. *Journal of Physical Oceanography*, **50**, 1793–1812, doi: 10.1175/JPO-D-20-0027.1.

Whalen, C. B., C. de Lavergne, A. C. N. Garabato, J. M. Klymak, J. A. MacKinnon, and K. L. Sheen, 2020: Internal wave-driven mixing: governing processes and consequences for climate. *Nature Reviews Earth and Environment*, **1**, 606–621, doi: 10.1038/s43017-020-0097-z.

Whitehead, J. A., M. E. Stern, G. R. Flierl, and B. A. Klinger, 1990: Experimental observations of baroclinic eddies on a sloping bottom. *Journal of Geophysical Research: Oceans*, **95**, 9585–9610, doi: 10.1029/JC095iC06p09585.

Whitley, V., and J. Wenegrat, 2025: Breaking internal waves on sloping topography: Connecting parcel displacements to overturn size, interior-boundary exchanges, and mixing. *Journal of Physical Oceanography*, **55**, 645–661, doi: 10.1175/JPO-D-24-0052.1.

Whitt, D. B., and L. N. Thomas, 2013: Near-inertial waves in strongly baroclinic currents. *Journal of Physical Oceanography*, **43**, 706–725, doi: 10.1175/JPO-D-12-0132.1.

Wienkers, A. F., L. N. Thomas, and J. R. Taylor, 2021: The influence of front strength on the development and equilibration of symmetric instability. part 2. nonlinear evolution. *Journal of Fluid Mechanics*, **926**, doi: 10.1017/jfm.2021.684.

Winters, K. B., 2015: Tidally driven mixing and dissipation in the stratified boundary layer above steep submarine topography. *Geophysical Research Letters*, **42**, 7123–7130, doi: 10.1002/2015GL064676.

Winters, K. B., and L. Armi, 2013: The response of a continuously stratified fluid to an oscillating flow past an obstacle. *Journal of Fluid Mechanics*, **727**, 83–118, doi: 10.1017/jfm.2013.247.

Winters, K. B., P. N. Lombard, J. J. Riley, and E. A. D'Asaro, 1995: Available potential energy and mixing in density-stratified fluids. *Journal of Fluid Mechanics*, **289**, doi: 10.1017/S002211209500125X.

Wunsch, C., and R. Ferrari, 2004: Vertical mixing, energy, and the general circulation of the oceans. *Annual Review of Fluid Mechanics*, **36**, 281–314, doi: 10.1146/annurev.fluid.36.050802.122121.

Wynne-Cattanach, B. L., and Coauthors, 2024: Observations of diapycnal upwelling within a sloping submarine canyon. *Nature*, **630**, 884–890, doi: 10.1038/s41586-024-07411-2.

Yankovsky, E., and S. Legg, 2019: Symmetric and baroclinic instability in dense shelf overflows. *Journal of Physical Oceanography*, **49**, 39–61, doi: 10.1175/JPO-D-18-0072.1.

Yankovsky, E., S. Legg, and R. Hallberg, 2021: Parameterization of submesoscale symmetric instability in dense flows along topography. *Journal of Advances in Modeling Earth Systems*, **13**, doi: 10.1029/2020MS002264.

Ye, T., R. Mittal, H. S. Udaykumar, and W. Shyy, 1999: An accurate cartesian grid method for viscous incompressible flows with complex immersed boundaries. *Journal of Computational Physics*, **156**, 209–240, doi: 10.1006/jcph.1999.6356.

Young, W. R., and M. B. Jelloul, 1997: Propagation of near-inertial oscillations through a geostrophic flow. *Journul of Marine Research*, **55**, 735–766.

Zheng, Z., J. O. Wenegrat, B. Fox-Kemper, and G. J. Brett, 2025: Wind-catalyzed energy exchanges between fronts and boundary layer turbulence. *Journal of Physical Oceanography*, **55**, 1591–1606, doi: 10.1175/JPO-D-24-0243.1.

Zhou, H., W. Dewar, W. Yang, H. Liu, X. Chen, R. Li, C. Liu, and G. Gopalakrishnan, 2022: Observations and modeling of symmetric instability in the ocean interior in the northwestern equatorial pacific. *Communications Earth & Environment*, **3**, 28, doi: 10.1038/s43247-022-00362-4.

Zilberman, N. V., M. Scanderbeg, K. Balem, T. Schmitt, P. Weatherall, V. Thierry, E. V. Wijk, and D. Sandwell, 2025: Deep argo improves the accuracy and resolution of ocean bathymetry. *Earth and Space Science*, **12**, doi: 10.1029/2025EA004304.

Zängl, G., L. Gantner, G. Hartjenstein, and H. Noppel, 2004: Numerical errors above steep topography: A model intercomparison. *Meteorologische Zeitschrift*, **13**, 69–76, doi: 10.1127/0941-2948/2004/0013-0069.

Óscar Álvarez, A. Izquierdo, C. J. González, M. Bruno, and R. Mañanes, 2019: Some considerations about non-hydrostatic vs. hydrostatic simulation of short-period internal waves. a case study: The strait of gibraltar. *Continental Shelf Research*, **181**, 174–186, doi: 10.1016/j.csr.2019.05.016.